UC Irvine
UC Irvine Electronic Theses and Dissertations

Title

Silver Aluminum Solid-State and Eutectic Bonding Processes and Study of Intermetallic Properties and Corrosion for Advanced Electronics and Photonics

Permalink

https://escholarship.org/uc/item/1d23m0d4

Author

Fu, Shao-Wei

Publication Date

2018

Peer reviewed|Thesis/dissertation

eScholarship.org Powered by the California Digital Library
University of California

UNIVERSITY OF CALIFORNIA,
IRVINE

Silver Aluminum Solid-State and Eutectic Bonding Processes and Study of Intermetallic Properties and Corrosion for Advanced Electronics and Photonics

DISSERTATION

submitted in partial satisfaction of the requirements
for the degree of

DOCTOR OF PHILOSOPHY

in Engineering

by

Shao-Wei Fu

Dissertation Committee:
Professor Chin C. Lee, Chair
Associate Professor Daniel R. Mumm
Professor Frank G. Shi

2018

© 2018 Shao-Wei Fu

DEDICATION

To

my dear family and friends

Without their moral support, unconditional love, and encouragement,
this dissertation would have never been possible.

TABLE OF CONTENTS

		Page
LIST OF FIGURES		vi
LIST OF TABLES		xi
ACKNOWLEDGEMENT		xiv
CURRICULUM VITAE		xv
ABSTRACT OF THE DISSERTATION		xvii
CHAPTER 1	Introduction	1
1.1	Electronic Packaging	1
1.2	High Temperature Power Devices and Electronics	2
1.3	Electric Interconnections (Wire Bonding)	4
1.4	Die-Attachments	7
1.5	Metalized substrates (DBC, DBA)	9
1.6	Objectives and Outline of this Dissertation	11
1.7	References	16
CHAPTER 2	Experimental Setup and Techniques	22
2.1	Material Synthesis and Processing	22
	2.1.1 Vacuum Ingot Casting	22
	2.1.2 Electron Beam Evaporation	23
	2.1.3 Electroplating	26
2.2	Vacuum Furnace and Bonding Setup	26
2.3	Material Characterization Techniques	30
	2.3.1 X-Ray Diffraction (XRD)	30
	2.3.2 Scanning Electron Microscope (SEM)/Energy Dispersive X-ray Spectroscopy (EDX)	32
	2.3.3 Focus Ion Beam (FIB)	35

2.3.4 Transmission Electron Microscopy (TEM) 37
2.4 References.. 38
CHAPTER 3 A study on intermetallic compound formation in Ag-Al system and evaluation of its mechanical properties by micro-indentation.. 39
3.1 Introduction.. 39
3.2 Experimental Design and Procedures 41
3.3 Experimental Results and Discussion 43
3.3.1 Phase Evaluation in Ag-Al Alloys..................................... 44
3.3.2 Intermetallic Compound Formation at Ag-Al Joint Interface.. 50
3.3.3 Micro-indentation Analysis of Ag_3Al and Ag_2Al 52
3.4 Summary 56
3.5 References 57
CHAPTER 4 A corrosion study of Ag-Al intermetallic compounds in chlorine -containing epoxy molding compounds....................................... 63
4.1 Introduction.. 63
4.2 Experimental Design and Procedure 65
4.3 Experimental Results and Discussion 67
4.3.1 Corrosion Experiment of Ag-Al joints under HAST........... 67
4.3.2 Corrosion Experiment of Ag_3Al and Ag_2Al under HAST 69
4.3.3 Proposed Corrosion Model of Ag-Al IMC under HAST 80
4.4 Summary 83
4.5 References 84
CHAPTER 5 Direct silver to aluminum solid-state bonding processes........... 89
5.1 Introduction.. 89
5.2 Experimental Design and Procedure 92

5.3 Experimental Results and Discussion 94
5.3.1 Ag-Al Solid-State Bonding Process 94
5.3.2 Shear Test Results of Ag-Al Solid-State Bonding 98
5.3.3 TEM analysis on Ag-Al Solid-State Bonding 104
5.4 Summary 106
5.5 References 107
CHAPTER 6 Direct bonding silver to aluminum using eutectic reaction in air 113
6.1 Introduction 113
6.2 Experimental Design and Procedure 116
6.3 Experimental Results and Discussion 117
6.3.1 Ag-Al Eutectic Bonding Process and Comparison with Ag-Al Solid-State Bonding 117
6.3.2 Shear test results of Ag-Al eutectic bonding process 122
6.4 Summary 127
6.5 References 128
CHAPTER 7 New solid-state die-attach method using silver foil bonded on aluminum substrate by eutectic reaction 132
7.1 Introduction 132
7.2 Experimental Design and Procedure 135
7.3 Experimental Results and Discussion 138
7.3.1 Ag Foil Bonding Technique to Produce Si/Ag/Al joints 138
7.3.2 Shear Test Results of the Si/Ag/Al joints 145
7.4 Summary 154
7.5 References 155
CHAPTER 8 Summary 160

LIST OF FIGURES

Page

Figure. 1.1 Schematic layout of a simplified package 4

Figure. 2.1 The hydrogen-oxygen torch operation system and vacuum sealing procedures 23

Figure. 2.2 Angstrom Engineering EvoVac Glovebox Evaporator 25

Figure. 2.3 Schematic of the vacuum furnace showing key components: (a) quartz cylinder, (b) upper stainless plate, (c) base plate, (d) graphite platform, (e) heating wire, (f) feedthroughs, (g) platform thermocouple, and (h) sample thermocouple....... 27

Figure. 2.4 Photo of the graphite heating platform 28

Figure. 2.5 Essential hardware components of Rigaku SmartLab X-ray Diffractometer.. 32

Figure. 2.6 The interaction volume and the signals produced by the interaction between the electron beam and specimen............. 34

Figure. 2.7 Philips XL-30 FEG SEM 35

Figure. 2.8 SEM image of FIB deposited Pt strip layer (left). SEM image of TEM sample attaching TEM grid by using Omniprobe. (right) 36

Figure. 2.9 FEI/Philips CM-20 conventional TEM.. 38

Figure. 3.1 The casted ingot and disk samples after annealing at 200 °C for 750 hours. After annealing, the ingot samples were cut into disks (10 mm in diameter and 1 mm in thickness) and mechanically polished for further examination........................... 43

Figure. 3.2 Experimental and calculated Ag-Al phase diagrams from 10 to 50 at. % Al at 400 to 725 K. The solid lines and dashed lines represent experimental data and calculated data, respectively. Spots marked 1-11 reveal the equilibrium phases identified in Ag-Al alloy samples no. 1 to no. 11 with composition from 19 to 43 at. % Al, as shown in Table 3.1. The white spot indicates a phase from a single-phase sample. The black spot is a phase from a two-phase alloy.. 45

Figure. 3.3 Back-scattered SEM images showing microstructures of Ag-Al alloys. The single-phase intermetallics: (a) Ag-36 at. % Al and (b) Ag-22 at. % Al. The two-phase alloys: (c) Ag-19 at. % Al alloy, (d) Ag-27 at. % Al alloy, and (e) Ag-43 at. % Al alloy. (f) shows enlarged area of (e). Phases identified for each sample are indicated on the image and listed in Table 3.1......... 48

Figure. 3.4 XRD spectra of the representative Ag-Al alloys: (a) Ag-36 at. % Al, (b) Ag-22 at. % Al, (c) Ag-19 at. % Al alloy, (d) Ag-27 at. % Al alloy, and (e) Ag-43 at. % Al alloy 49

Figure. 3.5 The cross-sectional SEM image of Ag-Al joints after annealing at 200°C for 750 hours. Red dots marked 1-5 indicate the EDX analysis location on the interface region. The resulting phase compositions are listed in the table below...................................... 52

Figure. 3.6 Indentation deformation and cracks morphology in (a) bulk μ-Ag_3Al under loading of 300 gf and (b) 500 gf, and (c) bulk δ-Ag_2Al under loading of 500 gf and (d) 1000 gf. In sample (d), region A, B and C show the presence of slip bands around the indent.. 54

Figure. 4.1 Chemical structure of 3-chloro-1-propanol..................................... 66

Figure. 4.2 Cross-sectional images of the Ag-Al joints molded in EMC: (a) optical microscopy image before HAST, (b) back-scattered electron image before HAST, (c) optical image after HAST, (d) back-scattered electron image after HAST 69

Figure. 4.3 EDX composition analysis results and the XRD spectrum of the Ag_3Al and Ag_2Al intermetallic alloys. 71

Figure. 4.4 The cross-sectional SEM back-scattered electron images of the Ag_3Al and Ag_2Al compounds molded in epoxy molding compounds after HAST for 25, 50, and 125 hours........................ 72

Figure. 4.5 The cross-sectional SEM back-scattered electron images of (a) Ag and (b) Al molded in epoxy molding compounds after HAST for 125 hours... 73

Figure. 4.6 (a) The SEM back-scattered electron images and EDX composition analysis of the corroded Ag_3Al compound after 50-hour HAST. (b) The SEM image of an enlarged corrosion region. Red dots marked by 1-12 indicate the EDX analysis locations. The resulting element compositions are listed in

the table. (c) The EDX energy spectra of representative analysis locations........ 75

Figure. 4.7 (a) The SEM back-scattered electron images and EDX composition analysis of the corroded Ag_2Al compound after 50-hours HAST. (b) The SEM image of an enlarged corrosion region. Red dots marked by 1-12 indicate the EDX analysis location. The resulting element compositions are listed in the table. (c) The EDX energy spectra of the representative composition analysis points 77

Figure. 4.8 SEM images and EDX elemental mappings of Ag, Al, O, and Cl elements on the corrosion region of Ag_2Al........ 78

Figure. 4.9 Corrosion layer thickness versus HAST time on bulk Ag_3Al and Ag_2Al disks molded in epoxy molding compound containing chlorine ions 79

Figure. 4.10 Schematic illustration of proposed corrosion model of the Ag-Al IMC in chlorine-containing EMC under HAST 81

Figure. 5.1 (a) Commercial surface pre-treatments and metallization processes on Al substrate in electronic packages. (b) Proposed Ag-Al solid-state bonding technique to direct bond Al foil on Al substrate as a bondable layer which is compatible with nano-silver paste and solders. In a more advanced level, device chips can be bonded to the Ag foil on Al substrates at 300 °C using solid-state bonding technique 91

Figure. 5.2 SEM back-scattered electron images of Ag-Al joints bonded at (a)400 °C, (b) 425 °C, and (c) 450 °C for 10 minutes. In the enlarged image of (c), the red dots marked by 1-5 indicate the EDX analysis locations and the resulting element compositions are listed in the Table 5.1 96

Figure. 5.3 Ag-Al binary phase diagram 97

Figure. 5.4 (a) The schematic diagram of the shear test specimen configurations: single-lap-joint and single-strap-joint (used in this study). (b) The shear strength of the Ag-Al joints bonded at 400 °C, 425 °C, and 450 °C, respectively........ 99

Figure. 5.5 SEM back-scattered images of the fracture surfaces on the Al side of the Ag-Al joints bonded at (a) 400 °C, (b) 425 °C, and (c) 450 °C. The XRD spectrum of the fracture surface on the Al side of Ag-Al joints bonded at 450 °C is presented in (d) 101

Figure. 5.6 SEM back-scattered images on the cross-sections of Ag-Al joint bonded at 450 °C after shear test (a) Al side and (b) Ag side. Enlarged images on Ag side are shown in (c) and (d) 103

Figure. 5.7 (a) The SEM cross section image shows the interface region of a Ag-Al joint bonded at 450 °C. (b) The TEM image of the rectangle box in (a), where aluminum oxide line is indicated by red arrows. The TEM specimen was prepared by in-situ dual focused ion beams (FIB) 105

Figure. 5.8 High resolution STEM images of (a) the Ag_2Al/Al interface region and (b) a Ag_2Al region containing a thin Al_2O_3 layer. The inserts display selected area diffraction patterns (SADP) of the encircled Ag_2Al zones characterized along $[11\bar{2}1]$ zone axis 106

Figure. 6.1 (a) Commercial surface pre-treatments and metallization processes on Al substrate in electronic packages. (b) Proposed Ag-Al direct bonding technique which is compatible with nano-silver paste and solders 115

Figure. 6.2 SEM back-scattered electron images of Ag-Al joints bonded at 450 °C for 10 minutes. In the enlarged image of (b) and (c), the red dots marked by 1 - 6 indicate the EDX analysis locations and the resulting element compositions are listed in the Table 6.1 118

Figure. 6.3 Ag-Al binary phase diagram 119

Figure. 6.4 SEM back-scattered electron images of Ag-Al joints bonded at 570 °C for 5 minutes. In the enlarged image of (b) and (c), the red dots marked by 1- 6 indicate the EDX analysis locations and the resulting element compositions are listed in the Table 6.2 121

Figure. 6.5 The schematic diagram of the single-strap-joint specimen configuration used in this study for the shear testing........ 122

Figure. 6.6 (a) SEM secondary electron image of the fracture surfaces on the Al side of the Ag-Al solid state bonding. SEM back-scattered images of the cross-sections of Ag-Al solid state bonding after shear test on the (b) Al side and (c) Ag side 124

Figure. 6.7 (a) High resolution STEM image of the $Ag_2Al/Al_2O3/Ag_2Al$ interface region. (b)The selected area diffraction pattern

(SADP) of the Ag_2Al along $[11\bar{2}1]$ zone axis 125

Figure. 6.8 (a) SEM secondary electron image of the fracture surfaces on the Al side of the Ag-Al eutectic bonding 126

Figure. 7.1 (a) Commercial surface activating and metallization processes on Al substrates and subsequent die-attach process such as silver sintering or soldering. (b) New Ag-Al eutectic and solid-state techniques to bond Al foil directly on Al substrate, onto which Si chip can be directly bonded using solid-state bonding 135

Figure. 7.2 Bonding structure design of the Ag foil bonding technique. (a) First bonding step: Ag-Al solid-state bonding or Ag-Al eutectic bonding to bond Ag foil directly to Al substrate. (b) Second bonding step: solid-state process to bond metalized Si chip to Ag-cladded Al substrate 137

Figure. 7.3 SEM back-scattered electron images of a Si/Ag/Al sample for which the first bonding step is Ag-Al solid-state process and the second step is solid-state bonding of Si chip. In the enlarged image (c), the red dots marked by 1 - 5 indicate EDX analysis locations with element compositions listed in Table 7.2 140

Figure. 7.4 Ag-Al binary phase diagram 141

Figure. 7.5 SEM back-scattered electron images of a Si/Ag/Al sample for which the first bonding step is Ag-Al eutectic process and the second step is solid-state bonding of Si chip. In the enlarged image, (b) and (c), the red dots marked by 1-6 indicate the EDX analysis locations with element compositions listed in Table 7.3 143

Figure. 7.6 (a) The schematic illustration of die shear test configuration. (b) Optical image of a sample fracturing at the Ag/Al interface. (c) Optical image of a sample fracturing within the Si chip 146

Figure. 7.7 Back-scattered SEM images of a fractured Si/Ag/Al sample for which the first bonding step is solid-state process: (a) the Al side, (b) the Ag side, (c) enlarged image of (b) 148

Figure. 7.8 (a) SEM secondary electron image of the fracture surface on the Al side of a Si/Ag/Al joint sample for which Ag-Al solid-state process was used for the first bonding step. (b) Enlarged SEM image of the fracture surface 150

Figure. 7.9 The SEM back-scattered electron images of the fractured Ag/Al interface of a Si/Ag/Al joint for which the first bonding step was conducted using Ag-Al eutectic reaction. (a) Al side and (b) Ag side 152

Figure. 7.10 (a) SEM secondary electron image of the fracture surface on the Al side of a Si/Ag/Al joint sample for which the first bonding step was conducted using Ag-Al eutectic reaction. (c) Enlarged SEM image showing the quasi-cleavage feature of the Ag_2Al compound and the ductile dimples on the Al solid solution 152

LIST OF TABLES

Page

Table 1.1 Temperature requirements for applications in harsh environments 3

Table 1.2 Summary of popular die-attach materials with melting and operating temperatures........ 8

Table 1.3 Thermal cycling test results of DBC substrate and DBA substrate 11

Table 3.1 Equilibrium phase and chemical compositions of Ag-Al alloys determined in this study........ 43

Table 3.2 Phase compositions, hardness (H), elastic modulus (E), and fracture toughness (Kc) of the μ-Ag3Al and δ-Ag2Al........ 55

Table 4.1 Compositions (at. %) of intermetallic compound layer in the Ag-Al joint molded in EMC before and after HAST........ 69

Table 5.1 EDX data on locations 1 - 5 near Ag-Al interface in Fig. 2 (c) 97

Table 5.2 The shear strength and the fracture surface composition of Ag-Al joints bonded at 400 °C, 425 °C, and 450 °C, respectively.. 102

Table 6.1 EDX data on locations 1- 6 near Ag-Al interface in Fig. 6.2........ 119

Table 6.2 EDX data on locations 1- 6 near Ag-Al interface in Fig. 6.4........ 121

Table 6.3 Shear strengths of Ag-Al joints using solid-state and eutectic bonding techniques........ 122

Table 7.1 Conditions of the first bonding step (Ag-Al solid-state and eutectic) and the second bonding step (solid-state) to produce the Si/Ag/Al structure........ 138

Table 7.2 EDX data on locations 1 - 5 near Ag/Al interface in Fig. 7.3........ 140

Table 7.3 EDX data on locations 1 - 6 near Ag/Al interface in Fig. 7.5........ 143

Table 7.4 Shear test results on breakage force, shear strength, and fracture interface of six Si/Ag/Al joint samples produced by Ag-Al solid-state bonding........ 147

Table 7.5 Shear test results on breakage force, shear strength, and fracture interface of six Si/Ag/Al joint samples produced by Ag-Al eutectic bonding 148

ACKNOWLEDGMENTS

I would like to express my deepest gratitude to my advisor, Professor Chin C. Lee, for his guidance, mentorship and support. His working style greatly influences how I conduct research. He teaches me to review the fundamental theories and pay attention to the details when conducting research. In addition, I would also like to thank him for his nominations for numerous fellowships and the financial support from him. Without his mental and financial support, it could never have been possible for me to complete my PhD. I would like to extend my gratefulness to my committee members: Professor Daniel R. Mumm, Professor James C. Earthman, Professor Frank G. Shi, and Professor Lizhi Sun, for their valuable suggestions on my research.

My appreciation also goes to my colleagues, Dr. Shou-Jen Hsu, Dr. Yuan-Yun Wu, Dr. Yi-Ling Chen, Dr. Yongjun Huo, Jiaqi Wu, Yipin Wu, Chun-An Yang and Roozbeh Sheikhi for contributing their expertise, discussions, and collaborations, and for creating a family-like working environment during my PhD. study. I also want to thank INRF staff, Jake, Mo and Richard, and IMRI staff, Dr. Jian-Guo Zheng and Dr. Qiyin Lin for their assistance on conducting experiments. I have to show my greatest gratitude to my friends at UCI, Evan Lin, Monica Hsu, Qam Chen, Ken Tang, Michael Lu, Ethan Lin, and Yangchun Lee, for the bonded friendship and kind support. I would like to extend my sincere gratitude to my family and my better half Y-Ying for their unconditional love and support. Their encouragement is the strongest driving force for overcoming difficulties. This dissertation could have never been completed without their love and support.

CURRICULUM VITAE

Shao-Wei Fu

2012	Bachelor of Science Department of Materials Science and Engineering National Tsing-Hua University, Hsinchu, Taiwan
2012-2014	Research Assistant National Synchrotron Radiation Research Center, Hsinchu, Taiwan
2014-2018	Graduate Student Researcher Materials & Manufacturing Technology Department of Electrical Engineering and Computer Science University of California at Irvine, Irvine, CA, USA
2016	Master of Science in Engineering, Concentration in Materials and Manufacturing Technology, The Henry Samueli School of Engineering, University of California, Irvine, CA, USA
2016-2018	Teaching Assistant Department of Electrical Engineering and Computer Science University of California at Irvine, Irvine, CA, US
2018	Doctor of Philosophy in Engineering Concentration in Materials and Manufacturing Technology, The Henry Samueli School of Engineering, University of California at Irvine, Irvine, CA, US

FIELD OF STUDY

Materials and Manufacturing Technology

PUBLICATIONS

▪ Journal Articles

1. Y. Huo, **S. Fu**, Y. Chen and C.C. Lee, "A reaction study of sulfur vapor with silver and silver–indium solid solution as a tarnishing test method," Journal of Materials Science: Materials in Electronics, vol. 27, no. 10, pp. 10382-10392, 2016.

2. **S. Fu** and C.C. Lee, "A corrosion study of Ag–Al intermetallic compounds in chlorine-containing epoxy molding compounds," Journal of Materials Science: Materials in Electronics, vol. 28, no. 20, pp. 15739-15747, 2017.

3. **S. Fu** and C.C. Lee, " A study on intermetallic compound formation in Ag-Al system and evaluation of its mechanical properties by micro-indentation," Journal of Materials Science: Materials in Electronics, vol. 29, no. 5, pp. 3985-3991, 2018.

4. **S. Fu** and C.C. Lee, " Direct silver to aluminum solid-state bonding processes" Materials Science and Engineering: A, vol. 722, pp. 160-166, 2018.

5. **S. Fu** and C.C. Lee, " New solid-state die-attach method using silver foil bonded on aluminum substrate by eutectic reaction, ", submitted.

▪ Published Conference Proceedings and Conference Presentations

1. **S. Fu** and C.C. Lee, "Solid-State Reactions of Silver and Aluminum Associated with Silver Wire Bonds," in Electronic Components and Technology Conference (ECTC), 2016 IEEE 66th, pp. 648-653, 2016.

2. **S. Fu** and C.C. Lee, " Direct bonding silver to aluminum using eutectic reaction in air," in Electronic Components and Technology Conference (ECTC), 2018 IEEE 68th, published in 2018.

ABSTRACT OF THE DISSERTATION

Silver to Aluminum Direct Bonding Process using Solid-State and Eutectic Reaction with Intermetallic Study for High-Temperature Electronics

By

Shao-Wei Fu

Doctor of Philosophy in Engineering

University of California, Irvine, 2018

Professor Chin C. Lee, Chair

A major challenge in today's high-temperature power electronics is the lack of reliable packaging materials with good performance. Silver (Ag) has the advantages of high electric and thermal conductivity, high melting point, and excellent mechanical properties, making it a promising material for wire bonding and die-attachment in microelectronic and power electronic packages. On the other hand, aluminum (Al) is often used as a conductive metal layer in semiconductor devices, such as chip metallizations and thick film substrates. This research aims to evaluate the material properties of the Ag-Al intermetallic compounds, and develop new Ag-Al bonding processes for high-temperature applications.

First, Ag-Al alloys and Ag-Al joints are produced to study the intermetallic phases in Ag-Al alloys and at Ag/Al interface. The deformation and fracture behaviors of Ag_2Al and Ag_3Al are evaluated using micro-indentation technique. The results show that Ag_3Al exhibits high hardness and low fracture toughness with brittle fracture mode, while Ag_2Al shows ductile deformation with no crack formation. Moreover, a corrosion experiment is designed to

measure the corrosion rates of Ag, Al, and Ag_3Al and Ag_2Al compounds in epoxy molding compounds under humidity test. The results show that the corrosion rate of Ag_3Al is twice of that of Ag_2Al, and no corrosion occurs on Ag or Al. The results above clearly suggest that Ag_3Al is likely the weak link and should be avoided. Finally, this research further develops a novel Ag foil bonding technique to bond Ag foils directly to Al substrates. Two Ag-Al bonding processes are developed: solid-state and eutectic reaction. Using the Ag foil as a bonding medium, Si chips are bonded to the Ag-cladded Al substrates using solid-state process at 300 °C. In Ag-Al soli-state bondings, Ag and Al atoms inter-diffused through the thin Al_2O_3 to form Ag_2Al and Ag_3Al compounds. In Ag-Al eutectic bondings, Ag_2Al+(Al) eutectic structure forms at bonding interface without Ag_3Al compound formation. The native Al_2O_3 layer, a potential fracture path, is broken into pieces during eutectic reaction and possibly dispersed into the eutectic structure. Shear test results of Si/Ag/Al joints far exceed the military criterion. The fracture mechanisms are studied in detail.

Chapter One

Introduction

1.1 Electronic Packaging

The requirements for today's IC commercial products are smaller, faster, more powerful and reliable. Electronic package technique is one of the critical concerns to make these functionalities. The major functions are: (1) to provide a path for electrical current, (2) to distribute the on/off signals of chip, (3) to dissipate the heat generation by the electrical circuit and (4) to support and protect the chip [1]. The overall performance of a single chip package, a multichip module, and an entire electronic system is not only determined by the electrical components and the circuit layouts, but also strongly depends on the packaging technology. Hierarchically, electronic packaging begins from the interface of a semiconductor chip, which is considered as the first-level or chip-level packaging, to higher level packaging such as board-level and syste package leads, and the encapsulation [2]. m-level packaging. Chip-level packaging consists of the attachment of chips to substrates, the interconnection of chips to package leads, and the encapsulation [2].

In recent years, high-temperature electronic packaging has been rapidly developed due to increasing demand of power electronics applications, particularly for the automotive, aerospace, and energy production industries [3]. Silicon carbide (SiC) and gallium nitride (GaN), both wide bandgap semiconductors, have emerged as promising alternatives to replace silicon (Si) in the high-power and high-temperature segments [4]. Compared to silicon devices, wide bandgap semiconductor devices exhibit lower switching losses, higher breakdown voltages, and higher operating temperatures (above 350 °C) [5]. For continuous operations under such high temperatures, novel interconnection materials and packaging structures are required for power electronics systems.

1.2 High Temperature Power Devices and Electronics

Numerous electronic applications (automotive, aircrafts, space exploration, and oil and gas industry for well logging) require operation at high temperatures that differ greatly form common standard operating temperature [6]. The temperature and operating life requirement for those applications is summarized in Table 1.1. The oil and gas industry is the oldest and currently still the largest application of high-temperature electronics. The electronic systems for the oil and natural gas well-logging, particularly around drilling heads,

must operate at temperatures ranging from 150 °C to 300 °C [7]. The temperature requirement is varied according to the depth of the well. The enhanced geothermal well-logging systems require downhole gauges tolerating up to 600 °C [7]. In order to assure the device performance and reliability under such high temperature operation, corresponding packaging materials and techniques must be compatible with more severe thermal and electrical constraints.

Table 1.1. Temperature requirements for applications in harsh environments [7, 8].

Industry	Operating temperature requirements	
Automotive	Engine control electronic	150 °C
	Electric suspension and brake	300 °C
Aircraft	Engine control electronic	300 °C
	Combustion sensing	500 °C
Spacecraft	Power management	200 °C
	Planet exploration	400 °C
Well-logging	Oil and gas	300 °C
	Geothermal	600 °C

Figure 1.1 shows the schematic layout of a simplified packaging structure in a power electronics module. The die-attachment (Pb solder, Pb-free solder, and sintered silver paste, etc.) provides mechanical support, thermal dissipation, and electrical conduction between the semiconductor chip and the substrate. The wire bond (usually Al and Au wires)

electrically connects the chip and the external leads of the electronic device. The substrate (direct bond copper, direct bond aluminum) includes an insulating ceramic layer between two metalized conductors. The molding compound covers and encapsulates the chip and other packaging components.

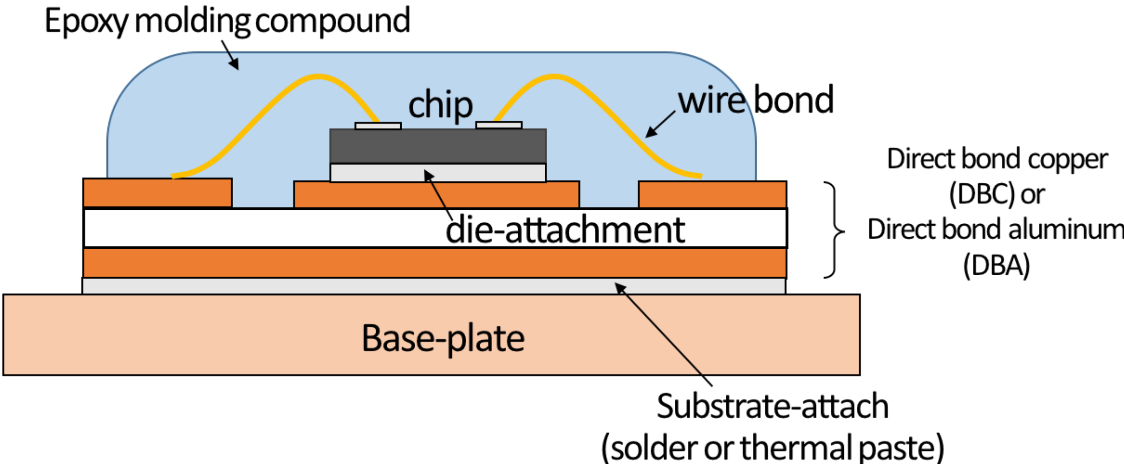

Fig. 1.1 Schematic layout of a simplified package.

In the following sections, the important packaging components and interconnection technologies are reviewed. The working mechanisms and high temperature considerations for the wire bonding, die-attachment, and metalized substrates are discussed. The research motivation and dissertation outline are given at last.

1.3 Electrical Interconnections (Wire Bonding)

Wire bonding is the technique of making electrical connection between chips and external leads of the semiconductor device [9]. Aluminum (Al), gold (Au), and more recently copper (Cu) wires are commonly used for wire bonding on the Al pad [10]. For decades, thermosonic ball bonding with Au wires has been the dominant wire bonding technique, providing excellent workability and stable chemical properties. However, the rising gold price has motivated the packaging industry to look for alternative wire materials such as Cu and Ag. With the new interest in Cu wire bonding over the past several years, there has been extensive evaluation of Cu wires on Al bond-pads in industry [11-12]. The reaction on Cu/Al interface and Cu wire-bond reliability have been studied. Since Cu wires get oxidized easily and are harder than Au and Ag alloy wires, the process window of Cu wire bonding is narrower. Special bonding equipment are usually needed. Reliability issues such as Al pad splashing and Si chip cratering in Cu wire-bonds are reported [12-14].

In power electronic packages, ultrasonic wedge bonding with large Al wire is the most commonly used bonding technique because of the large wire diameter and the low cost of Al [13]. However, Al wire-bonds are susceptible to heel crack, where failure arises from the overworked bond heel during the ultrasonic bonding process [15]. Additional fatigue failures are caused by the large difference of thermal expansion coefficients (CTE) between the Al wires (24 ppm/ °C) and Si chips (2.7 ppm/ °C) [16]. Recently, Cu wire bonding are

rapidly developed for power electronics. Cu has the advantages of high yield strength and more compatible CTE (18 ppm/ °C) than Al. On the other hand, the work hardening and the oxidation issue are the drawbacks of Cu wire bonding during thermal cycles [17]. In high temperature storage test at 200 °C, Kirkendall voids and cracks are observed in the Cu-Al intermetallic compounds (IMC), and the bonding strength of Cu wire-bonds remarkably decrease [18]. Although other possible alternatives, such as large Au and platinum (Pt) wires, have shown good reliability in storage test above 200 ° C, the use of large Au and Pt wires for power electronics remains limited due to the high materials cost [17].

Most recently, Ag alloy wires have been introduced as a new bonding wire alternative. Compared to Cu wires, Ag alloy wires have the advantages of higher oxidation resistance and higher ductility. Thus, Ag alloy wire bonding exhibits a wider process window and can reduce Al pad splash and silicon damage [19]. In high temperature storage test (HTS), Ag alloy wire-bonds pass industrial reliability standard. Microstructures of Ag alloy wire-bonds exhibit homogenous IMC growth without cracks or Kirkendall void formation, and no electrical degradation is detected [20]. In industrial production, Ag alloy wire bonding possess similar bonding parameters to Au wire bonding. Regular wire bonders can be used without equipment replacement [10]. Recently, some LED manufacturers started to deploy Ag alloy wire bonding in LED semiconductor packaging. Ag alloy wires will be one of the

promising wire options for microelectronic and power electronic packaging. Further Ag-Al IMC studies and reliability assessments of Ag alloy wire-bonds are required.

1.4 Die-attachments

The die-attach layer provides mechanical fixture, thermal dissipation path and possibly electrical connection between the chips the substrates [1, 2]. For power electronics, the selection of proper die-attach materials is important to provide sufficient mechanical reliability and overall packaging thermal management, especially under high temperature operation. Table 1.2 lists the melting temperatures and normal operating temperatures of commercial die-attachment materials. The commonly used conductive adhesives and Pb-free (Sn-Ag-Cu) solders are not suitable for power electronics due to their low melting temperatures (below 220 °C) [21]. Pb-rich solders (Pb-5Sn, Pb-10Sn), with melting point around 300 °C, was widely used in power electronic packaging because of their desirable properties such as good wettability and high ductility [22]. In year 2006, with the recognition of the negative effect of Pb on human health, regulations such as Restriction of Hazardous Substances (RoHS) have prohibited the usage of Pb in electronic devices. High temperature Pb-free solder alloys (Au-Sn, Bi-Ag, and Zn-Al) retain problems in the soldering process,

including poor processability, massive intermetallic compound, and high material cost [23]. Moreover, these solder alloys still cannot meet the operating capabilities of SiC-based power devices (operating temperature above 350°C). Recently, sintered nano-silver paste has been introduced as a novel die-attach method for power devices [24]. Ag has the highest electrical and thermal conductivity among all metals. By reducing the Ag particles size to the nanometer scale, Ag sintering can proceed at a lower temperature and pressure due to the sufficient driving forces provided by the surface energy of Ag nano-particles. Some reliability issues, such as oxidation and high temperature mechanical degradation, associated with the porous silver joint structure due to organic degassing still need to be addressed in the future work.

Table 1.2 Summary of popular die-attach materials with melting and operating temperatures.

Die-attachment Materials (wt. %)	Melting Temperature (°C)	Normal Operating Temperature (°C)
Silver filled epoxy	100	75
$Sn_{63}Pb_{37}$	183	92
Sn-Ag-Cu	217	119
$Pb_{95}Sn_5$	300	185
$Au_{80}Sn_{20}$	280	170
Zn-Al	382	229
Au-Ge	356	230
Au-Si	363	236
Sintered nano-silver paste	961	715

1.5 Metallized Substrates (DBC, DBA)

The substrate in electronic packages provides critical functions including circuit support and protection, heat dissipation, and signal and power distribution [1, 2]. For power electronics, the substrate reliability becomes a serious concern when operating at high temperatures [25]. Conventional organic board based substrates are not suitable for power devices due to their low glass transition temperature. Ceramic based metalized substrates have been developed for high temperature power electronics. Direct bond copper (DBC) substrates is the most commonly used electronic circuit board for power semiconductor modules. DBC substrates have advantages of high current carrying capacity, relatively high thermal conductivity, and controlled coefficient of thermal expansion (CTE) [26]. Recently, reliability issues of DBC substrates in thermal cycling tests have been reported [27, 28]. With large temperature excursion higher than 250 °C, severe thermomechanical stresses induce cracks at the copper/ceramic interface, leading to eventual delamination of the DBC structure [28].

As a possible alternative, direct bond aluminum (DBA) substrates have been developed. DBA substrates outperform DBC substrates in thermal cycling tests [28]. The reason is the lower yield stress and plastic strain rate of aluminum as opposed to copper, which result in

lower thermomechanical stress at the aluminum/ceramic interface and less strain hardening during thermal cycling. No crack or delamination was observed in DBA substrates after 1500 thermal cycles from -55 °C to 250 °C [28, 29]. Although DBA exhibits superior thermomechanical performance than DBC, a main challenge of using DBA or other Al metalized substrates in electronic packaging is its poor bondability. The native aluminum oxide layer prevents aluminum from electroless or electrolytic plating of metallization layer, which is an essential step to make Al substrates bondable to die-attach materials such as solders and nano-silver paste. Thus, a zincating process is required to prepare DBA substrates for further metallization processing. During the zincating process, the aluminum oxide is dissolved in the zincating solution, and a layer of zinc is deposited to protect the surface, providing a basis for subsequent metallization [30]. The zincating process exhibits a narrow process window due to its high reaction sensitivity to Al surface conditions. The zincating and following metallization processes on Al surface largely increase the processing cost and add more reliability issues of DBA substrates [31]. In this dissertation, the surface pretreatment process and die-attach method on Al metalized substrates is further reviewed and discussed in Chapter 5 and 6. Direct solid-state and eutectic bonding processes of Ag to Al are developed, and a new solid-state die-attach method using silver foil bonded on aluminum substrate is proposed.

Table 1.3 Thermal cycling test results of DBC substrate and DBA substrate

	DBC - aluminum nitride	DBA - aluminum nitride
Thermal cycling range: -40 °C to 125 °C	Delamination after 600 cycles	No crack observed after 3000 cycles
Thermal cycling range: - 40 °C to 250 °C	Delamination after 30 cycles	No crack observed after 700 cycles

1.5 Objectives and Outline of this Dissertation

A major challenge in today's high-temperature electronic packaging is the lack of reliable packaging materials with good performance, especially for the chip-level packaging (electrical interconnections, die-attachments, and substrates). The overall reliability and performance of the power electronic devices is highly dependent on the electrical, thermal, and mechanical characteristics of these packaging materials.

As mentioned in pervious section, for electrical interconnections, Ag alloy wire bonding is considered as a promising alternative to replace Au, Cu, or Al wire bonding for microelectronic and power electronic packaging. Compared to Cu wires, Ag alloy wires have lower oxidation rate and higher ductility [19]. It had been reported that Ag alloy wire bonding exhibits wider process window and causes less Al pad splash and silicon damage. A

concern is intermetallic compound (IMC) formation at the bonding interface [20]. The IMC layer has often been found to be the weak region due to its brittle nature, leading to a high failure rate of the bonding joints. For Au and Cu wire bonding, cracks and voids incur at the Au/Al and Cu/Al bonding interfaces under humidity storage test conditions, causing wire-bond failure [32-34]. Moisture-induced corrosion at the IMC region and bonding interface seems to be the root cause of this failure. For Ag alloy wire bonding, although many studies have reported the reliability test results of the Ag-Al wire-bonds, studies on the Ag-Al IMC are rather limited. The mechanical properties and corrosion resistances of the Ag-Al IMC are still unclear.

For packaging substrates, the classically used direct-bonded copper (DBC) substrates fails after 30 cycles with large temperature excursion higher than 250 °C [35]. With the thermomechanical reliability of DBC as a major concern, direct bond aluminum (DBA) substrates have been developed. DBA exhibits superior thermomechanical performance than DBC [28]. No crack or delamination was observed in DBA substrates after 1500 thermal cycles from -55 °C to 250 °C. However, since Al is not compatible with most die-attach materials, zincating and metallization processes are required to provide bondable surface for die-attachment process. To prevent the reliability issues caused by the zincating and metallization processes, novel surface pretreatment process and die-attach method on Al are

needed for DBA substrates.

In this dissertation, Chapter 1 provides an overview of current technologies of high temperature electronics packaging, including electrical interconnections, die-attachments, and metallized substrates. The research methodologies used in this dissertation, including materials fabrication, bonding furnace setup and process flow, and material characterization techniques are described in Chapter 2.

In Chapter 3, experiments were designed to investigate the Ag-Al IMC formation in the Ag-Al system and evaluate the IMC mechanical properties. Ag-Al ingot alloys and Ag-Al joints were produced to study the intermetallic phase formation in the Ag-Al alloy and at the Ag/Al interface. Ag_2Al and Ag_3Al compound ingots were grown by in-house casting method. The deformation and fracture behaviors of Ag_2Al and Ag_3Al were evaluated using micro-indentation technique. The results show that Ag_3Al exhibits high hardness and low fracture toughness with brittle fracture mode, while Ag_2Al shows ductile deformation with no crack formation. Correlations between the mechanical properties of the Ag-Al IMC and the Ag-Al joint reliability are discussed.

In Chapter 4, the corrosion mechanism of the Ag-Al joint in chlorine-containing molding compounds under high temperature/high humidity test (HAST) was studied. A corrosion experiment according to industry condition was established to measure the

corrosion rates of Ag, Al, and Ag_3Al and Ag_2Al compounds in epoxy molding compounds under HAST. The results show no corrosion on Ag and Al. The corrosion rates of Ag_3Al and Ag_2Al is linear verses time, indicating a reaction-controlled corrosion mechanism. A corrosion model was proposed to establish the chemical reactions of Ag_3Al and Ag_2Al with moisture and chlorine ions in molding compounds.

After studying the Ag-Al solid-state reaction and the Ag-Al IMC properties associated with the Ag-Al wire-bond reliability, we move to develop novel Ag-Al bonding techniques to directly bond Ag to Al substrates. In Chapter 5, a new Ag-Al solid-state bonding process was proposed. This bonding was deemed not possible in the past because of the native oxide on the Al substrate. Our experimental results, however, show that this bonding is achievable so far as the Ag and Al atoms on the interface can interdiffuse through the thin Al_2O_3 layer and form Ag_3Al and Ag_2Al IMC. No surface treatment was applied on Al substrates to remove the native Al_2O_3 layer before the bonding. The shear strength of Ag-Al joints passes the military standard by a large margin. SEM and TEM with electron diffraction technique was utilized to study the nanostructure of the bonding interface. The Ag-Al bonding mechanisms and fracture behaviors were investigated and discussed.

In Chapter 6, to further improve the Ag-Al bonding reliability and propose bonding process in air atmosphere, a new bonding technique has been developed to directly bond Ag

to Al substrates using eutectic reaction in air. During the bonding process, Ag_2Al+(Al) eutectic structure formed at the Ag/Al interface with no Ag_3Al IMC formation. The native Al_2O_3 layer on Al substrates, as a potential fracture path, was broken during the eutectic reaction and possibly dispersed into the eutectic structure. The resulting Ag-Al joints exhibits an excellent shear strength of 40 MPa and a ductile fracture mode.

In Chapter 7, a two-step bonding process has been developed to bond Si chips to Al substrates using Ag foils. The first bonding step bonds Ag foils directly to Al substrates without using any flux. The second bonding step attaches Si chips to the Ag-cladded Al substrates using solid-state process at 300 °C without any additional die-attach material. Two Ag-Al direct bonding techniques, solid-state and eutectic reaction, were demonstrated in the first bonding step. Shear test results of the resulting Si/Ag/Al joints far exceed the military criterion. The interface microstructures and fracture mechanisms of the Si/Ag/Al joints bonded with solid-state and eutectic reaction were studied and discussed.

This research provides a novel solid-state die-attach method on Al substrates by using the Ag foil bonding technique. No surface treatment, such as zincating and metallization, was required on Al substrates before the bonding process. With the advantages of high thermal conductivity, high reliability, lightweight, and process simplicity, the Ag-cladded Al structures should be highly valuable for applications in electronic and photonic packages,

such as aircraft and aerospace vehicles. Finally, the important conclusions in this dissertation and future research perspectives is presented in Chapter 8. The author hope that the content of this dissertation can be meaningful and contributing some insights to the research and development of high temperature power electronics and packaging technology.

1.7 References

1. R. R. Tummala, ed., Fundamentals of Microsystems Packaging, New York: McGraw- Hill, pp.21, 2001.
2. International Technology Roadmap for Semiconductors, 2005 Ed, Assembly and Packaging, 2005.
3. H. S. Chin, K. Y. Cheong, and A. B. Ismail, "A review on die attach materials for SiC-based high-temperature power devices, " Metallurgical and Materials Transactions B, vol. 41, No.4, pp.824-832, 2010.
4. C. Buttay, D. Planson, B. Allard, D. Bergogne, P. Bevilacqua, C. Joubert, M. Lazar, C. Martin, H. Morel, D. Tournier, C. Raynaud, "State of the art of high temperature power electronics", Materials Science and Engineering B, vol. 176. No. 4, pp. 283-288, 2011.
5. G. Pensl and W. J. Choyke, "Electrical and optical characterization of SiC", Physica B:

Condensed Matter, vol. 185, No. 1, pp. 264-283, 1993.

6. P. Hagler, P. Henson and R. W. Johnson, "Packaging technology for electronic applications in harsh high-temperature environments," IEEE Trans. Ind. Electron., vol. 58, no. 7, pp. 2673-2682, 2011.
7. H. Chin, K. Cheong, and A. Ismail, "A review on die attach materials for SiC-based high-temperature power devices, " Metallurgical Mater. Trans. B, vol. 41, pp. 824–832, 2010.
8. R.W. Johnson, "A review of high temperature electronics packaging, " Proceedings of the 1989 High Temperature Electronics Conference, Albuquerque, NM, June 5-7, 1989.
9. C. Harper, Electronic packaging and interconnection handbook, McGraw-Hill, Inc., 2004.
10. C.L. Gan and U. Hashim, "Evolutions of bonding wires used in semiconductor electronics: Perspective over 25 years," J. Mater. Sci: Mater. Electron., vol. 26, no. 7, pp. 4412-4424, 2015.
11. Z. Zhong, "Overview of wire bonding using copper wire or insulated wire," Microelectronics Reliability, vol. 51, no. 1, pp. 4-12, 2011.
12. B.K. Appelt, A. Tseng, C. Chen and Y. Lai, "Fine pitch copper wire bonding in high volume production," Microelectronics Reliability, vol. 51, no. 1, pp. 13-20, 2011.
13. G.G. Harman, Wire bonding in microelectronics, McGraw-Hill, 2010.
14. C. Breach, "What is the future of bonding wire? will copper entirely replace gold?" Gold

Bulletin, vol. 43, no. 3, pp. 150-168, 2010.

15. S. Ramminger, N. Seliger, and G. Wachutka. "Reliability model for Al wire bonds subjected to heel crack failures." Microelectronics Reliability, vol. 40, no. 8-10, pp. 1521-1525. 2000.
16. A. Morozumi, K. Yamada, T. Miyasaka, S. Sumi, and Y. Seki. "Reliability of power cycling for IGBT power semiconductor modules." IEEE Trans. Ind. Appl., vol. 39, no. 3, pp. 665-671. 2003.
17. R. Khazaka, L. Mendizabal, D. Henry, and R. Hanna. "Survey of high-temperature reliability of power electronics packaging components." IEEE Transactions on power Electronics, vol. 30, no. 5, pp. 2456-2464, 2015.
18. R. Schueller, “Copper wire bond failure mechanisms,” DfR Solutions, Minneapolis, MN, USA, 2012.
19. J. Tsai, A. Lan, D. Jiang, L. W. Wu, J. Huang and J. Hong, "Ag alloy wire characteristic and benefits," in Electronic Components and Technology Conference (ECTC), 2014 IEEE 64th, pp. 1533-1538, 2014.
20. L. J. Kai, L. Y. Hung, L. W. Wu, M. Y. Chiang, D. S. Jiang, C. Huang and Y. P. Wang, "Silver alloy wire bonding," in Electronic Components and Technology Conference (ECTC), 2012 IEEE 62nd, pp. 1163-1168, 2012.
21. K. N. Tu, Solder Joint Technology, New York, Springer, 2007.

22. Y. Yamada, Y. Takaku, Y. Yagi, K. Ishida et al., "Reliability of wire-bonding and solder joint for high temperature operation of power semiconductor device", Microelectronics Reliability, vol. 47, no. 12, pp. 2147-2151, Dec. 2007.

23. K. Suganuma, S.J. Kim, K.S. Kim, "High-temperature lead-free solders: Properties and possibilities", The Journal of The Minerals Metals and Materials Society, vol. 61, no. 1, pp. 64-71, Jan. 2009

24. J.G. Bai, J.N. Calata, G.Q. Lu, "Processing and characterization of nanosilver pastes for die-attaching SiC devices", IEEE Transactions on Electronics Packaging Manufacturing, vol. 30, no. 4, pp. 241-245, Oct. 2007.

25. Y. Yoshino, H. Ohtsu and T. Shibata, "Thermally induced failure of Copper Bonded alumina substrates for electronic packaging," J Am Ceram Soc, vol. 75, no. 12, pp. 3353-3357, 1992.

26. G. Dong, X. Chen, X. Zhang, K. D. Ngo and G. Lu "Thermal fatigue behaviour of Al2O3-DBC substrates under high temperature cyclic loading," Soldering & Surface Mount Technology, vol. 22, no. 2, pp. 43-48, 2010.

27. S. T. Chua, K. S. Siow, "Microstructural studies and bonding strength of pressureless sintered nano-silver joints on silver direct bond copper (DBC) and copper substrates aged at 300°C", Journal of Alloys and Compounds, vol. 687, pp. 486-498, 2016.

28. S. Kraft, A. Schletz and M. Maerz, "Reliability of silver sintering on DBC and DBA

substrates for power electronic applications," in Integrated Power Electronics Systems (CIPS), 2012 7th International Conference on, pp. 1-6, 2012.

29. T. G. Lei, J. N. Calata, K. D. Ngo and G. Lu, "Effects of large-temperature cycling range on direct bond aluminum substrate," IEEE Transactions on Device and Materials Reliability, vol. 9, no. 4, pp. 563-568, 2009.

30. S. Lee, J. Lee and Y. Kim, "Nucleation and growth of zinc particles on an aluminum substrate in a zincate process," J Electron Mater, vol. 36, no. 11, pp. 1442-1447, 2007.

31. M. M. Arshad, I. Ahmad, A. Jalar, G. Omar and U. Hashim, "The effects of multiple zincation process on aluminum bond pad surface for electroless nickel immersion gold deposition," Journal of electronic packaging, vol. 128, no. 3, pp. 246-250, 2006.

32. H. Kim, J. Y. Lee, K. Paik, K. Koh, J. Won, S. Choe, J. Lee, J. Moon and Y. Park, "Effects of Cu/Al intermetallic compound (IMC) on copper wire and aluminum pad bondability," IEEE Transactions on Components and Packaging Technologies, vol. 26, no. 2, pp. 367-374, 2003.

33. M. Lue, C. Huang, S. Huang and K. Hsieh, "Bromine-and chlorine-induced degradation of gold-aluminum bonds," J Electron Mater, vol. 33, no. 10, pp. 1111-1117, 2004.

34. C. L. Gan, C. Francis, B. L. Chan and U. Hashim, "Extended reliability of gold and copper ball bonds in microelectronic packaging," Gold Bulletin, vol. 46, no. 2, pp. 103-115, 2013.

35. D. C. Katsis and Y. Zheng, "Development of an extreme temperature range silicon carbide power module for aerospace applications," in Power Electronics Specialists Conference, PESC 2008. IEEE, pp. 290-294, 2008.

Chapter Two

Experiment Setup and Techniques

2.1 Materials Synthesis and Processing

2.1.1 Vacuum Ingot Casting

In this dissertation, ingot casting method has been used to synthesize bulk Ag-Al alloys. The vacuum environment is necessary for the casting production of bulk metallic material for avoiding oxidation and reducing voids and defects created by trapped air bubbles. The hydrogen-oxygen torch operation system was employed to seal the raw materials in quartz tubes with controlled vacuum. Quartz tube was selected as the capsule for the vacuum casting method due to its high melting temperature (1700 ºC) and good chemical stability. The high purity raw materials shots of desired compositional ratios were firstly loaded into the quartz tube with one end closed. Next, the quartz tube filled with raw materials was pumped down to a vacuum level of 50 milli-torr by a mechanical pump. During torch operation, the O_2 to H_2 ratio was controlled as 1:4 to obtain a stable reducing flame, and the pressures of regulator gauges for hydrogen and oxygen are fixed at 10 psi and 2.5 psi, respectively. As the open end of the quartz tube was melted and sealed by torch flaming, a

vacuum capsule containing designed raw materials can be produced. The capsule was then brought to and kept at 1000 °C for 1 hours to completely melt the raw materials, and followed by 48-hour annealing at 50 °C above the liquidus temperature to ensure homogenization of the ingot alloy.

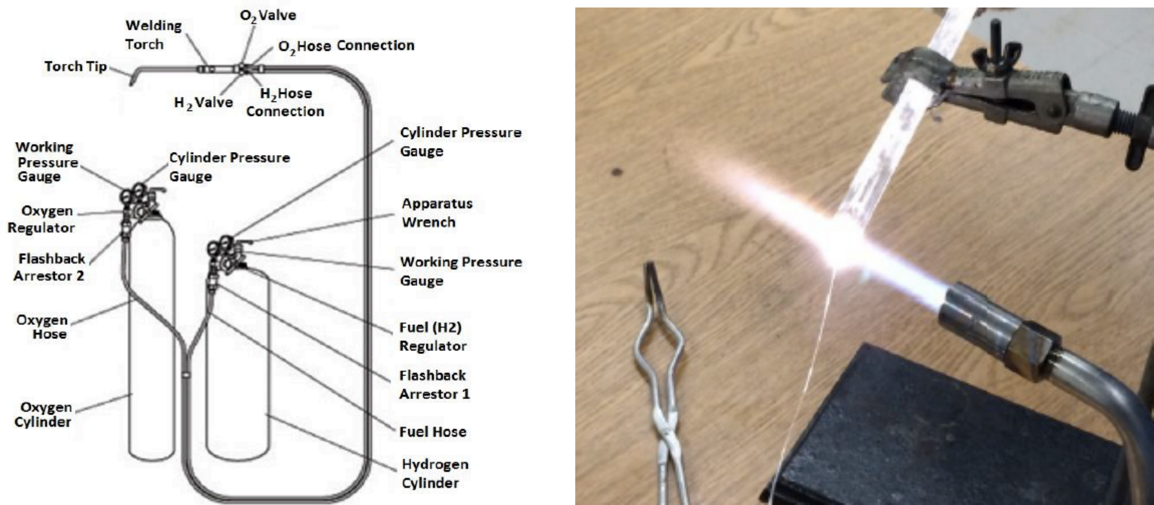

Fig. 2.1 The hydrogen-oxygen torch operation system and vacuum sealing procedures

2.1.2 Electron Beam Evaporation

Electron beam (e-beam) evaporation is a form of physical vapor deposition (PVD). PVD processes are commonly used for the deposition of metallic films, because they can be performed at lower process risk and cheaper in regards to materials cost that Chemical Vapor Deposition (CVD). In e-beam evaporation, a target anode is bombarded with an

electron beam given off by a charged tungsten filament under high vacuum. The electron beam causes atoms from the target to transform into the gaseous phase. The gas molecules are able to evaporate freely and then condense on all surfaces inside the chamber. The entire process takes place inside of a vacuum chamber and multi-layer coatings can be deposited in one duty cycle.

The vacuum deposition provides clean, uniform, and well thickness controlled metal layers. In one high vacuum cycle, usually 2×10^{-6} to 3×10^{-6} torrs, up to three or four metal layers can be deposited. These metal layers are efficiently prevented from oxidations. However, during deposition, the substrates undergo high temperature, which may incur unwanted interdiffusion and reaction between deposited metal layers and also cause breakage when bonding CTE mismatch materials. In addition, it is difficult to produce metal layers thicker than 10μm using vacuum deposition method, and to build and maintain a vacuum system is costly. In our experiment, e-beam deposition is used to produce thin metal films, serving as adhesion layers and capping layers.

In this dissertation, Angstrom Engineering EvoVac Glovebox Evaporator in Irvine Material Research Institute (IMRI) was used for the thin film sample preparation of this dissertation, as shown in Fig. 2.9. The evaporation chamber can be pumped down to 2×10^{-8} torr with mechanical-cryogenic two stages pumping system within 1 hour. After turning-on

the E-beam source, the sample stage can be protected by E-beam stutter and sample stage stutter during the pre-soaking of target materials. A featured function of this instrument is glancing angle deposition (GLAD) technique, which enable the sample stage rotate at designed speed both in-plane and out-plane to fabricate thin film sample with smooth, high coverage, or even nano-structures. During the E-beam evaporation process, the deposition rate was monitored by quartz crystal microbalance (QCM), and was precisely controlled by an automatic negative feedback system, using proportional–integral–derivative (PID) controller.

Fig. 2.2 Angstrom Engineering EvoVac Glovebox Evaporator.

2.1.2 Electroplating

Electroplating is a process of depositing a metal layers on a conductive substrate immersed in an electrolytic bath composed of a solution of the salt of the metal to be plated. The deposition is driven by external DC current. The anode is made of the metal to be plated, and the cathode connects to the substrate. Take silver (Ag) electroplating as an example. At the anode, Ag atoms are dissolved by $Ag \rightarrow Ag^{+} + e^{-}$, and the reduction reaction at the cathode is $Ag^{+} + e^{-} \rightarrow Ag$. The Ag ions, thus, are plated onto the substrate surface. Compared to vacuum deposition, electroplating is less expensive and easily to fabricate thick layers. It can be implemented at relative low temperature, from room temperature to 80°C.

2.2 Vacuum Furnace and Bonding Setup

In this research, all of bonding process is done in a vacuum furnace built in house as depicted in Fig. 2.3 [1]. The vacuum furnace consists of a quartz cylinder, two stainless steel plates, a heating platform, and a ceramic post. The quartz cylinder, having the inner diameter of 130 mm and height of 200 mm, is sandwiched between two steel plates to construct a vacuum chamber. The interference between the cylinder and the steel plate is sealed by an O-ring. It is easy to observe the sample during the reflow process because to the transparency

of quartz. The temperature is monitored by two type-K thermocouples (Chromel+ Alumel-) at two locations, the top surface of sample and the sidewall of platform. Inside the vacuum furnace, a graphite platform is supported by a ceramic poster standing at the center of the base stainless steel plate.

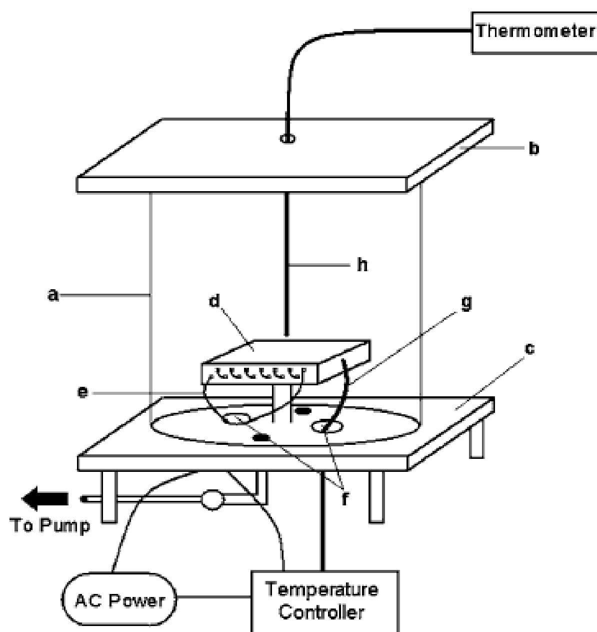

Fig. 2.3 Schematic of the vacuum furnace showing key components: (a) quartz cylinder, (b) upper stainless plate, (c) base plate, (d) graphite platform, (e) heating wire, (f) electrical feedthroughs, (g) platform thermocouple, and (h) sample thermocouple

The graphite platform, having the size of 75×75×10 mm^3, is drilled with many holes to allow the heating wire (Nickel-Chromium alloy) going through the body of the block. The wire is electrically insulated from the graphite using ceramic tubes as shown in Fig. 2.4.

Graphite was chosen as the material of the platform because it has been experimentally proven that it absorbs 97% of radiation and is a nearly perfect emitter of radiation [2]. Therefore, the platform will absorb a maximum amount of heat given off by the wires. It is also easy to machine and can withstand very high temperature.

Fig. 2.4 Photo of the graphite heating platform

To achieve thermal isolation of the platform from the upper and base plates, a ceramic poster having relatively low thermal conductivity is utilized to support the platform. Once the chamber is pumped down, heat transfers to the upper and base plates from the platform through radiation mechanism only. Because the plates are constructed of stainless steel, being able to reflect and scatter radiation, the plates will not absorb much heat radiation and can keep cooled to low temperature with natural convection by ambient air. It is designed so

that the platform is well thermally isolated from the chamber enclosure that includes the cylinder wall and two steel plates. This is a unique feature of the furnace design. It allows for the platform to be heated to high temperatures while the temperature of the rest of the chamber remains relatively low, which is very important in the safety issue and the ability to seal the chamber in vacuum using O-rings. The upper plate is mounted with an ultra-Torr connector to take the small K-type thermocouple probe for measuring the sample temperature. The base plate contains four ports with National Pipe Thread (NPT). Two of these are occupied by feedthroughs. One feedthrough is for a pair of copper wires to pass into the chamber to connect to the two ends of the heating wire. The other is for thermocouple wires. The third port is used for the vacuum gauge, and the fourth port is for connecting to a mechanical pump. In this design, the chamber is allowed to pump down to 50 millitorrs and the maximum temperature of platform reaches up to 450 °C.

To conduct the bonding process in the vacuum chamber, the samples are mounted in a graphite fixture and applied with a static pressure to ensure intimate contact. The assembly is then placed on the graphite platform. Once the vacuum furnace is pumped down and kept at 50 to 100 millitorrs to suppress oxidation during bonding, the temperature controller is turned on to heat up the platform. The bonding process is carried out at wide ranges of temperature and dwell time for different bonding systems. After reaching the peak

temperature, the heater is turned off and the assembly is allowed to cool down naturally to room temperature in a vacuum environment. Comparing to bonding in air, the amount of oxygen available to oxidize the molten solder is reduced by a factor of 15,200 in 50 millitorrs of vacuum.

2.3 Characterization Techniques

2.3.1 X-Ray Diffraction (XRD)

X-ray diffraction is used to identify the crystalline phases present in materials and to measure the structural properties, such as average grain size, crystallinity, lattice parameter, strain, and crystal defect, of multilayer films. X-ray diffraction peaks are produced by constructive interference of a monochromatic beam of x-rays scattered at specific angles from each lattice plane in a sample. An X-ray, generated by a cathode ray tube, is filtered to produce monochromatic radiation. These X-rays are then collimated to concentrate and direct the ray towards to the sample. In principle, X-ray diffraction is fairly easy to understand by Bragg's Law: the constructive interference happens when the interaction of incident rays and lattice plan satisfy Bragg's equation

$$n\lambda = 2dhklsin\theta$$

where λ is the wavelength of electromagnetic radiation, d is the lattice spacing in the crystalline sample, and θ is the diffraction angle. The peak intensities are determined by the atomic arrangement within the lattice planes. These diffracted X-rays are then detected, processed and counted. Therefore, the X-ray diffraction pattern is the fingerprint of periodic atomic arrangements of a sample. By scanning the sample through a range of 2θ angles, all possible diffraction directions of the lattice can be attained. In this study, it was applied to different materials and their results are presented as a plot of diffraction intensity corresponding to diffraction angles.

In this research, Rigaku SmartLab X-ray diffractometer in Irvine Material Research Institute is used for X-ray diffraction characterization. As shown in Fig. 2.12, SmartLab X-ray diffractometer consists of a number of essential parts: (1) The collimated Cu Kα line excitation X-ray source, (2) A set of incident-beam optics and receiving-beam optics, (3) The X-Ray detector: count the number of X-rays scattered by the sample, (4) The goniometer and sample stage: the platform that holds and moves sample, optics, detector, and x-ray tube. In general, two different hardware settings, namely, Bragg–Brentano (BB) and Parallel Beam (PB), can be used in SmartLab diffractometer. Bragg–Brentano optics setting is used for bulk polycrystalline or power materials characterization, whereas Parallel Beam optics setting is usually applied to thin film materials characterization.

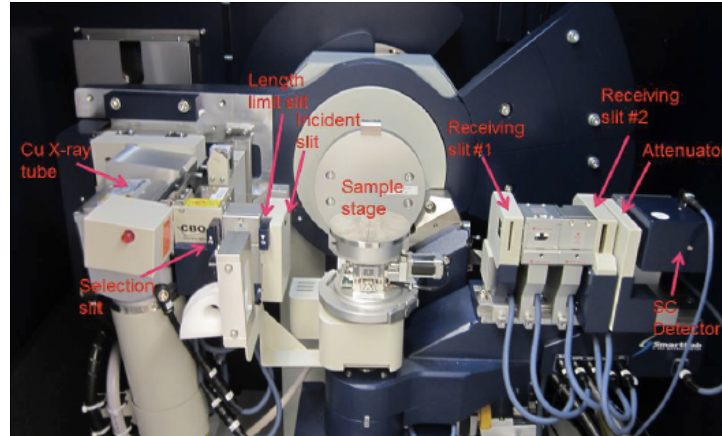

Fig. 2.5 Essential hardware components of Rigaku SmartLab X-ray diffractometer.

2.3.2 Scanning Electron Microscope/Energy Dispersive X-ray Spectroscopy (SEM/EDX)

SEM is an electron microscope that uses focused beam of high energy electrons to image specimens. The high energy electrons interact with the atoms that make up the sample generating a variety of signals from the surface of the specimens. These signals, which includes secondary electrons (SE), back-scattered electrons (BSE), diffracted backscattered electrons (EBSD), characteristic X-rays, visible light (cathodoluminescence), specimen current, and transmitted electrons, reveal the specimens' surface topographies, chemical compositions, orientations, and crystalline structures. Fig. 2.6 displays the interaction volume and the signals produced by the interaction between electron beam and specimens [3]. The SE detector installed in the SEM captures the SE imaging high-resolution

morphologies and topographies for the specimens' surfaces. Due to the very narrow electron beam, SEM micrographs have a large depth of field, yielding a three-dimensional surface image of a specimen. BSE detectors may also be used in a SEM to illustrate contrasts in the composition of multiphase specimens. For instance, a stronger BSE intensity is detected if a larger number of backscattered electrons reaching to a BSE detector. Larger atoms, with a greater Z-number, have a higher probability of producing elastic collisions due to their larger cross-sectional area. Thus, elements with a greater atomic number (Z) show brighter images than smaller atomic number in BSE images. X-ray is also produced during the interaction of an electron beam with a specimen. The energy-dispersive detector is used to separate the characteristic x-rays of different elements into an energy spectrum. In addition, EDX software system is used to analyze the energy spectrum for determining the specific elements in the specimen. Energy dispersive X-ray spectroscopy can be used to find the chemical composition of materials in small area ($\sim 10^{-6}$ mm^2), and can create element composition mappings over this area. The spot size, defined as the diameter of the electron beam, depends on the density and atomic number of the interested elements and accelerating voltage.

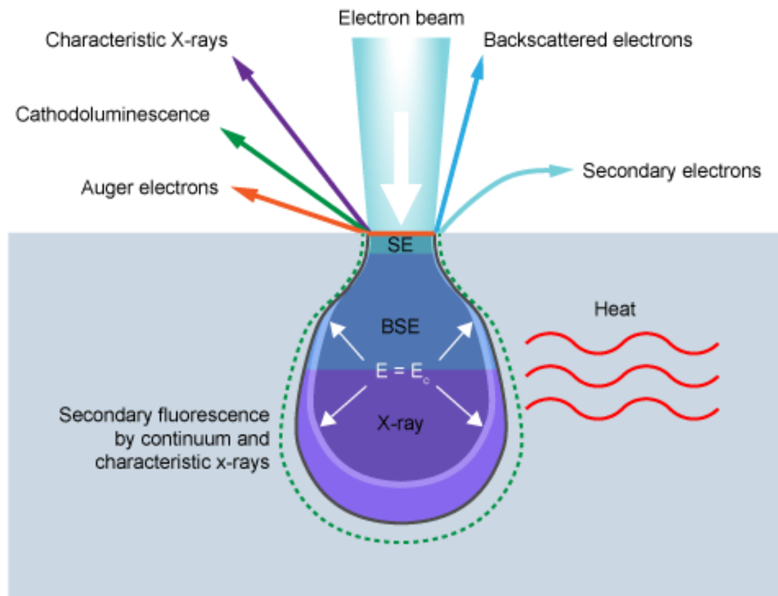

Fig. 2.6 The interaction volume and the signals produced by the interaction between the electron beam and specimen [3].

In this research, the Philips XL-30 FEG SEM was used for most of SEM imaging in the content of this dissertation. XL-30 is a thermionic field emission SEM which is fully automatic gun configuration controlled by advanced computer technology. The magnification is up to 800,000X with 2 nm resolution. It is easy to use for examining and survey the morphology of the nano structures. This XL30 also equipped with EDX detector to provide the composition information.

Fig. 2.7 Philips XL-30 FEG SEM

2.3.3 Focused Ion Beam (FIB)

A focused ion beam (FIB) instrument is almost identical to a SEM, but uses a beam of ions rather than electrons. The focused ion beam can directly modify or "mill" the specimen surface by the sputtering process. The ion milling can be controlled with nanometer precision. By controlling the energy and intensity of the ion beam, it is possible to perform precise nano-machining to remove unwanted material and produce a clean surface.

In this dissertation, FIB is very useful for making a clean cross-sectional sample surface, thereby avoiding the “smear” effects usually induced by mechanical polishing. FEI Quanta 3D FEG Dual Beam SEM/FIB Instrument was used for most of FIB imaging and operation in this research. Gallium ion (Ga+) sources are used to generate the ion beams. The gallium primary

ion beam hits the sample surface and sputters a small amount of material, which leaves the surface as either secondary ions or neutral atoms. The primary beam also produces secondary electrons. As the primary beam raster-scanning on the sample surface, the signal from the sputtered ions or secondary electrons is collected to form images. During SEM/FIB operation, a Gas Injection Source (GIS) probe can be inserted into the chamber, and FIB-assisted chemical vapor deposition (CVD) can be applied to deposit Pt onto the sample surface. The FEI Quanta 3D has also equipped with Omniprobe, which can be used to pick the chopped-off sample in the chamber. By using the FIB deposition, FIB cutting, and Omniprobe, a sample preparation method for transmission electron microscopy (TEM) analysis has been developed.

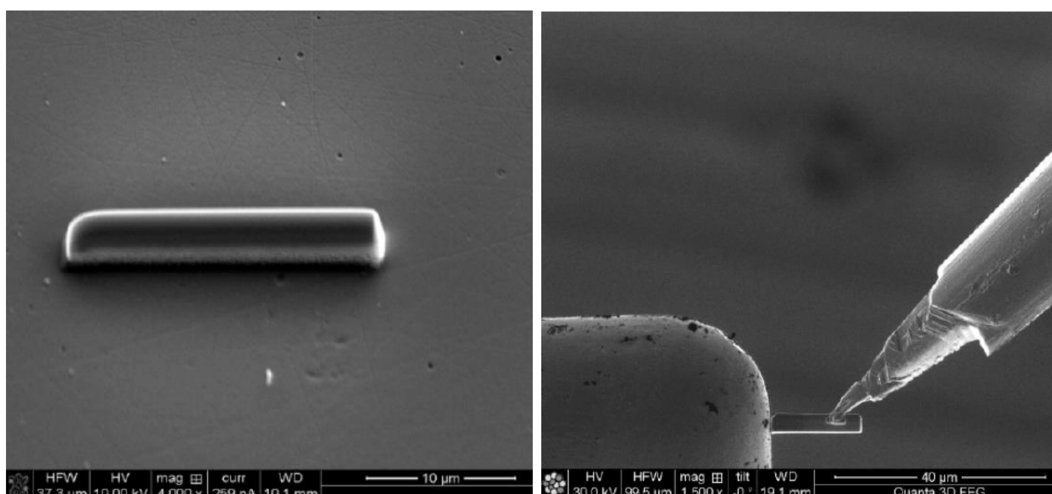

Fig. 2.8 SEM image of FIB deposited Pt strip layer (left). SEM image of TEM sample attaching TEM grid by using Omniprobe. (right).

2.3.4 Transmission Electron Microscopy (TEM)

Transmission electron microscopy is a microscopy technique in which a beam of electrons is transmitted through a material sample to form an image. The TEM sample is most often an ultrathin section less than 100 nm thick or a suspension on a grid. An image is formed from the interaction of the electrons with the sample as the beam is transmitted and/or diffracted through the material sample. Compared with SEM, TEM offers a much better spatial resolution, up to single atom (Å) and can give much more material structural and crystallographic information than SEM. Therefore, TEM is extremely useful for material and solid-state physics scientific study. Nowadays, TEM related techniques are relative mature and have various modes for different applications, such as bright field (BF), dark field (DF), selected area diffraction (SAD), convergent-beam electron diffraction (CBED), electron energy-loss spectrometry (EELS), high-resolution TEM (HRTEM), high-angle annular dark-field (HAADF) imaging, and more. More details on the topics of TEM physics and principles can be found in the reference textbook [6]. In this research, FEI/Philips CM-20 conventional TEM, as shown in Fig. 2.25, was used in the content of this dissertation. Philips CM 20 TEM with EDX system has accelerating voltage 200 kV that can obtain the image resolution down to 0.27 nm with maximum magnification 750,000X. This CM20 TEM is equipped with an

energy dispersive spectrometer (EDS) that can perform element analysis.

Fig. 2.9 FEI/Philips CM-20 conventional TEM.

2.4 References

1. Chin C. Lee, Dave T. Wang, and Won S. Choi, "Design and construction of a compact vacuum furnace for scientific research," Review of Scientific Instruments, American Institute of Physics, 77, 125104, pp.125104.1-125104.5, Dec. 2006
2. http://www.egglescliffe.org.uk/physics/astronomy/blackbody/bbody.html
3. http://www.ammrf.org.au/myscope/sem/background/concepts/interactions.php

Chapter Three

A study on intermetallic compound formation in Ag-Al system and evaluation of its mechanical properties by micro-indentation

3.1 Introduction

Wire bonding technology has been widely used to interconnect chips and substrates of microelectronic packages [1-3]. In the 1980s, both aluminum (Al) and gold (Au) wires were adopted in wire bonding. With increasing demand for high complexity and high reliability packaging, thermosonic ball bonding with Au wires became the dominant wire bonding technique. As the pitch of wire bonds continued to decrease, Al wires were abandoned because of their rapid oxide growth during spark ball formation. However, large diameter Al wires are still used on high power devices with the wedge bonding method [4]. Au wire diameter has continued to decrease to 15 μm due to rising gold prices and shrinking pad size [5,6]. On the other hand, the rising gold price has motivated the packaging industry to look for alternative wire materials such as silver (Ag) and copper (Cu) [7-11]. Recently, several packaging companies have bonded Cu wires on Al bond-pads in production. The Cu/Al interface reaction and Cu wire bond reliability have been reported [7,8]. Since Cu wires get

oxidized easily and exhibit higher hardness as compared to Au and Ag alloy wires, Cu wires possess a narrower process window for wire bonding. The high hardness of Cu could cause Al pads splashing, and the higher bonding force for Cu wire bonding could induce Si chip cratering [9]. In addition, Cu-Al wire bonds exhibit low corrosion resistance to halogen elements under high humidity. Halogen content, such as chlorine, in molding compound should be controlled to prevent the corrosion at the Cu/Al interface [11].

Recently, Ag alloy wires have been introduced as a new bonding wire alternative [10,12]. Compared to Cu wires, Ag alloy wires have the advantages of higher oxidation resistance and higher ductility. Thus, Ag alloy wire bonding exhibits a wider process window and can reduce Al pad splash and silicon damage [13]. A concern is intermetallic compound (IMC) formation at the bonding interface. The IMC layer has often been found to be the weak region due to its brittle nature, leading to a high failure rate of the bonding joints [14-17]. Several research studies have sought to understand the IMC formation and the resulting phases in Ag-Al wire bonds. However, the Ag-Al IMC phases reported are not conclusive. One research group indicated Ag_4Al and Ag_2Al phases [18] and others showed $AgAl_2$, Ag_2Al and Ag_3Al phases at the Ag/Al interface [19-20]. Moreover, although many studies have reported the reliability test results of the Ag-Al wire bonds [18-21], the mechanical properties of the Ag-Al intermetallics are still unclear.

Therefore, this study aims to investigate the Ag-Al intermetallic compound formation in Ag-Al system and further evaluate its mechanical properties. First, the Ag-Al alloys with compositions from 19 to 43 at. % Al were evaluated to identify the phase equilibrium and crystal structure of the Ag-Al intermetallic phases. By studying the interfacial reaction of the Ag/Al joints, μ-Ag_3Al and δ-Ag_2Al IMC were identified to form at the Ag/Al interface and stabilize after long-time annealing at 200 °C. Finally, deformation and fracture behaviors of the bulk μ-Ag_3Al and δ-Ag_2Al were analyzed by the micro-indentation. Mechanical properties of the μ-Ag_3Al and δ-Ag_2Al were probed and discussed. In what follows, we first present the experimental design and procedures. Experimental results are then reported and discussed. Finally, a short summary is given.

3.2 Experimental Design and Procedures

Ag-Al alloy ingots were grown through the casting method followed by long-time annealing. Ag and Al shots with 99.99% purity were uniformly mixed and loaded into 150 mm long quartz tubes with 1 cm in inner diameter. After loading, the tubes were evacuated by a vacuum pump and sealed by a hydrogen torch to form capsules. The capsules were brought to and kept at 1,000 °C for 2 hours, followed by 48-hour annealing at 50 °C above

the liquidus temperature to ensure complete homogenization. The sealed samples were then water quenched to room temperature to avoid excess phase formation during the cooldown process. Subsequently, solid-state annealing was performed at 200 °C for up to 750 hours. After annealing, the ingots (40 - 45 mm long and 10 mm in diameter) were cut into disks with a thickness of 1 mm and mechanically polished for further examination. The casted ingot and disk samples after annealing are shown in Fig. 3.1. Chemical compositions, microstructures, and crystal structures of the disk specimens were characterized by a scanning electron microscope with energy dispersive X-ray spectroscopy (SEM/EDX, Philips XL-30 FEG SEM) and X-ray diffraction (XRD, Rigaku Smartlab X-ray diffractometer).

To further study the intermetallic compound formation at the Ag/Al interface, the interfacial reaction of the Ag/Al joints at 200 °C was investigated in this study. Ag-Al joints were prepared by bonding Ag disks to Al substrates using the solid-state bonding process. The bonding process was performed at 350°C with a 1,000 psi (6.89 MPa) static pressure for 450 seconds in the 0.1 torr vacuum. Subsequently, the Ag-Al joints were annealed at 200°C for 750 hours to form the Ag-Al IMC layer. To avoid possible damaging from the conventional mechanical polishing process, the cross-sectional Ag/Al joint specimens were prepared by the using focused ion beam (FIB) milling technique. The interfacial morphologies and the phase compositions were evaluated by SEM/EDX.

After identifying the intermetallic compound formation in the Ag-Al alloys and Ag/Al joints, the mechanical properties of the two stable intermetallic phases, μ-Ag_3Al and δ-Ag_2Al, were studied. The hardness, elastic modulus and fracture toughness of bulk μ-Ag_3Al and δ-Ag_2Al were analyzed by a micro-hardness tester (Buehler, Lake Bluff, IL Micromet II Micro Hardness Tester). Vickers indentation mode was used with indentation loads ranging between 100 to 1000 gf. SEM observations were conducted after indentation to determine the average lengths of the induced cracks.

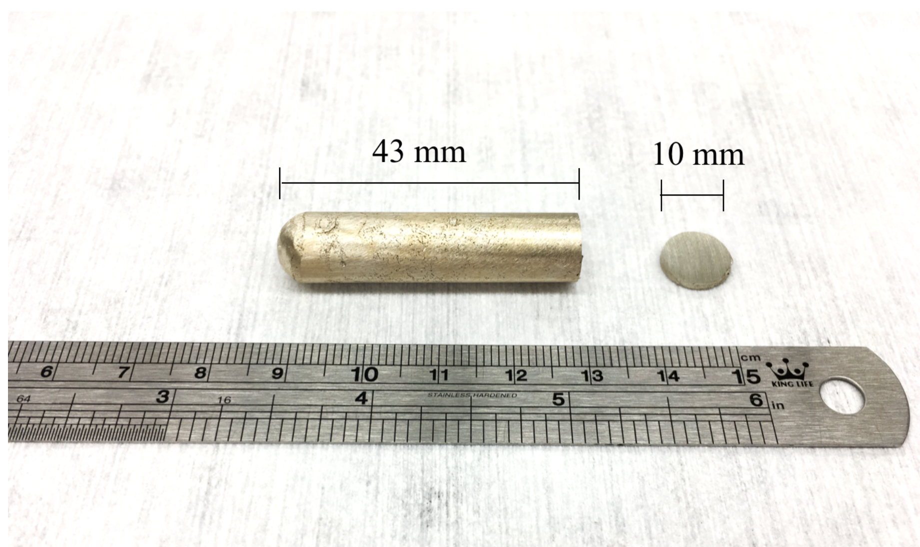

Fig. 3.1 The casted ingot and disk samples after annealing at 200 °C for 750 hours. After annealing, the ingot samples were cut into disks (10 mm in diameter and 1 mm in thickness) and mechanically polished for further examination.

3.3 Experimental Results and Discussion

3.3.1 Phase Evaluation in Ag-Al Alloys

In order to understand Ag-Al binary system and study the equilibrium Ag-Al intermetallic phases, the Ag-Al phase diagrams [22,23,24] are reviewed. In Fig. 3.2, we put the experimental phase diagram [22] and two calculated phase diagrams [23, 24] together for comparison. Below 873 k (600 °C), all three phase diagrams indicate that there are only two intermetallic phases, δ-Ag_2Al and μ-Ag_3Al. The experimental and calculated boundaries of the δ-Ag_2Al phase are in good agreement. However, the experimental and calculated boundaries of the μ-Ag_3Al phase differ significantly. Below 523 k (250 °C), the crystal structures and boundaries of μ-Ag_3Al and δ-Ag_2Al phases are sparse and incomplete. In industry, the temperature range between 125 °C and 300 °C has been chosen for the standard thermal storage testing of wire bonds, and the temperature range between 150 °C and 250 °C is the typical post-mold curing process [25]. It is critical to understand the equilibrium intermetallic phase in the Ag-Al system within this temperature range and further study its crystal structure and mechanical properties. In this study, eleven alloys with compositions from 19 to 43 at. % Al annealed at 200 °C were employed to obtain two single-phase intermetallic phases and three mixed-phase alloys, as listed in Table 3.1. The experimental results show that both intermetallic phases, μ-Ag_3Al and δ-Ag_2Al, stabilize at

200 °C after long-time annealing. In Fig. 3.2, the white spots represent a single-phase intermetallic in the sample. The black spots represent a two-phase alloy in the sample. At 200 °C, single-phase μ-Ag_3Al stabilizes in the composition range from 21.6 at. % to 22.9 at. % Al, and single-phase δ-Ag_2Al stabilizes in the composition range from 32.1 at. % to 39.9 at. % Al. In addition, three two-phase alloys, μ-Ag_3Al + (Ag), μ-Ag_3Al + δ-Ag_2Al, and δ-Ag_2Al + (Al), were produced and studied.

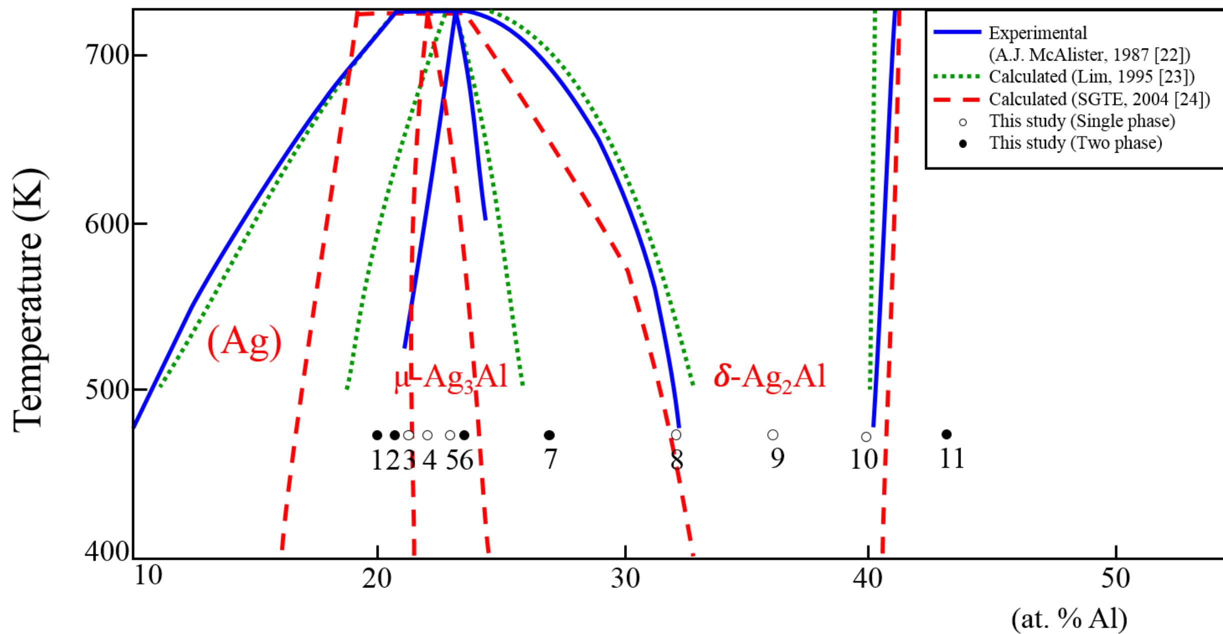

Fig. 3.2 Experimental [22] and calculated [23, 24] Ag-Al phase diagrams from 10 to 50 at. % Al at 400 to 725 K. The solid lines and dashed lines represent experimental data and calculated data, respectively. Spots marked 1-11 reveal the equilibrium phases identified in Ag-Al alloy samples no. 1 to no. 11 with composition from 19 to 43 at. % Al, as shown in Table 3.1. The white spot indicates a phase from a single-phase sample. The black spot is a phase from a two-phase alloy.

Table 3.1 Equilibrium phase and chemical compositions of the Ag-Al alloys

#	Designed alloy compositions	Micro-structure	Chemical compositions	Phases
1	Ag-19 at.% Al	Two-phase	(Ag-15.5 at.% Al) + (Ag-21.5 at.% Al)	(Ag) + μ-Ag_3Al
2	Ag-21 at.% Al	Two-phase	(Ag-15.4 at.% Al) + (Ag-21.7 at.% Al)	(Ag) + μ-Ag_3Al
3	Ag-21.5 at.% Al	Single phase	(Ag-21.6 at.% Al)	μ-Ag_3Al
4	Ag-22 at.% Al	Single phase	(Ag-22.0 at.% Al)	μ-Ag_3Al
5	Ag-23 at.% Al	Single phase	(Ag-22.9 at.% Al)	μ-Ag_3Al
6	Ag-23.5 at.% Al	Two-phase	(Ag-22.9 at.% Al) + (Ag-32.0 at.% Al)	μ-Ag_3Al + δ-Ag_2Al
7	Ag-27 at.% Al	Two-phase	(Ag-22.8 at.% Al) + (Ag-31.9 at.% Al)	μ-Ag_3Al + δ-Ag_2Al
8	Ag-32 at.% Al	Single phase	(Ag-32.1 at.% Al)	δ-Ag_2Al
9	Ag-36 at.% Al	Single phase	(Ag-35.8 at.% Al)	δ-Ag_2Al
10	Ag-40 at.% Al	Single phase	(Ag-39.9 at.% Al)	δ-Ag_2Al
11	Ag-43 at.% Al	Two-phase	(Al-2.2 at.% Ag) + (Ag-39.8 at.% Al)	(Al) + δ-Ag_2Al

In the following section, microstructures and crystal structures of the Ag-Al alloys are presented. Fig. 3.3 exhibits the SEM back-scattered electron images of the representative Ag-Al alloys, including single-phase intermetallics, μ-Ag_3Al and δ-Ag_2Al, and two-phase alloys, μ-Ag_3Al + (Ag), μ-Ag_3Al + δ-Ag_2Al, and δ-Ag_2Al + (Al). Fig. 3.4 displays the corresponding XRD spectra of the Ag-Al alloys. Results show that single-phase μ-Ag_3Al remains as the cubic structure (A13, β-Mn type) when stabilized at 200 °C, and the single-phase δ-Ag_2Al exhibits

the hexagonal structure (A3, Mg type) when stabilized at 200°C. SEM images of the homogeneous μ-Ag_3Al and δ-Ag_2Al are presented in Fig. 3.3 (a) and (b). Microstructures of the two-phase alloys, Ag-19 at. % Al alloy, Ag-27 at. % Al alloy and Ag-43 at. % Al alloy, are shown in Fig. 3.3 (c) to (f). In the Ag-19 at. % Al alloy, it is observed that the brighter (Ag) strips are embedded in the μ-Ag_3Al phase. The Al solubility detected in (Ag) solid solution is approximately 15.5 at. %. The Ag-27 at. % Al alloy exhibits a mixed-phase with μ-Ag_3Al and δ-Ag_2Al intermetallics, as shown in Fig. 3.3 (d). The brighter phase is the μ-Ag_3Al phase with 22.8 at. % Al, and the darker phase is the δ-Ag_2Al phase with 31.9 at. % Al. Fig. 3.3 (e) and (f) exhibit the hypoeutectic microstructures of the Ag-43 at. % Al alloy. The microstructure is formed by the oval-shaped δ-Ag_2Al grains surrounded by the dark intergranular (Al) phase with fine precipitates. The needle-shaped precipitates in (Al) phase, as shown in Fig. 3.3 (f), are identified as the δ-Ag_2Al phase by EDX. The Ag concentration detected in (Al) solid solution is approximately 2.2 at. %. The precipitation of the needle-shaped δ-Ag_2Al in (Al) phase is attributed to the decreased Ag solubility in (Al) phase from liquidus temperature to 200 °C. The over-saturated Ag in (Al) phase leads to the formation of secondary δ-Ag_2Al precipitates inside the (Al) solid solution phase as annealing at 200 °C. The XRD spectra of the two-phase alloys, Ag-19 at. % Al alloy, Ag-27 at. % Al alloy, and Ag-43 at. % Al alloy, are shown in Fig. 3.4 (c) to (e).

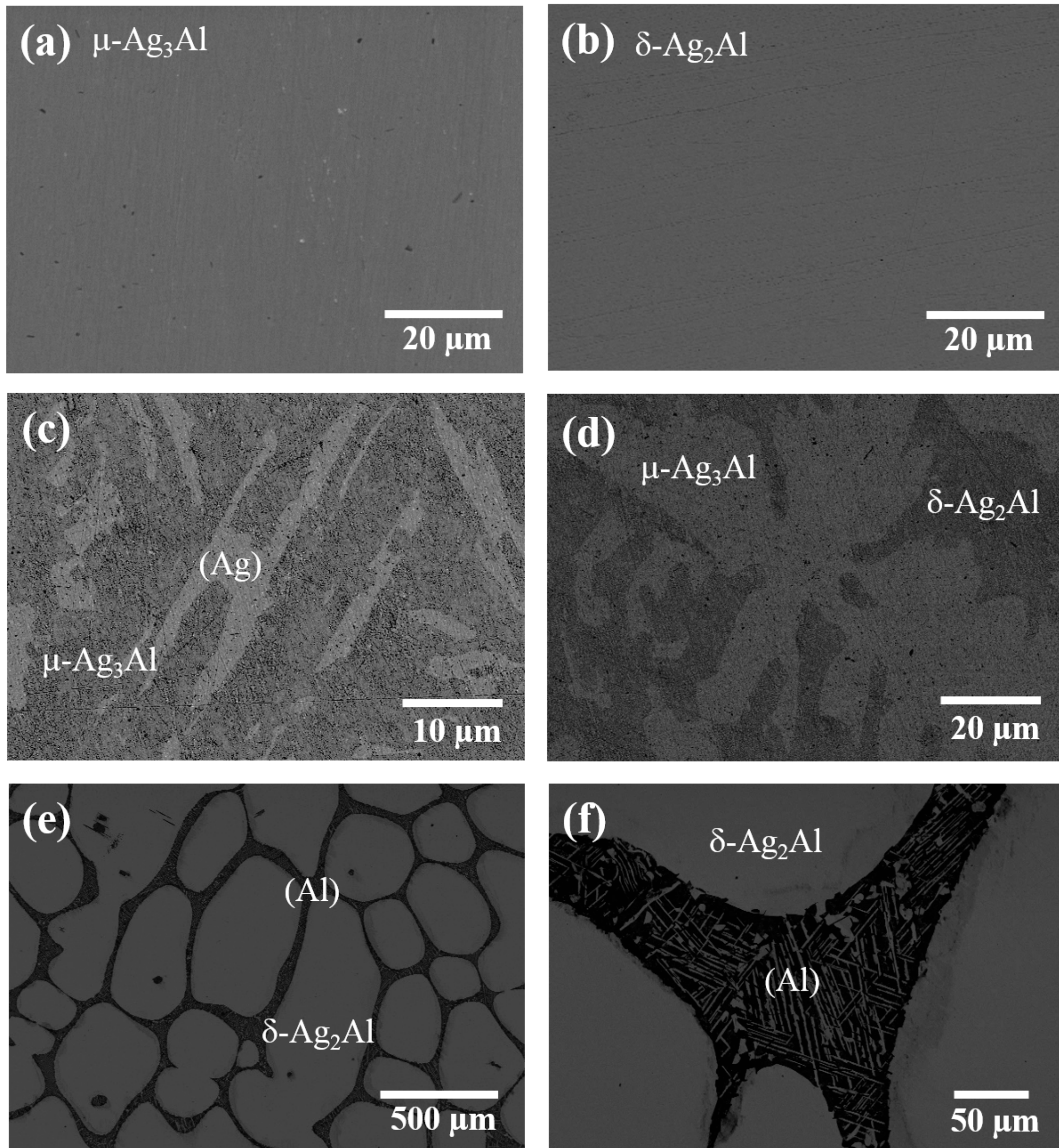

Fig. 3.3 Back-scattered SEM images showing microstructures of Ag-Al alloys. The single-phase intermetallics: (a) Ag-36 at. % Al and (b) Ag-22 at. % Al. The two-phase alloys: (c) Ag-19 at. % Al alloy, (d) Ag-27 at. % Al alloy, and (e) Ag-43 at. % Al alloy. (f) shows the enlarged area of (e). Phases identified for each sample are indicated on the image and listed in Table 3.1.

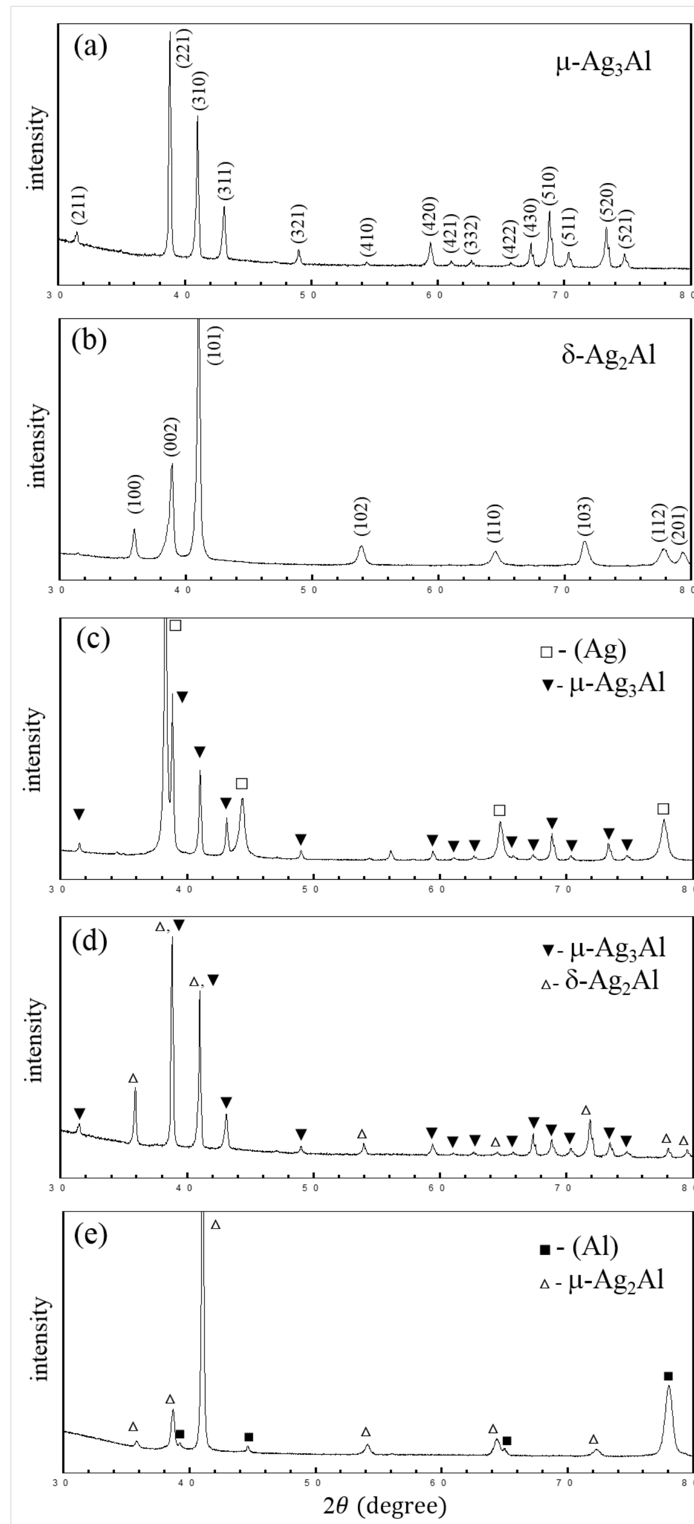

Fig. 3.4 XRD spectra of the representative Ag-Al alloys: (a) Ag-36 at. % Al, (b) Ag-22 at. % Al, (c) Ag-19 at. % Al alloy, (d) Ag-27 at. % Al alloy, and (e) Ag-43 at. % Al alloy.

3.3.2 Intermetallic Compound Formation at Ag-Al Joint Interface

The results above reveal that the Ag-Al intermetallic phases, μ-Ag_3Al and δ-Ag_2Al, can stabilize and coexist with (Ag) or (Al) in Ag-Al alloys after long-time annealing at 200 °C. To further study the Ag-Al intermetallic compound formation at the Ag/Al interface, the interfacial reaction of the Ag/Al joints at 200 °C was investigated. The Ag-Al joints were prepared by bonding Ag disks to Al substrates using the solid-state bonding process. Fig. 3.5 shows the microstructure of the Ag-Al joints after annealing at 200°C for 750 hours. On the cross-sectional SEM image, red dots marked 1-5 indicate the EDX analysis location on the interface region. The resulting phase compositions are listed in the table below. During solid-state reaction at 200 °C, the atomic inter-diffusion of Ag and Al leads to the Ag-Al IMC formation at the joint interface. The microstructure shows the Ag-Al IMC grew into both Al and Ag sides from the joint interface. From the EDX results, the scallop-type IMC which grew into the Al side was identified as δ-Ag_2Al. The layer-type IMC which grew into the Ag side was characterized as δ-Ag_2Al and μ-Ag_3Al, while the μ-Ag_3Al IMC layer was detected between the δ-Ag_2Al IMC and the Ag region. As shown in the table below, at the Ag/Al interface, the δ-Ag_2Al IMC on region 2 and 3 exhibits similar compositions, containing approximately 34.5 at. % Al. The μ-Ag_3Al IMC layer contains 22.1 at. % Al.

As reported above, after annealing the Ag-Al alloys and the Ag-Al joints at 200 °C, the phase equilibrium and crystal structures of the Ag-Al intermetallics are demonstrated. The Ag-Al joints were examined to study the IMC microstructure at the Ag/Al interface. In the industrial Ag-Al wire bonding process, bonding parameters such as electronic flame off (EFO) process and ultrasonic power could affect the Ag-Al interdiffusion and IMC nucleation at the bonding interface. Therefore, the Ag-Al IMC phases reported at the Ag-Al wire bonds interface are not conclusive. In this study, after long-term annealing the Ag-Al joints, δ-Ag_2Al and μ-Ag_3Al were identified as the thermodynamically stable phases at the Ag/Al interface. The thickness of δ-Ag_2Al and μ-Ag_3Al IMC layers in the Ag-Al joint is approximately 2 to 5 μm, which is in a comparable range to the IMC growth in Ag-Al wire bonds. Since the IMC layer is considered as the weak region within the wire bonds and could lead to brittle failure of the joint, it is important to understand the mechanical properties of the Ag-Al IMCs.

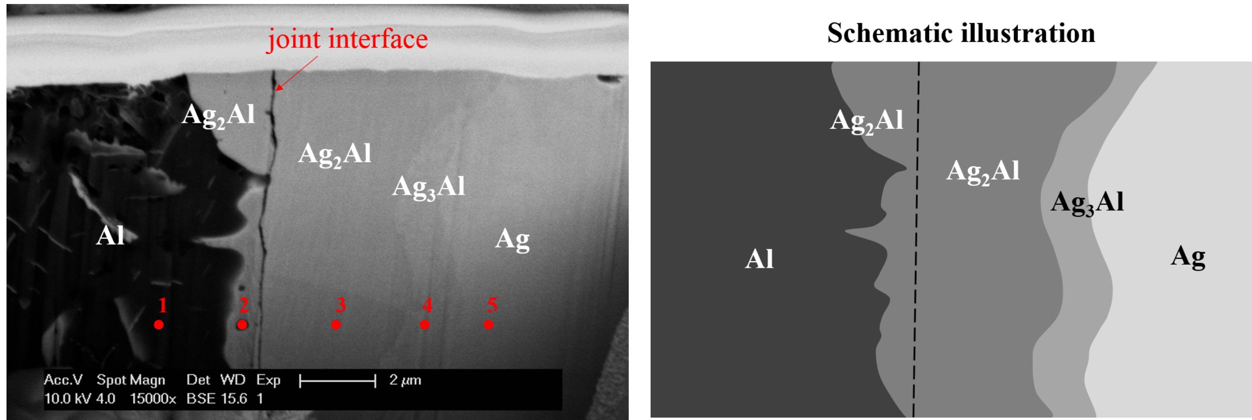

	Ag (at.%)	Al (at.%)	Remark
Region 1	0.9	99.1	Al
Region 2	65.5	34.5	Ag_2Al
Region 3	65.7	34.3	Ag_2Al
Region 4	77.9	22.1	Ag_3Al
Region 5	98.3	1.7	Ag

Fig. 3.5 The cross-sectional SEM image of the Ag-Al joints after annealing at 200°C for 750 hours. Red dots marked 1-5 indicate the EDX analysis location on the interface region. The resulting phase compositions are listed in the table below.

3.3.3 Micro-indentation Analysis of Ag_3Al and Ag_2Al

To investigate the mechanical properties of Ag-Al IMCs, the hardness and fracture toughness of the μ-Ag_3Al and δ-Ag_2Al were analyzed by the micro-indentation. Instead of using Ag-Al joints, bulk μ-Ag_3Al and δ-Ag_2Al were prepared as the indentation specimens to achieve larger analysis area for Ag-Al IMCs and avoid interface defect in Ag-Al joints. Single-phase μ-Ag_3Al with 22.0 at. % Al and δ-Ag_2Al with 35.8 at. % Al were produced. The polished

intermetallics were analyzed by a Vickers indenter using a loading force ranging between 100 to 1000 gf. The characteristic features of indentation deformation and cracks in bulk μ-Ag_3Al and δ-Ag_2Al are shown in Fig. 3.6. The hardness **(H)**, elastic modulus **(E)**, and fracture toughness **(K_{1C})** of μ-Ag_3Al and δ-Ag_2Al are listed in Table 3.2. Bulk μ-Ag_3Al exhibits significantly higher hardness than bulk δ-Ag_2Al and possesses fracture toughness value of 1.61 ± 0.13 MPa$\sqrt{\text{m}}$. The fracture toughness value is calculated by the equation [26]:

$$\mathbf{K_{1C} = 0.016 \left(\frac{E}{H}\right)^{1/2} \frac{P}{c^{3/2}}}$$

where **c** implies the length from the center of the contact to the end of the crack, **P** is the loading force, **H** is the measured hardness, and **E** is the measured elastic modulus. Fig 3.6 (a) and (b) show the indentation cracks in bulk μ-Ag_3Al under a load of 300 gf and 500 gf. It is clearly observed that cracks emanated from all four corners of the indent in μ-Ag_3Al. At a higher load of 500 g, larger indent deformation and the longer cracks were detected in μ-Ag_3Al. It is clear that the indentation crack propagation in μ-Ag_3Al demonstrates the fracture characteristics of brittle materials. In the case of bulk δ-Ag_2Al, indentation cracks could not be induced after applying loads up to 1000 gf, as shown in Fig 3.6 (c) and (d). With higher indent load, the extent of plastic deformation increases as indicated by the presence of slip bands around the indent. At a load of 1000 gf, parallel slip bands of about 10-20 μm wide formed in δ-Ag_2Al, as shown in Fig. 3.6 (d). Region A shows the slip bands nearly parallel to

the indent edge, and region B and C reveal the coarser slip bands connected to the indent edge with an identical orientation. The formation of slip bands is attributed to the plastic deformation induced by the localized stress around the indent. The presence of slip bands exhibits the ability of δ-Ag_2Al to endure plastic deformation before fracture. These microstructures imply the significant intrinsic ductility of δ-Ag_2Al intermetallic.

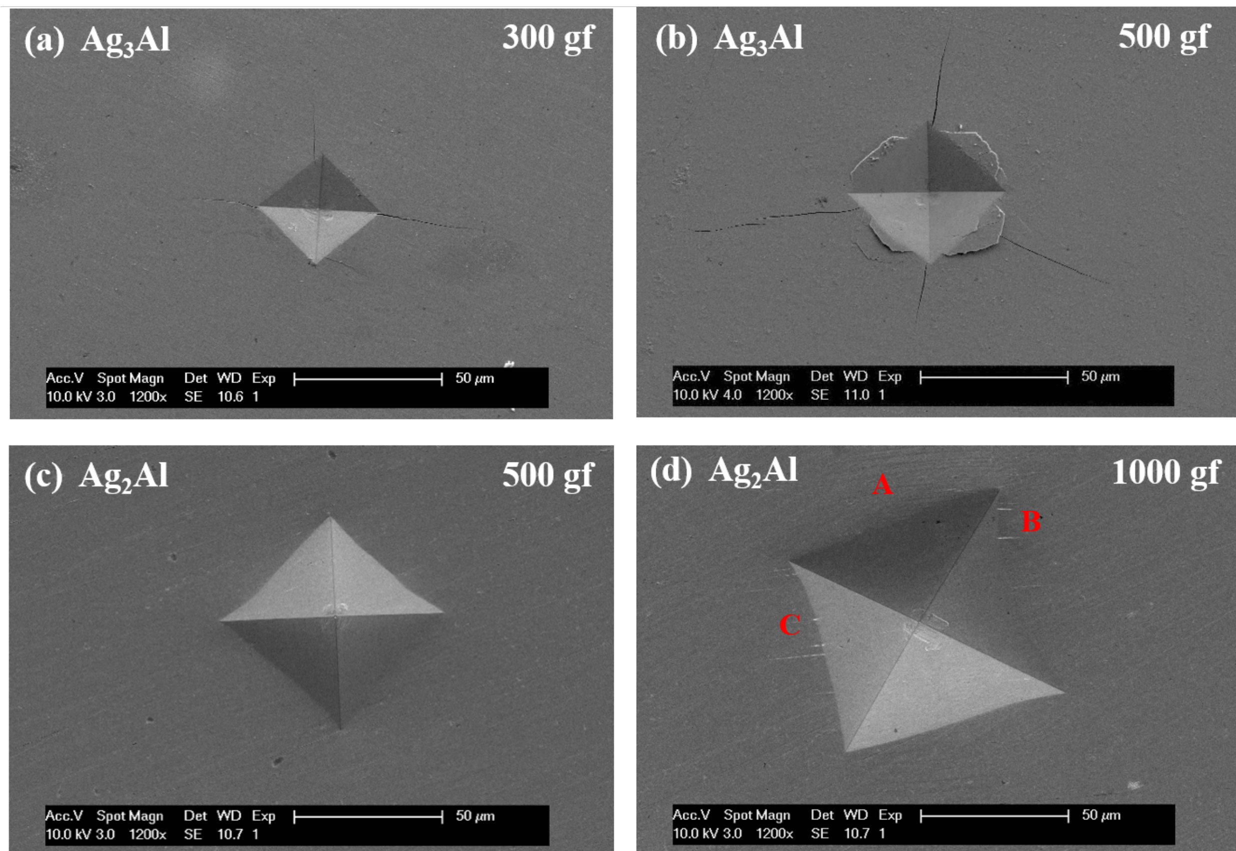

Fig. 3.6 Indentation deformation and cracks morphology in (a) bulk μ-Ag_3Al under loading of 300 gf and (b) 500 gf, and (c) bulk δ-Ag_2Al under loading of 500 gf and (d) 1000 gf. In sample (d), region A, B and C show the presence of slip bands around the indent.

Table 3.2 Phase compositions, hardness (*H*), elastic modulus (*E*), and fracture toughness (*Kc*) of the μ-Ag_3Al and δ-Ag_2Al.

Phase	Composition	Hardness (MPa)	Elastic modulus (GPa)	Fracture toughness (MPa*√m)
μ-Ag_3Al	Ag-22 at.% Al	2207 ± 141	110 ± 2.5	1.61 ± 0.13
δ-Ag_2Al	Ag-35.8 at.% Al	1222 ± 94	106 ± 2.1	-

As a result, among two Ag-Al intermetallics, μ-Ag_3Al demonstrates the brittle fracture characteristics in the micro-indentation analysis. The measured results reveal that μ-Ag_3Al exhibits significantly higher hardness and lower fracture toughness as compared to δ-Ag_2Al. Therefore, the formation of interfacial μ-Ag_3Al IMC could lead to brittle fracture at the Ag-Al wire bonding interface and degrade the joint reliability. Moreover, as crystal structures of μ-Ag_3Al and δ-Ag_2Al are demonstrated in this study, it is important to discuss the effect of lattice mismatch between the IMC phases and substrates on the Ag-Al joint reliability. In the Ag-Al system, δ-Ag_2Al with hexagonal structure and Al with face-centered-cubic form a well-lattice-matched δ-Ag_2Al/Al interface [27]. However, large lattice mismatch between the μ-Ag_3Al/Ag interface is expected due to the complex cubic structure of μ-Ag_3Al (A13, β-Mn type). In Ag-Al wire bonds, the large lattice mismatch between the μ-Ag_3Al and Ag could induce lattice strain and defects at the compound interface, decreasing the interfacial stability. Due to the brittle nature of μ-Ag_3Al and the large lattice mismatch at the μ-Ag_3Al/Ag

interface, suppressing the formation of μ-Ag_3Al IMC is extremely important to enhance the Ag-Al joint reliability. For Ag-Al wire bonds, adding some elements to Ag wires might reduce the Ag-Al IMC growth or change the phase compositions of the Ag-Al IMC. Recently, Au and Pd elements have been added to produce Ag alloy wires. Ternary IMC phases, $(Ag, Pd)_2Al$, $(Ag, Pd)_3Al_2$ and $(Au,Ag)_4Al$, were probed at the Ag-Pd/Al and Ag-Au-Pd/Al interface [10,28]. However, the crystal structures and mechanical properties of these ternary phases are still unclear and need to be addressed in future.

3.4 Summary

In this study, experiments were established to investigate the Ag-Al intermetallic compound (IMC) formation in Ag-Al system and evaluate its mechanical properties. First, the Ag-Al alloys of eleven compositions were grown and evaluated to identify the phase equilibrium and crystal structure of the Ag-Al intermetallic phases. Microstructures and phase compositions of the designed Ag-Al alloys are presented and discussed. The interfacial reaction of the Ag/Al joints at 200 °C was investigated. The μ-Ag_3Al and δ-Ag_2Al IMC were identified to form at the Ag/Al interface and stabilize after long-time annealing at 200 °C. Finally, deformation and fracture behaviors of the bulk μ-Ag_3Al and δ-Ag_2Al were analyzed

by the micro-indentation. In μ-Ag_3Al, the indentation cracks propagation demonstrates the brittle fracture characteristics of μ-Ag_3Al. In δ-Ag_2Al, the absence of indentation cracks and observed slip bands imply the intrinsic ductility of δ-Ag_2Al. The measured results reveal that μ-Ag_3Al exhibits remarkably higher hardness and lower fracture toughness as compared to δ-Ag_2Al. Correlations between the mechanical properties of the Ag-Al IMC and the Ag-Al joint reliability are discussed. This research reveals the phase equilibrium and crystal structures of the Ag-Al IMCs and quantifies the intrinsic mechanical properties of μ-Ag_3Al and δ-Ag_2Al, providing an important reference for securing the Ag-Al wire bonding reliability.

3.5 References

1. C. Harper, Electronic packaging and interconnection handbook, McGraw-Hill, Inc., 2004.
2. E. R. R. Tummala and E. J. Rymaszewski, Microelectronics Packaging Handbook, 1997.
3. G. G. Harman, Wire bonding in microelectronics, McGraw-Hill, 2010.
4. A. Dasgupta and M. Pecht, "Material failure mechanisms and damage models," IEEE Trans. Reliab., vol. 40, no. 5, pp. 531-536, 1991.
5. C. Breach and F. Wulff, "New observations on intermetallic compound formation in gold ball bonds: General growth patterns and identification of two forms of Au 4

Al," Microelectronics reliability, vol. 44, no. 6, pp. 973-981, 2004.

6. C. Breach, "What is the future of bonding wire? will copper entirely replace gold?" Gold Bulletin, vol. 43, no. 3, pp. 150-168, 2010.

7. C. L. Gan and U. Hashim, "Evolutions of bonding wires used in semiconductor electronics: Perspective over 25 years," J. Mater. Sci: Mater. Electron., vol. 26, no. 7, pp. 4412-4424, 2015.

8. Z. Zhong, "Overview of wire bonding using copper wire or insulated wire," Microelectronics Reliability, vol. 51, no. 1, pp. 4-12, 2011.

9. B. K. Appelt, A. Tseng, C. Chen and Y. Lai, "Fine pitch copper wire bonding in high volume production," Microelectronics Reliability, vol. 51, no. 1, pp. 13-20, 2011.

10. R. Guo, T. Hang, D. Mao, M. Li, K. Qian, Z. Lv and H. Chiu, "Behavior of intermetallics formation and evolution in Ag–8Au–3Pd alloy wire bonds," J. Alloys Compounds, vol. 588, pp. 622-627, 2014.

11. C. Yu, C. Chan, L. Chan and K. Hsieh, "Cu wire bond microstructure analysis and failure mechanism," Microelectronics reliability, vol. 51, no. 1, pp. 119-124, 2011.

12. T. Chuang, C. Tsai, H. Wang, C. Chang, C. Chuang, J. Lee and H. Tsai, "Effects of annealing twins on the grain growth and mechanical properties of Ag-8Au-3Pd bonding wires," J Electron Mater, vol. 41, no. 11, pp. 3215-3222, 2012.

13. C. Cheng, H. Hsiao, S. Chu, Y. Shieh, C. Sun and C. Peng, "Low cost silver alloy wire bonding with excellent reliability performance," in Electronic Components and Technology Conference (ECTC), 2013 IEEE 63rd, pp. 1569-1573, 2013.
14. K. Sakuma, K. Sueoka, S. Kohara, K. Matsumoto, H. Noma, T. Aoki, Y. Oyama, H. Nishiwaki, P. Andry and C. Tsang, "IMC bonding for 3D interconnection," in Electronic Components and Technology Conference (ECTC), 2010 Proceedings 60th, pp. 864-871, 2010.
15. Y. C. Jang, S. Y. Park, H. D. Kim, Y. C. Ko, K. W. Koo, M. R. Choi, H. G. Kim, N. K. Cho, I. T. Kang and J. H. Yee, "Study of intermetallic compound growth and failure mechanisms in long term reliability of silver bonding wire," in Electronics Packaging Technology Conference (EPTC), 2014 IEEE 16th, pp. 704-708, 2014.
16. C. Lu, "Review on silver wire bonding," in Microsystems, Packaging, Assembly and Circuits Technology Conference (IMPACT), 2013 8th International, pp. 226-229, 2013.
17. J. Xi, N. Mendoza, K. Chen, T. Yang, E. Reyes, S. Bezuk, J. Lin, S. Ke and E. Chen, "Evaluation of Ag wire reliability on fine pitch wire bonding," in Electronic Components and Technology Conference (ECTC), 2015 IEEE 65th, pp. 1392-1395, 2015.
18. K. Yoo, C. Uhm, T. Kwon, J. Cho and J. Moon, "Reliability study of low cost alternative Ag bonding wire with various bond pad materials," in Electronics Packaging Technology Conference, EPTC'09. 11th, pp. 851-857, 2009.

19. T. Chuang, C. Chang, C. Chuang, J. Lee and H. Tsai, "Formation and growth of intermetallics in an annealing-twinned Ag-8Au-3Pd wire bonding package during reliability tests," IEEE Transactions on Components, Packaging and Manufacturing Technology, vol. 3, no. 1, pp. 3-9, 2013.
20. L. J. Kai, L. Y. Hung, L. W. Wu, M. Y. Chiang, D. S. Jiang, C. Huang and Y. P. Wang, "Silver alloy wire bonding," in Electronic Components and Technology Conference (ECTC), 2012 IEEE 62nd, pp. 1163-1168, 2012.
21. M. Schneider-Ramelow and C. Ehrhardt, "The reliability of wire bonding using Ag and Al," Microelectronics Reliability, vol. 63, pp. 336-341, 2016.
22. A. McAlister, "The Ag-Al (silver-aluminum) system," Bulletin of Alloy Phase Diagrams, vol. 8, no. 6, pp. 526-533, 1987.
23. S. Lim, P. Rossiter and J. Tibballs, "Assessment of the al-ag binary phase diagram," Calphad, vol. 19, no. 2, pp. 131-141, 1995.
24. SGTE Binary Phase Diagram Collection, http://www.sgte.org.
25. JESD22-A103E, High temperature storage life, JEDEC, 2015.
26. D. Harding, W. Oliver and G. Pharr, "Cracking during nanoindentation and its use in the measurement of fracture toughness, " MRS Online Proceedings Library Archive. vol. 356, 1994.

27. S. Senapati, "Evolution of lamellar structures in Al-Ag alloys", 2005.

28. W. Huang, K. Lin, Y. Lin and Y. Cheng, "The Intermetallic Compound Formation for the Wire Bond Between an Al Pad and Ag-xPd Alloy Wire," J. Electron. Mater. vol. 45 pp. 6130-6136, 2016.

Chapter Four

A corrosion study of Ag-Al intermetallic compounds in chlorine-containing epoxy molding compounds

4.1 Introduction

Wire bonding technique has been extensively used to interconnect chips and substrates of microelectronic packages [1-3]. Gold (Au) wire had been most popular for decades, providing excellent workability and stable chemical properties [4,5]. However, the rising gold price has motivated the packaging industry to look for alternative wire materials such as silver (Ag) and copper (Cu) [5-9]. Recently, several packaging companies have bonded Cu wires on aluminum (Al) bond-pads in production. The reaction on Cu/Al interface and Cu wire-bond reliability have been reported [5,6]. Since Cu wires get oxidized easily and are harder than Au and Ag alloy wires, the process window of Cu wire bonding is narrower. Special bonding equipment are usually needed. Other issues on Cu wire-bonds are splashing on Al pads and Si chip cratering [8].

Most recently, Ag alloy wires have been chosen as a possible alternative [9,10]. Compared to Cu wires, Ag alloy wires have lower oxidation rate and higher ductility. It had been reported that Ag alloy wire bonding exhibits wider process window and causes less Al

pad splash and silicon damage [11]. In choosing a wire material, one important thing to consider is how it bonds to the Al pads [12,13]. Several research works have shown that the bonding on the Ag-Al interface is caused by intermetallic compound (IMC) formation [14-16]. Based on the Ag-Al phase diagrams [17,18] and experiment results, the main IMCs are Ag_3Al and Ag_2Al [15-18]. Reliability of Ag alloy wire-bonds has been evaluated under high temperature and high humidity test conditions [11,13-16]. In high temperature storage test (HTS), Ag alloy wire-bonds pass industrial reliability standard [11,14,15]. Microstructures of Ag alloy wire-bonds exhibit homogenous IMC growth without cracks or Kirkendall void formation. No electrical degradation is detected. Under humidity storage test conditions, wire-bond failure rate increases [13,16,19]. In Highly Accelerated temperature/humidity Stress Test (HAST) and Pressure Cooker Test (PCT), cracks and voids incur at the Ag/Al bonding interface, causing wire-bond failure. Moisture-induced corrosion at the Ag/Al bonding interface seems to be the root cause of this failure. Similar corrosion effect is also observed in Au-Al and Cu-Al wire-bonds [20-23]. The corrosion is strongly associated with halogen content, such as chlorine (Cl), in the epoxy molding compounds (EMCs). However, the corrosion mechanism of Ag-Al wire-bonds is still unclear.

In this research, to find out how Ag-Al wire-bonds are corroded, experiments are designed to emulate the wire-bond environment and conditions. As a first step, instead of

using actual wire-bonds, bulk Ag-Al joints are produced with enough Ag_3Al and Ag_2Al volume for HAST and corrosion measurements. Since Ag-Al wire-bonds consist of Ag alloy wire, Ag_3Al and Ag_2Al on the interface, and the Al pad, corrosion experiment of each component with EMC is conducted with HAST for 125 hours. The experimental results show that corrosion occurs with Ag_3Al and Ag_2Al but not with Ag or Al. A corrosion chemical model is proposed to establish the reactions of Ag_3Al and Ag_2Al compounds with chlorine-containing EMC.

4.2 Experimental Design and Procedures

A typical wire bond is too small to produce enough corrosion volume for analysis. To emulate Ag-Al wire-bonds for the purpose of corrosion study, Ag-Al joints are prepared by bonding Ag disks to Al substrates using the solid-state bonding process. The bonding process was performed at 450°C with a 1000 psi static pressure for 10 minutes in 0.1 torr vacuum. Subsequently, the Ag-Al joints are annealed at 300°C for 100 hours to grow enough Ag-Al IMC layer. The resulting Ag-Al joints are molded in EMC for HAST. The test conditions are 130°C and 85% relative humidity (RH) without applied bias. High chlorine content (1000 ppm) is added to the EMC to accelerate the corrosion reaction and to shorten the experiment

time. The chlorine content is controlled by the amount of hydrolyzable chloride (3-chloro-1-propanol) added into the EMC.

To measure corrosion rates, corrosion experiments of bulk Ag, Ag_3Al, Ag_2Al and Al disks with EMC are conducted, respectively. To produce Ag_3Al and Ag_2Al disks, single-phase Ag_3Al and Ag_2Al ingots are grown by a casting method. Ag-35 at. % Al mixture and Ag-22 at. % Al mixture are, respectively, loaded in quartz tubes and sealed in vacuum to form capsules. The capsules are brought to 1,273 K (1,000°C) and stay at this temperature for 5 hours. This is followed by water quenching to room temperature and solid-state annealing at 473 K (200°C) for 750 hours. X-ray diffraction (XRD) analysis is used to confirm that these ingots are indeed single phase Ag_3Al and Ag_2Al, respectively. The ingots are cut into disks and polished for corrosion experiments. The bulk disks are encapsulated in EMC and tested at 130°C and 85% RH (HAST) for 25, 50 and 125 hours, respectively.

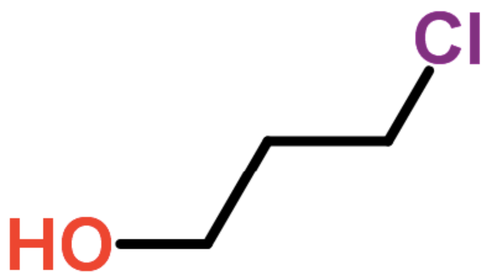

Fig. 4.1 Chemical structure of 3-chloro-1-propanol.

To study the corrosion reactions, the encapsulating EMC samples are cut in cross-section and fine polished for optical microscopy (OM) inspection and scanning electron microscopy/energy dispersive X-ray spectroscopy (SEM/EDX, FEI Philips XL-30, FEG SEM) examinations in back-scattered electron (BSE) mode.

4.3 Experimental Results and Discussion

4.3.1 Corrosion Experiment of Ag-Al joints in EMC under HAST

As presented in previous section, Ag-Al joints are prepared by bonding Ag disks to Al substrates using solid-state bonding process. After annealing at 300°C for 100 hours to grow IMC, the resulting Ag-Al joints are molded in EMC. EMC with high chlorine content (1,000 ppm) is used to accelerate corrosion reactions. The molded Ag-Al joints are tested by HAST (130°C, 85% RH) for 100 hours. Fig. 4.2 displays the cross section optical microscopy and back-scattered electron images of representative samples. Before HAST, a 20 μm thick Ag-Al IMC layer is clearly observed in Figs. 4.2 (a) and (b). Based on compositions measured by EDX analysis, shown in Table 4.1, the IMC layer consists of both Ag_3Al and Ag_2Al. Figs. 4.2 (c) and (d) exhibit a sample after HAST. As shown in the optical image, Fig. 4.2 (c), corrosion mainly occurred in the IMC area, and no reaction was observed on Ag or Al. The IMC layer

had turned black with continuous cracks. Corrosion and cracks propagated through the entire IMC layer to break it down to small particles and fragments. This makes it difficult to achieve nice polishing on cross section surfaces. The particles and fragments got onto the Ag and Al areas during the polishing process, causing scratches on the sample cross section, as exhibited in Fig. 4.2 (c). In the corroded IMC region, EDX analysis did not pick up compositions associated with Ag_3Al and Ag_2Al compounds, indicating that the original IMC layer had been completely disintegrated. On the corroded region, EDX analysis picked up elements Ag, Al, O, and Cl, as shown in Table 4.1. From EDX results, the corrosion in Ag-Al joints was caused by the oxidation of the IMC region in the presence of moisture and chlorine. At high humidity ambient, water vapor can penetrate into EMC and react with hydrolyzable chloride in EMC to produce Cl^- ions [24,25]. Water and Cl^- ions can diffuse and reach the Ag/Al interface and initiate the IMC corrosion. As water and Cl^- ions penetrate through the corroded IMC region, the corrosion action can continue towards the center of the Ag-Al joint interface.

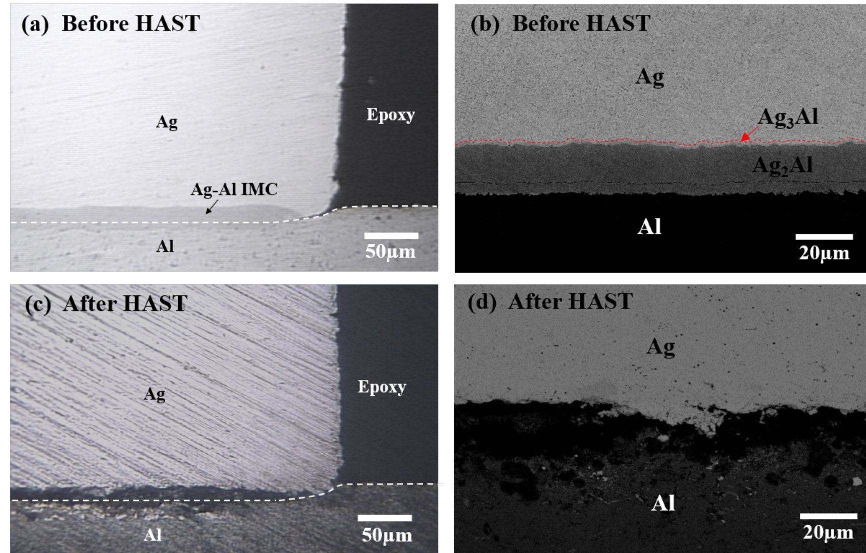

Fig. 4.2 Cross-sectional images of the Ag-Al joints molded in EMC: (a) optical microscopy image before HAST, (b) back-scattered electron image before HAST, (c) optical image after HAST, (d) back-scattered electron image after HAST

Table 4.1 Compositions (at.%) of intermetallic compound layer in the Ag-Al joint molded in EMC before and after HAST.

	Ag	Al	O	Cl	Remark
Before HAST	78.8	21.2	0.0	0.0	Ag_3Al
	66.2	33.8	0.0	0.0	Ag_2Al
After HAST	25.0	33.9	58.9	1.2	Corrosion region

4.3.2 Corrosion Experiment of Ag_3Al and Ag_2Al in EMC under HAST

The results reported above have clearly indicated that in Ag-Al joints, corrosion by Cl^- ions mainly occur at the Ag-Al IMC region. To find out the IMC corrosion rate and investigate

the microstructures and compositions of the corroded IMC region, reaction experiments with bulk Ag_3Al and Ag_2Al disks were designed and performed. First, single-phase Ag_3Al and Ag_2Al ingots were produced. Fig. 4.3 displays the XRD spectra and EDX analysis compositions of the Ag_3Al and Ag_2Al ingots. For the Ag_3Al sample, all XRD peaks belong to Ag_3Al lattice that has cubic structure (A13, β-Mn type). For the Ag_2Al sample, all peaks belong to Ag_2Al lattice that has hexagonal structure (A3, Mg type). The Ag_3Al and Ag_2Al ingots were cut into disk samples and polished. The polished samples were encapsulated in EMC and tested by HAST (130°C, 85% RH) for 25, 50, and 125 hours, respectively. Fig. 4.4 exhibits the cross-section SEM back-scattered electron images of molded Ag_3Al and Ag_2Al samples after HAST for different times. It is clearly observed that corrosion occurred on both Ag_3Al and Ag_2Al disks under HAST. The images show continuous corrosion regions of depth up to 100 μm on both Ag_3Al and Ag_2Al disks. An important fact to confirm is whether Ag or Al can be corroded by chlorine-containing EMC. Reaction experiments with Ag and Al disks were performed under the same HAST conditions. As presented in Fig. 4.5, the cross-section SEM image shows no detectable corrosion on the bulk Ag sample encapsulated in chlorine-containing EMC after HAST for 125 hours. The same is true for the bulk Al sample. The above results demonstrate that corrosion by chlorine ions occurs on both Ag_3Al and Ag_2Al, and no corrosion is found on

Ag or Al sample. In the following paragraphs, the corrosion mechanisms of Ag_3Al and Ag_2Al will be presented, following by a proposed corrosion model.

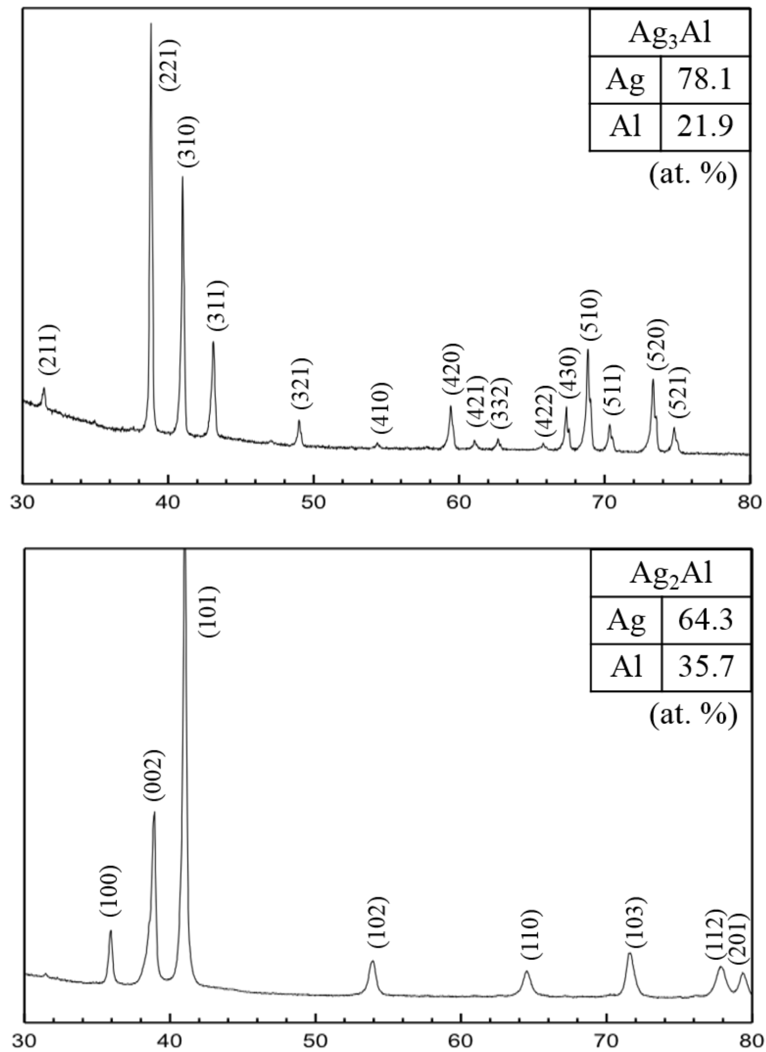

Fig. 4.3 EDX composition analysis results and the XRD spectrum of the Ag_3Al and Ag_2Al intermetallic alloys.

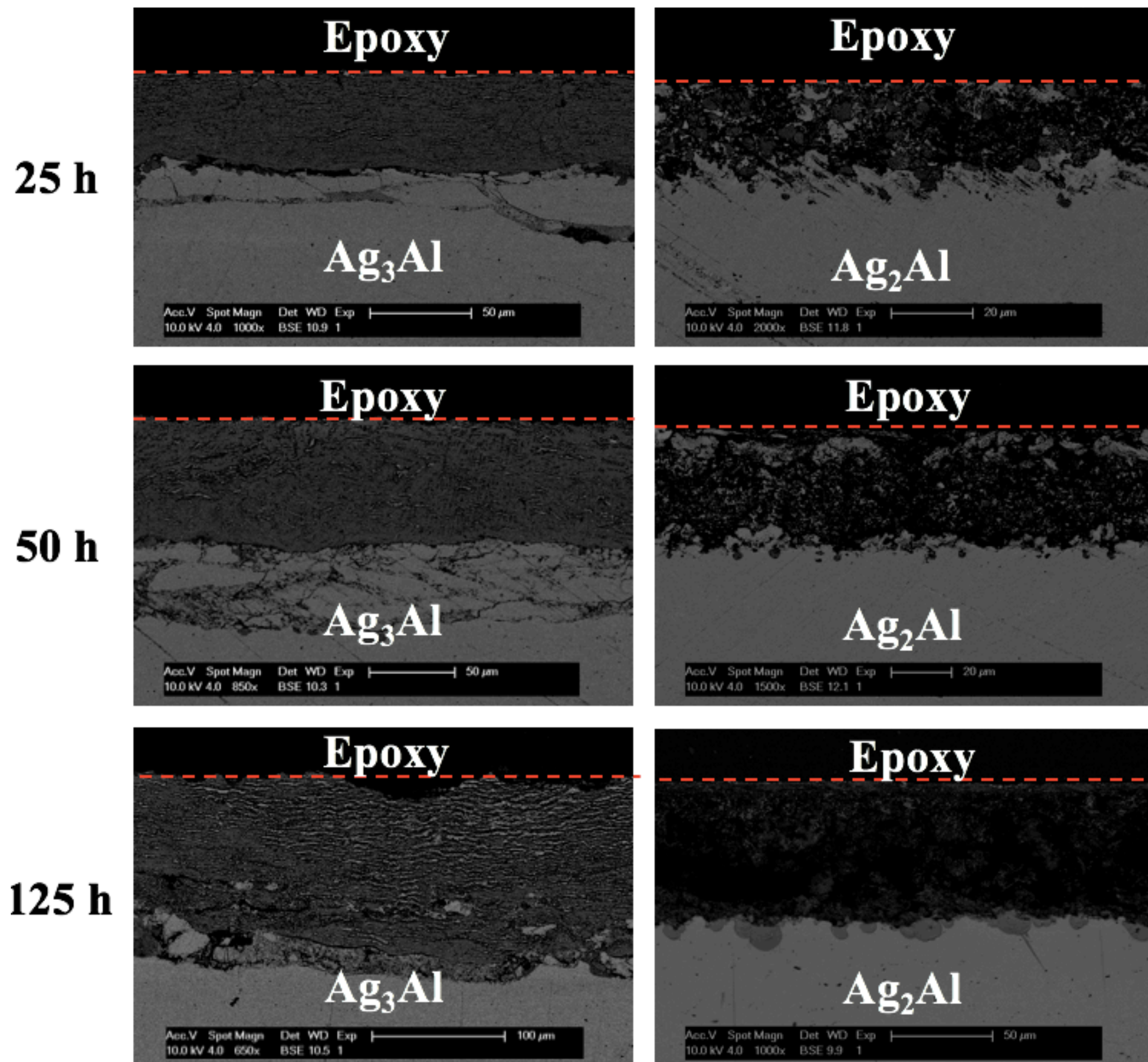

Fig. 4.4 The cross-sectional SEM back-scattered electron images of the Ag_3Al and Ag_2Al compounds molded in epoxy molding compounds after HAST for 25, 50, and 125 hours.

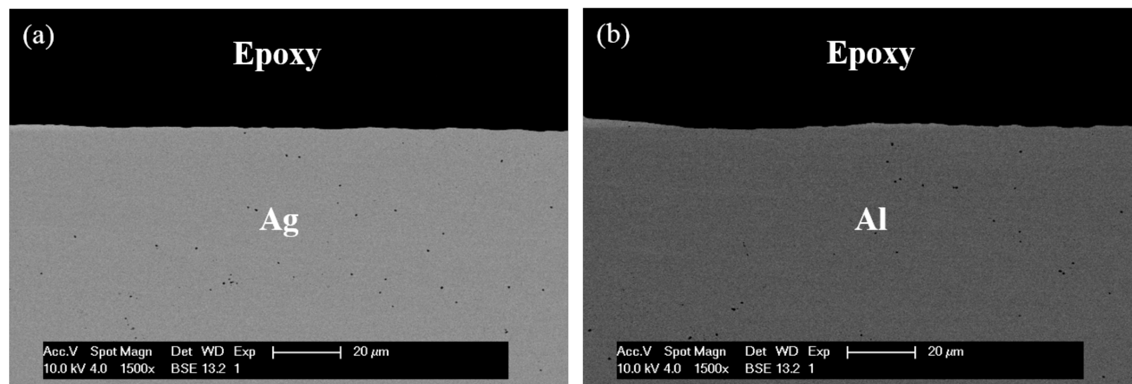

Fig. 4.5 The cross-sectional SEM back-scattered electron images of (a) Ag and (b) Al molded in epoxy molding compounds after HAST for 125 hours.

Fig. 4.6 (a) displays the microstructures of the corrosion region and corrosion-induced cracks in the Ag_3Al compound. Fig. 4.6 (b) shows an enlarged region. On the SEM images, red dots marked 1 - 12 indicate the EDX analysis location on the corrosion region. The resulting element compositions are listed in a table below. The microstructures consist of numerous submicron voids and cracks that were produced by the corrosion reactions. EDX analysis picked up element Cl in the corrosion region and in the vicinity of the cracks. It is interesting to observe that the corrosion-induced cracks propagate through the dark corrosion region and extend into the Ag_3Al compound. Moisture and Cl^- ions could penetrate through the cracks and voids in the corrosion region and accelerate the corrosion propagation into the Ag_3Al compound. The dispersed bright phase in the porous corrosion region was identified as Ag precipitates, as shown in pt. 1 - 5. On the dark regions, EDX analysis exhibits significant

variations in Ag, Al, and O element contents, as shown in pt. 6 - 10. The EDX energy spectra of representative analysis locations are displayed in Fig 4.6 (c). At randomly selected locations on dark regions, such as pt. 7 and pt. 9, EDX analysis detected dominant Al and O signals. Since silver oxide is thermodynamically unstable, the Al and O signals could come from aluminum oxide. It is probable that the corrosion reaction caused by moisture and Cl^- ions converts the Ag_3Al compound into corroded region consisting of aluminum oxide and dispersed Ag precipitates.

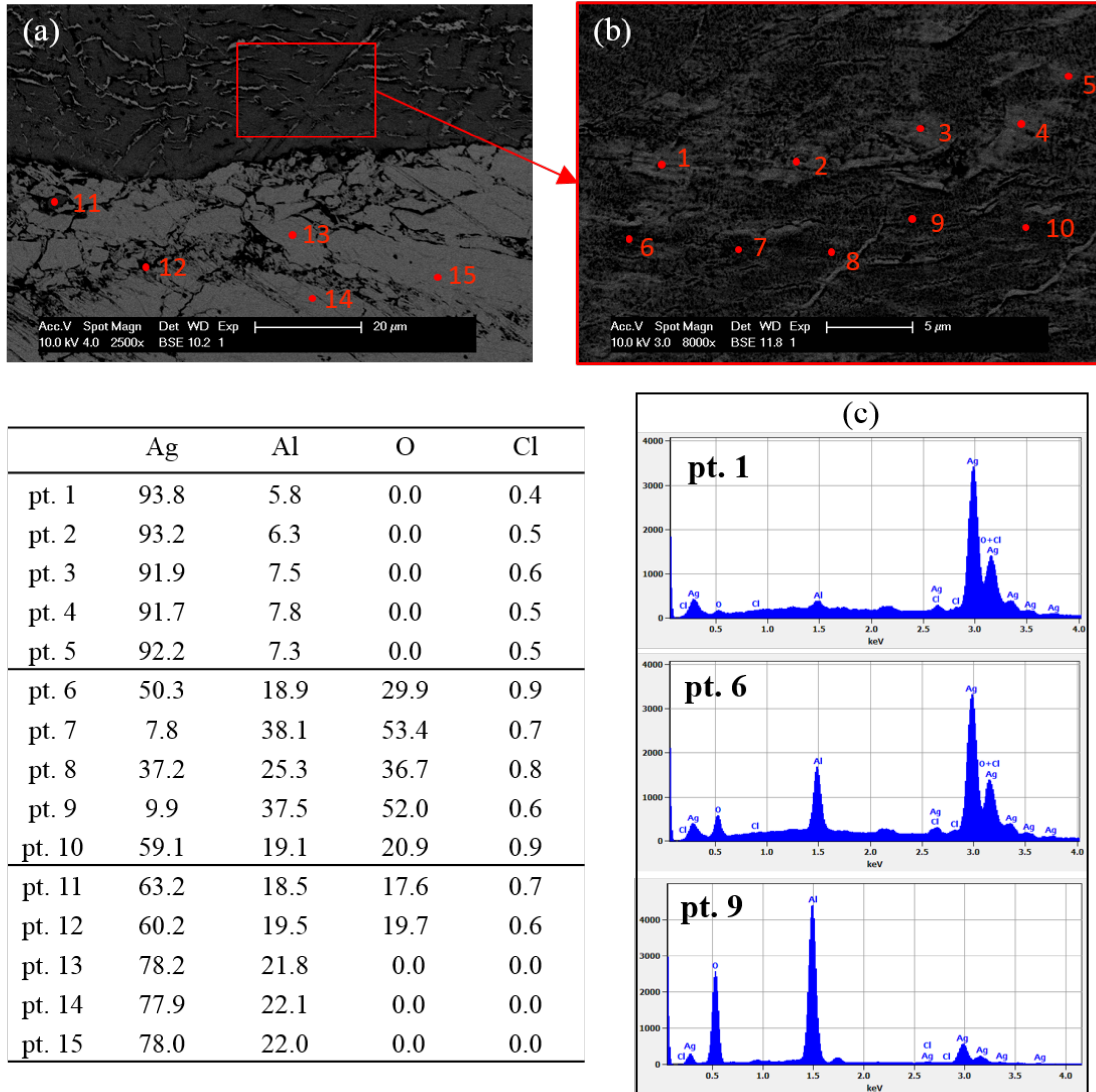

	Ag	Al	O	Cl
pt. 1	93.8	5.8	0.0	0.4
pt. 2	93.2	6.3	0.0	0.5
pt. 3	91.9	7.5	0.0	0.6
pt. 4	91.7	7.8	0.0	0.5
pt. 5	92.2	7.3	0.0	0.5
pt. 6	50.3	18.9	29.9	0.9
pt. 7	7.8	38.1	53.4	0.7
pt. 8	37.2	25.3	36.7	0.8
pt. 9	9.9	37.5	52.0	0.6
pt. 10	59.1	19.1	20.9	0.9
pt. 11	63.2	18.5	17.6	0.7
pt. 12	60.2	19.5	19.7	0.6
pt. 13	78.2	21.8	0.0	0.0
pt. 14	77.9	22.1	0.0	0.0
pt. 15	78.0	22.0	0.0	0.0

Fig. 4.6 (a) The SEM back-scattered electron images and EDX composition analysis of the corroded Ag_3Al compound after 50-hour HAST. (b) The SEM image of an enlarged corrosion region. Red dots marked by 1-12 indicate the EDX analysis locations. The resulting element compositions are listed in the table. (c) The EDX energy spectra of representative analysis locations.

Fig. 4.7 shows the corrosion region in a Ag_2Al sample and the EDX results after the same HAST conditions. It is seen that there are large number of voids in the corrosion region, but there are no propagating cracks as observed on the corroded Ag_3Al in Fig. 4.6. The high magnification image, Fig. 4.7(b), exhibits a seemingly random distribution of granular dark phase and irregular bright phase. EDX analysis identified the dispersed bright phase as Ag precipitates with similar compositions that on the corroded Ag_3Al. The dark region was identified as mixed phase containing Ag, Al, O and Cl. Higher Al and O contents were detected in the dark corrosion region of Ag_2Al as compared to Ag_3Al, which could possibly be attributed to higher proportion of aluminum oxide product in the corroded Ag_2Al. Fig. 4.8 displays the result of EDX elemental mapping of Ag, Al, O, and Cl element on the corroded Ag_2Al under high magnification. It is interesting to observe that Cl distributed in the irregular black region around the voids and cracks on the corroded Ag_2Al. Since the EDX mapping reveals complementary distribution of Cl and Ag, the relatively Cl-rich region is most likely attributed to the formation of aluminum chloride during the corrosion reaction. As aluminum chloride is considered chemically unstable, it can be readily hydrolyzed by moisture or consequently changed into aluminum oxide, leading to micro-void and micro-crack formation in the corrosion region.

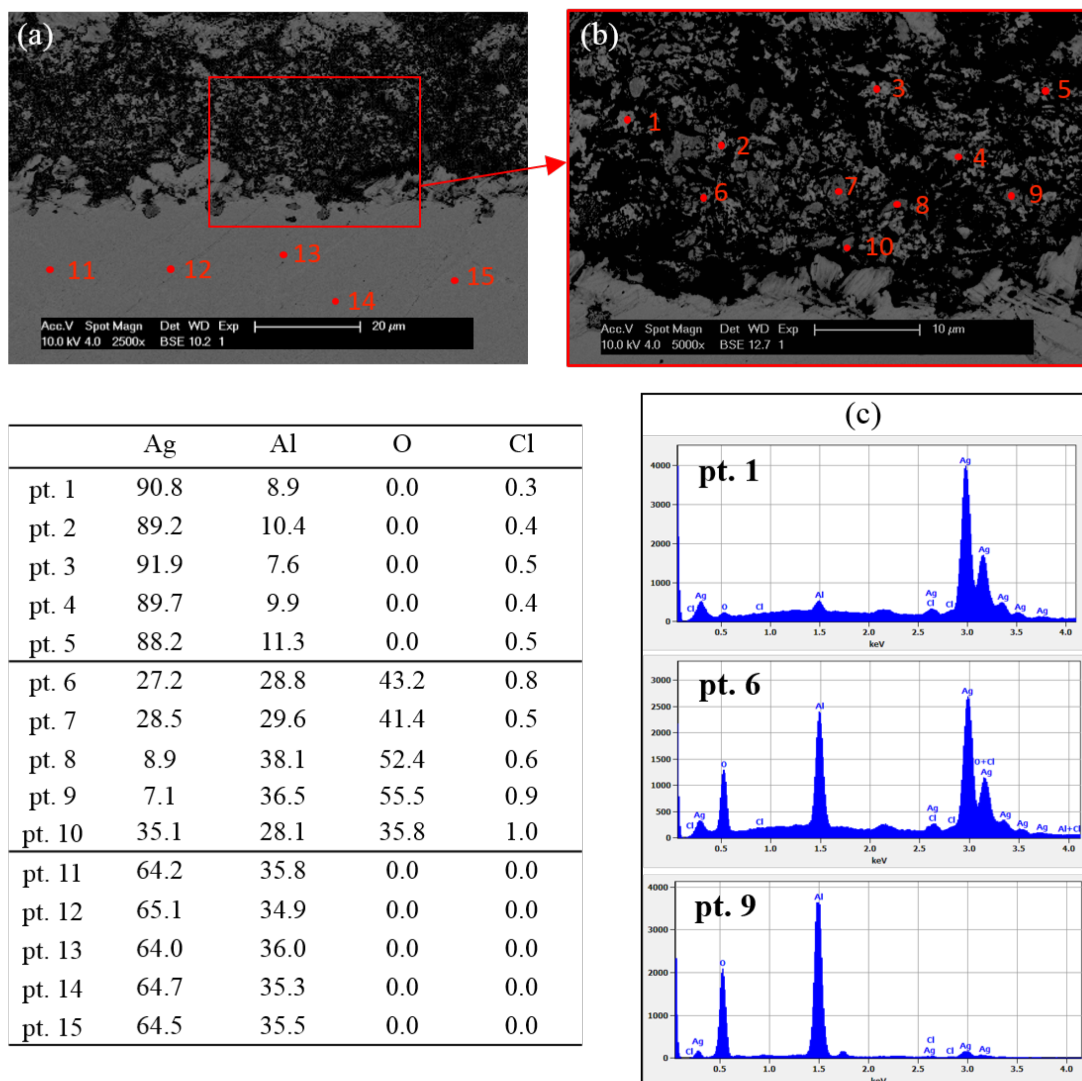

	Ag	Al	O	Cl
pt. 1	90.8	8.9	0.0	0.3
pt. 2	89.2	10.4	0.0	0.4
pt. 3	91.9	7.6	0.0	0.5
pt. 4	89.7	9.9	0.0	0.4
pt. 5	88.2	11.3	0.0	0.5
pt. 6	27.2	28.8	43.2	0.8
pt. 7	28.5	29.6	41.4	0.5
pt. 8	8.9	38.1	52.4	0.6
pt. 9	7.1	36.5	55.5	0.9
pt. 10	35.1	28.1	35.8	1.0
pt. 11	64.2	35.8	0.0	0.0
pt. 12	65.1	34.9	0.0	0.0
pt. 13	64.0	36.0	0.0	0.0
pt. 14	64.7	35.3	0.0	0.0
pt. 15	64.5	35.5	0.0	0.0

Fig. 4.7 (a) The SEM back-scattered electron images and EDX composition analysis of the corroded Ag_2Al compound after 50-hours HAST. (b) The SEM image of an enlarged corrosion region. Red dots marked by 1-12 indicate the EDX analysis location. The resulting element compositions are listed in the table. (c) The EDX energy spectrum of the representative composition analysis points

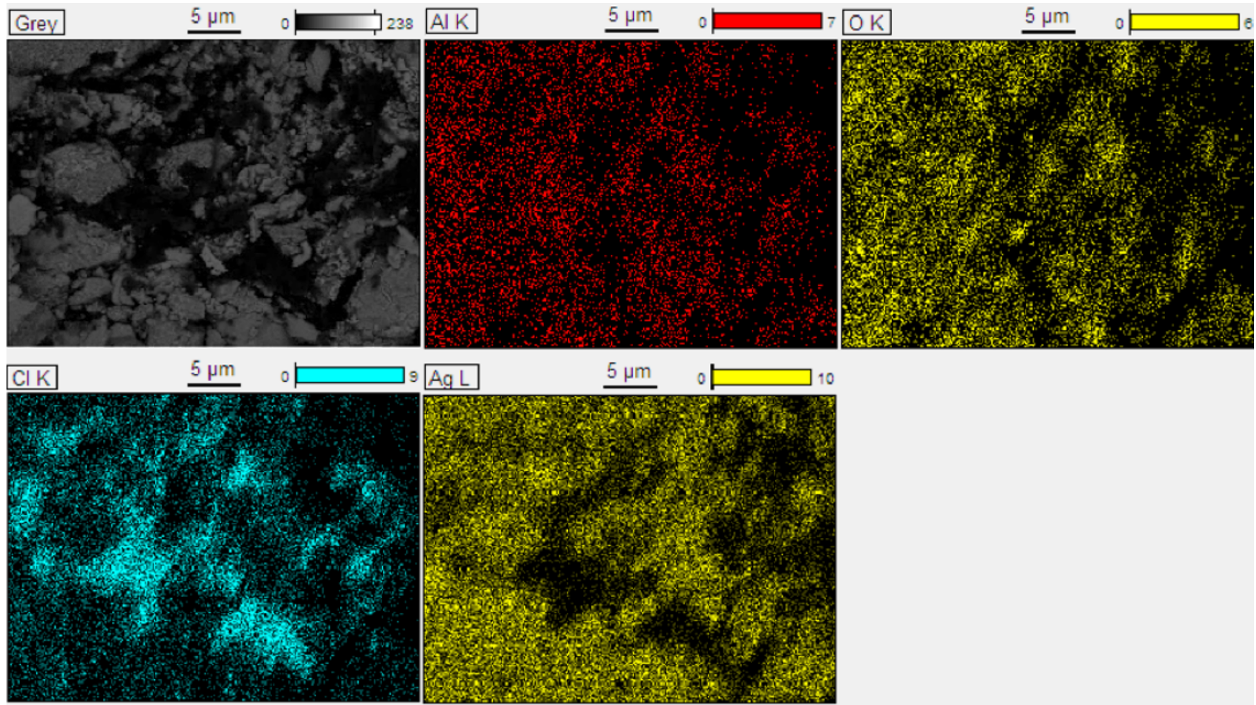

Fig. 4.8 SEM images and EDX elemental mappings of Ag, Al, O, and Cl elements on the corrosion region of Ag_2Al

Fig. 4.9 depicts the corrosion layer thickness on Ag_3Al and Ag_2Al disks, respectively, molded in EMC after HAST for different times. For both Ag_3Al and Ag_2Al, linear regression analysis was used to confirm the linear relationship between the thickness of the corroded layer and the reaction time. The standard deviation and the calculated fitting curve are shown in the graph. The adjusted R-squared values for both linear models are above 0.98 (0.99 for Ag_3Al and 0.98 for Ag_2Al), suggesting a good fit with the experimental data. The thickness versus time curves clearly indicates that Ag_3Al experiences significantly higher

corrosion rate compared to Ag_2Al. The linear growth curve implies that the corrosion rate is not diffusion-limited, but rather is reaction rate-limited. The curves can be described by

$$\mathbf{x = kt}$$

where **x** is the corrosion thickness, **k** is the corrosion rate constant, and **t** is the reaction time. It is seen that the corrosion rate on Ag_3Al is approximately twice the rate on Ag_2Al. This means that Ag_2Al is more resistant to corrosion than Ag_3Al by a factor of 2. Thus, Ag_3Al compound is the weak region in Ag-Al joints due to its high corrosion rate. The corrosion test method reported in this paper can potentially become a test standard for devices molded in EMC that go through various reliability tests.

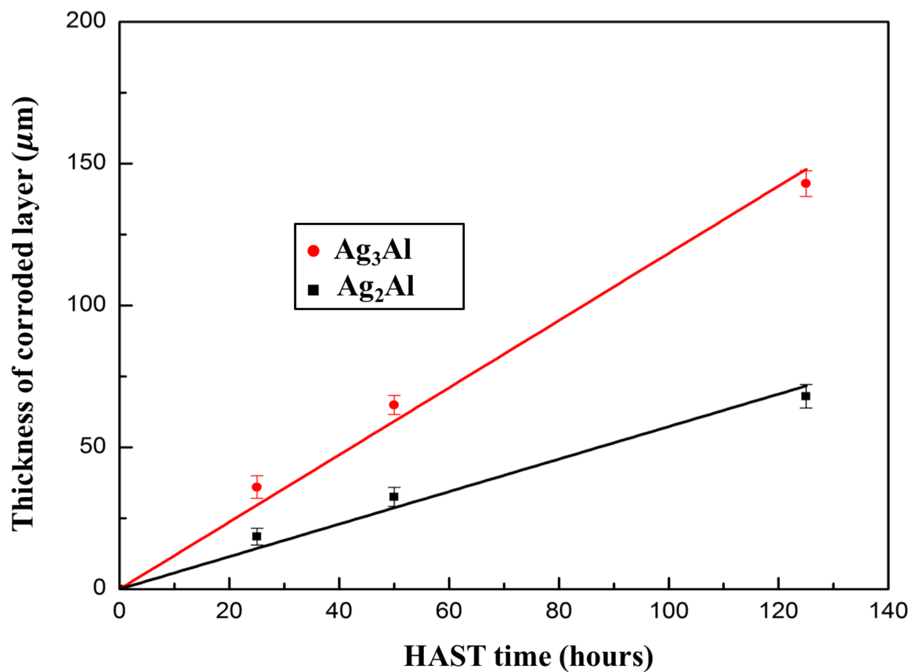

Fig. 4.9 Corrosion layer thickness versus HAST time on bulk Ag_3Al and Ag_2Al disks molded in epoxy molding compound containing chlorine ions.

4.3.3 Proposed Corrosion Model of Ag-Al IMC in EMC under HAST

According to the results shown above, after HAST, corrosion occurs on both Ag_3Al and Ag_2Al but not on Ag and Al. The relatively Cl-rich region detected around the voids and cracks in the corroded Ag_2Al could indicate the formation of aluminum chloride as the intermediate product. After corrosion reaction, Ag_3Al and Ag_2Al compounds disintegrate into the corrosion region consisting of aluminum oxide and dispersed Ag precipitates. Based on the microstructural characterization, a corrosion model is proposed as a sequence of reactions below. The corrosion model is also schematically illustrated in Fig. 4.10.

$$\text{R-Cl (hydrolyzable chloride)} + H_2O \rightarrow \text{R-OH} + H^+ + Cl^- \qquad (1)$$

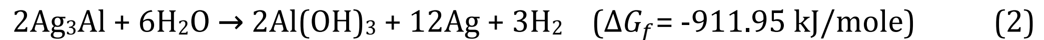

$$2Ag_3Al + 6H_2O \rightarrow 2Al(OH)_3 + 12Ag + 3H_2 \quad (\Delta G_f = -911.95\ \text{kJ/mole}) \qquad (2)$$

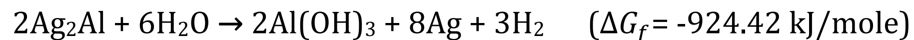

$$2Ag_2Al + 6H_2O \rightarrow 2Al(OH)_3 + 8Ag + 3H_2 \quad (\Delta G_f = -924.42\ \text{kJ/mole})$$

$$Al(OH)_3 + 3Cl^- \rightarrow AlCl_3 + 3OH^- \qquad (3)$$

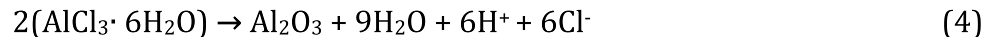

$$2(AlCl_3 \cdot 6H_2O) \rightarrow Al_2O_3 + 9H_2O + 6H^+ + 6Cl^- \qquad (4)$$

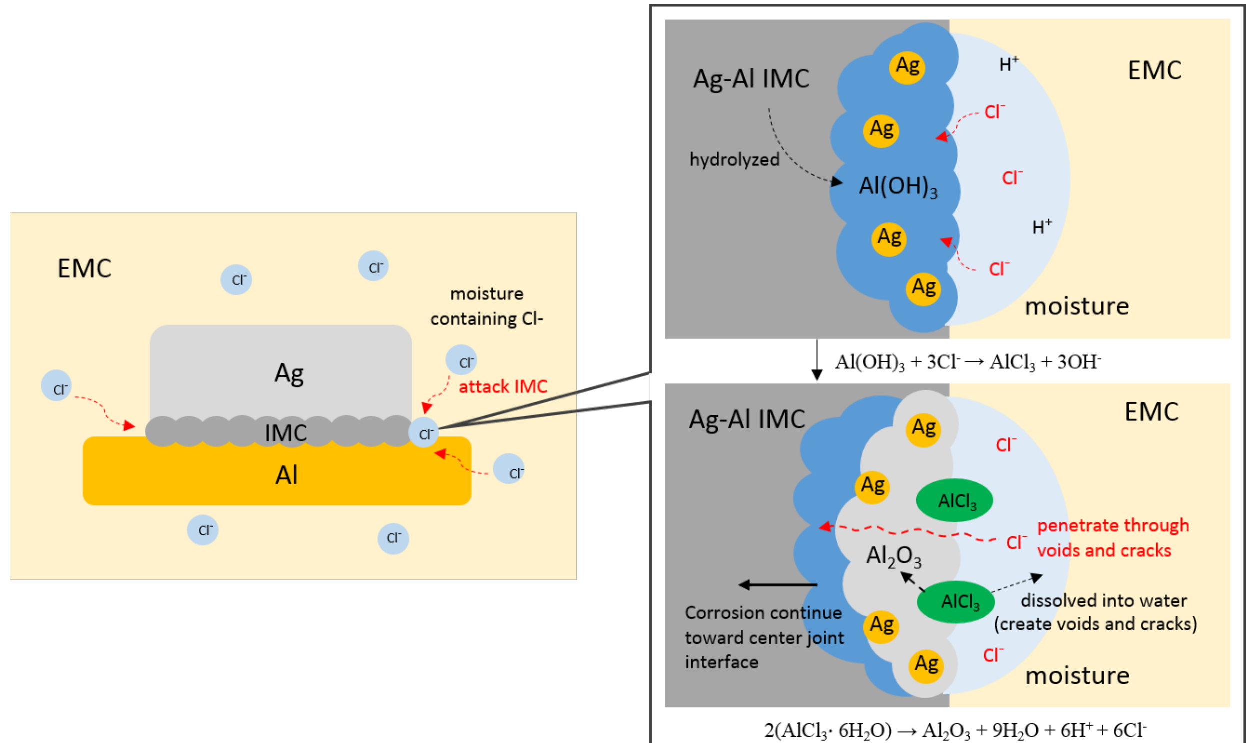

Fig. 4.10 Schematic illustration of proposed corrosion model of the Ag-Al IMC in chlorine-containing EMC under HAST.

The Ag-Al IMC corrosion occurs specifically in the presence of moisture and chlorine ion. Reaction (1) describes the production of chlorine ions in the EMC. Under HAST, moisture can penetrate through the EMC and react with hydrolyzable chloride to release Cl^- ions and hydrogen ion (H^+) [24]. Moisture and Cl^- ions can diffuse to the Ag/Al joint interface and initiate the IMC corrosion. In moisture environment, Ag_3Al and Ag_2Al IMC can be hydrolyzed and transformed into aluminum hydroxide ($Al(OH)_3$), as given in reaction (2). This reaction also forms H_2 gas as a by-product. The out-gassing of H_2 gas can lead to micro-crack

formation in the corrosion region. As the moisture and Cl^- ion diffuse to the IMC region, $Al(OH)_3$ can easily react with Cl^- ions and produce aluminum chloride ($AlCl_3$) [26,27], as shown in reaction (3). As aluminum chloride is chemically unstable, it can be readily hydrolyzed by moisture or transformed into aluminum oxide. In the temperature range of 100 to 200 °C, $AlCl_3$ hydrolyzes into $AlCl_3 \cdot 6H_2O$ octahedral complex and decomposes into aluminum oxide (Al_2O_3) [29], as shown in reaction (4). The hydrolyzation of $AlCl_3$ can lead to micro-void and micro-crack formation in the corrosion region.

In the corrosion mechanism of IMC, the level of moisture and Cl^- ions in the EMC is a dominant factor. As moisture and Cl^- ions diffuse through the EMC and initiate the IMC corrosion, aluminum chloride can form as an intermediate product and can be immediately hydrolyzed into aluminum oxide. This hydrolyzation reaction also releases additional Cl^- ions into the moisture environment, which can accelerate the repetitive reduction and oxidation reactions, from reactions (2) to (4). The formation of voids, cracks, and oxides in the corrosion region will weaken the Ag-Al joint and increase its electrical resistance. Thus, restricting the concentrations of moisture and Cl^- ions in the EMC is extremely important in keeping the quality of Ag-Al joints. Formulation of EMC with low chlorine level and low moisture permeability is a solution. Since corrosion occurs only in IMC region, reducing Ag-Al IMC growth is another possible solution. For Ag-Al wire bonds, adding some elements to

Ag wires might suppress the IMC growth. Recently, Au and Pd elements have been added to produce Ag alloy wires. It is still not clear if these elements suppress the IMC growth.

In conclusion, the corrosion reactions of Ag-Al joints in EMC under HAST were investigated in this study. Results show that the corrosion mainly occurs in the IMC region. In the real Ag-Al wire bonding application, bonding parameters could affect the grain size of Ag-Al IMC and the morphology of Ag/Al bonding interface, which could potentially influence the IMC corrosion rate. By establishing the corrosion experiment with bulk Ag-Al intermetallic compounds, this research quantifies the intrinsic reactivity of Ag_2Al and Ag_3Al with moisture and Cl- and provides possible directions for securing the Ag-Al bonding reliability. Further study on the corrosion behavior of Ag-Al wire bonding will be conducted in our future research.

4.4 Summary

In this study, the reactions of Ag-Al joints and bulk Ag-Al intermetallic compounds with chlorine-containing EMC under HAST were studied. The results show that corrosion induced by moisture and Cl^- ions occurs on both Ag_3Al and Ag_2Al. No corrosion is detected on Ag or Al samples. The corrosion rates of Ag_3Al and Ag_2Al were measured, respectively, by

a quantitative test method. The rates are linear versus time, indicating that the corrosion is reaction-controlled rather than diffusion-controlled. Corrosion rate on Ag_3Al is twice of that on Ag_2Al. Microstructures, phases, and compositions of corroded regions in Ag_3Al and Ag_2Al were examined in details. Bulk Ag_3Al and Ag_2Al compounds were broken down by moisture and Cl^- ions and disintegrated into corrosion regions consisting of aluminum oxide pieces and dispersed Ag precipitates with voids and cracks. A corrosion model was proposed to establish the chemical reactions of Ag_3Al and Ag_2Al with moisture and Cl^- ions in EMC. It is clear that moisture and Cl^- ions are the key ingredients that cause the corrosion. Accordingly, to counter the corrosion, the moisture diffusion through the package and/or the Cl^- ion concentration in EMC must be controlled and reduced. This is the direction discovered in this research to reduce Ag-Al wire-bond corrosion.

4.5 References

1. C. Harper, Electronic packaging and interconnection handbook, McGraw-Hill, Inc., 2004.
2. E. R. R. Tummala and E. J. Rymaszewski, Microelectronics Packaging Handbook, 1997.
3. G. G. Harman, Wire bonding in microelectronics, McGraw-Hill, 2010.
4. J. Cho, H. Jeong, J. Moon, S. Yoo, J. Seo, S. Lee, S. Ha, E. Her, S. Kang and K. Oh, "Thermal reliability & IMC behavior of low cost alternative Au-Ag-Pd wire bonds to Al

metallization," in Electronic Components and Technology Conference (ECTC), 2009 IEEE 59th, pp. 1569-1573, 2009.

5. C. L. Gan and U. Hashim, "Evolutions of bonding wires used in semiconductor electronics: Perspective over 25 years," J. Mater. Sci.: Mater. Electron., vol. 26, no. 7, pp. 4412-4424, 2015.
6. Z. Zhong, "Overview of wire bonding using copper wire or insulated wire," Microelectronics Reliability, vol. 51, no. 1, pp. 4-12, 2011.
7. B. K. Appelt, A. Tseng, C. Chen and Y. Lai, "Fine pitch copper wire bonding in high volume production," Microelectronics Reliability, vol. 51, no. 1, pp. 13-20, 2011.
8. C. Yu, C. Chan, L. Chan and K. Hsieh, "Cu wire bond microstructure analysis and failure mechanism," Microelectronics reliability, vol. 51, no. 1, pp. 119-124, 2011.
9. R. Guo, T. Hang, D. Mao, M. Li, K. Qian, Z. Lv and H. Chiu, "Behavior of intermetallics formation and evolution in Ag–8Au–3Pd alloy wire bonds," J. Alloys Compounds, vol. 588, pp. 622-627, 2014.
10. T. Chuang, C. Tsai, H. Wang, C. Chang, C. Chuang, J. Lee and H. Tsai, "Effects of annealing twins on the grain growth and mechanical properties of Ag-8Au-3Pd bonding wires," J Electron Mater, vol. 41, no. 11, pp. 3215-3222, 2012.
11. C. Cheng, H. Hsiao, S. Chu, Y. Shieh, C. Sun and C. Peng, "Low cost silver alloy wire bonding

with excellent reliability performance," in Electronic Components and Technology Conference (ECTC), 2013 IEEE 63rd, pp. 1569-1573, 2013.

12. H. Kim, J. Y. Lee, K. Paik, K. Koh, J. Won, S. Choe, J. Lee, J. Moon and Y. Park, "Effects of Cu/Al intermetallic compound (IMC) on copper wire and aluminum pad bondability," IEEE Transactions on Components and Packaging Technologies, vol. 26, no. 2, pp. 367-374, 2003.
13. Y. C. Jang, S. Y. Park, H. D. Kim, Y. C. Ko, K. W. Koo, M. R. Choi, H. G. Kim, N. K. Cho, I.T. Kang and J.H. Yee, "Study of intermetallic compound growth and failure mechanisms in long term reliability of silver bonding wire," in Electronics Packaging Technology Conference (EPTC), 2014 IEEE 16th, pp. 704-708, 2014.
14. J. Tsai, A. Lan, D. Jiang, L. W. Wu, J. Huang and J. Hong, "Ag alloy wire characteristic and benefits," in Electronic Components and Technology Conference (ECTC), 2014 IEEE 64th, pp. 1533-1538, 2014.
15. L. J. Kai, L. Y. Hung, L. W. Wu, M. Y. Chiang, D. S. Jiang, C. Huang and Y. P. Wang, "Silver alloy wire bonding," in Electronic Components and Technology Conference (ECTC), 2012 IEEE 62nd, pp. 1163-1168, 2012.
16. J. Xi, N. Mendoza, K. Chen, T. Yang, E. Reyes, S. Bezuk, J. Lin, S. Ke and E. Chen, "Evaluation of Ag wire reliability on fine pitch wire bonding," in Electronic Components and

Technology Conference (ECTC), 2015 IEEE 65th, pp. 1392-1395, 2015.

17. A. McAlister, "The Ag-Al (silver-aluminum) system," Bulletin of Alloy Phase Diagrams, vol. 8, no. 6, pp. 526-533, 1987.

18. S. Lim, P. Rossiter and J. Tibballs, "Assessment of the Al-Ag binary phase diagram," Calphad, vol. 19, no. 2, pp. 131-141, 1995.

19. Y. Chiu, T. Chiang, P. Yang, L. Huang, C. Hung, S. Uegaki and K. Lin, "The corrosion behavior of Ag alloy wire bond on Al pad in molding compounds of various chlorine contents under biased-HAST," in Electronics Packaging (ICEP), 2016 International Conference, pp. 497-501, 2016

20. M. Lue, C. Huang, S. Huang and K. Hsieh, "Bromine-and chlorine-induced degradation of gold-aluminum bonds," J Electron Mater, vol. 33, no. 10, pp. 1111-1117, 2004.

21. C. L. Gan, C. Francis, B. L. Chan and U. Hashim, "Extended reliability of gold and copper ball bonds in microelectronic packaging," Gold Bulletin, vol. 46, no. 2, pp. 103-115, 2013.

22. P. Su, H. Seki, C. Ping, S. Zenbutsu, S. Itoh, L. Huang, N. Liao, B. Liu, C. Chen and W. Tai, "An evaluation of effects of molding compound properties on reliability of Cu wire components," in Electronic Components and Technology Conference (ECTC), 2011 IEEE 61st, pp. 363-369, 2011.

23. T. Uno, "Bond reliability under humid environment for coated copper wire and bare

copper wire," Microelectronics Reliability, vol. 51, no. 1, pp. 148-156, 2011.

24. C. May, Epoxy resins: chemistry and technology, CRC press, 1987.

25. H. B. Fan, E. K. Chan, C. K. Wong and M. M. Yuen, "Investigation of moisture diffusion in electronic packages by molecular dynamics simulation," J. Adhes. Sci. Technol., vol. 20, no. 16, pp. 1937-1947, 2006.

26. S. K. Prasad, Advanced wire bond interconnection technology, Springer Science & Business Media, 2004.

27. B. D. Craig, Fundamental aspects of corrosion films in corrosion science, Springer Science & Business Media, 2013.

28. M. Choi, H. Kim, T. Lee, Y. Jeon, Y. Ahn, K. Koo, Y. Jang, S. Park, J. Yee and N. Cho, "Microstructural evaluation and failure analysis of Ag wire bonded to Al pads," Microelectronics Reliability, vol. 55, no. 11, pp. 2306-2315, 2015.

29. H. K. Farag and F. Endres, "Studies on the synthesis of nano-alumina in air and water stable ionic liquids," Journal of Materials Chemistry, vol. 18, no. 4, pp. 442-449, 2008.

Chapter Five

Direct silver to aluminum solid-state bonding processes

5.1 Introduction

In recent years, high temperature electronic packaging has been rapidly developed due to increasing demand of power electronics applications, particularly for the automotive, aerospace, and energy production industries [1-3]. The introduction of silicon carbide and gallium nitride semiconductors has enabled power electronics to operate at high temperatures above 350 °C [4]. For continuous operations under extreme high temperatures, novel interconnection materials and packaging structures are required for power electronics systems [5,6].

Direct bond copper (DBC) substrates have been widely used in power electronics for many years [7,8]. DBC substrates have advantages of high current carrying capacity, relatively high thermal conductivity, and controlled coefficient of thermal expansion (CTE) [9]. Recently, reliability issues of DBC substrates in thermal cycling tests have been reported [10-12]. The thermal cycling stress induces cracks at the copper/ceramic interface, leading to the eventual delamination of DBC substrates [10,11]. As a possible alternative, direct bond aluminum (DBA) substrates have been developed [13-14]. DBA substrates outperform DBC

substrates in thermal cycling tests [14-15]. The reason is the lower yield stress and plastic strain rate of aluminum as opposed to copper, which result in lower thermomechanical stress at the aluminum/ceramic interface and less strain hardening during thermal cycling. No crack or delamination was observed in DBA substrates after 1500 thermal cycles from -55 °C to 250 °C [15].

A main challenge of using aluminum layers or substrates in electronic packaging is its poor bondability. The native aluminum oxide layer prevents aluminum from electroless or electrolytic plating of metallization layer, which is an essential step to make aluminum bondable to die-attach materials such as solders and nano-silver paste [16]. Thus, the zincating process is required to prepare DBA substrates for further metallization processing. During the zincating process, the aluminum oxide is dissolved in the zincating solution, and a layer of zinc is deposited to protect the surface, providing a basis for subsequent metallization [17]. The zincating process exhibits a narrow process window due to its high reaction sensitivity to aluminum surface conditions [18,19]. The zincating and following metallization processes on aluminum largely increase the processing cost and add more reliability issues [20].

In this research, Ag-Al solid-state bonding has been developed as a novel bonding technique to directly bond Ag to Al substrates. SEM and TEM analyses were utilized to study

the microstructures and fracture mechanisms. In the solid-state bonding process at 425 and 450 °C, Ag and Al atoms inter-diffused through the thin aluminum oxide layer to react and form Ag_2Al and Ag_3Al. The shear strength of the Ag-Al joints passes the military criterion with a large margin. As shown in Fig. 5.1, an application of this new technique is to bond Ag foils to Al substrates and make them bondable to solders and nano-silver paste. This foil bonding technique provides an alternative to the zincating and metallization processes on aluminum substrates. At a more advanced level, device chips can be bonded to Al substrates using Ag foils as the bonding medium at 300 °C.

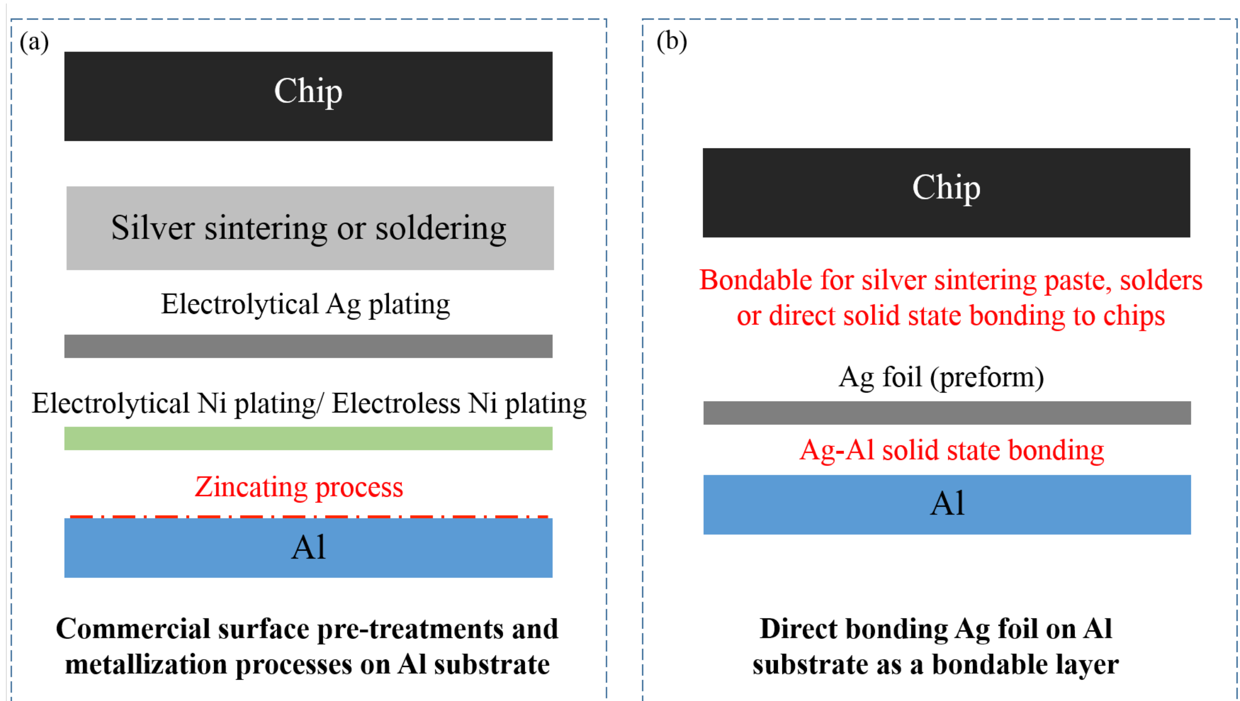

Fig. 5.1 (a) Commercial surface pre-treatments and metallization processes on Al substrate in electronic packaging. (b) Proposed Ag-Al solid-state bonding technique to direct bond Al foil on Al substrate as a bondable layer which is compatible with nano-silver paste and

solders. In a more advanced level, device chips can be bonded to the Ag foil on Al substrates at 300 °C using solid-state bonding technique.

5.2 Experimental Design and Procedures

To achieve Ag-Al solid-state bonding, Ag disks (10 mm in diameter and 1 mm in thickness) and Al substrates (15 mm × 12 mm × 1 mm) with 99.9% purity are employed. Ag disks were grown through the ingot casting method followed by annealing [21,22]. Ag shots with 99.99% purity were loaded into 150 mm long quartz tubes with 10 mm in inner diameter. After loading, the tubes were evacuated by a vacuum pump and sealed by a hydrogen torch to form capsules. The capsules were brought to and kept at 1000 °C for 2 h, followed by 48-h annealing at 850 °C to ensure complete homogenization. After annealing, the ingots (50 mm long and 10 mm in diameter) were cut into disks with a thickness of 1.5 mm. Ag disks and Al substrates were ground with silicon carbide-coated papers up to 2000 grits and polished with 1 μm diamond powder suspended fluid to achieve clean surfaces for bonding. During the bonding process, the Ag disk is placed over the Al substrate and held by a fixture with 1,000 psi (6.89 MPa) static pressure to ensure intimate contact. The assembly is loaded on a graphite platform in a vacuum furnace and heated with temperature monitored by a miniature thermocouple. The solid-state bonding is performed

at a vacuum level of 0.1 Torr (13.33 Pa) to suppress oxidation. The bonding temperatures are selected as 400 °C, 425 °C, and 450 °C, respectively, with a bonding time of 10 minutes.

The microstructures and phase compositions of the resulting Ag-Al joints are examined using scanning electron microscopy/energy dispersive X-ray spectroscopy (SEM/EDX, FEI Philips XL-30, FEG SEM) in back-scattered electron (BSE) mode. The standard single-strap-joint configuration [23, 24] was used to evaluate the shear strength of the Ag-Al joints. The shear test was conducted at room temperature using a tensile testing machine (Model 8800, Instron Corporation) with a crosshead speed of 1 mm/minute. After the shear test, the fracture surfaces of the joints are evaluated. The phase compositions of the fracture surface are probed by SEM/EDX and X-ray diffraction (XRD). The area ratios of the fractured phases are analyzed using ImageJ software. To further investigate the phase distribution at the Ag/Al interface and the failure mechanism of the Ag-Al joint, transmission electron microscopy (TEM) analysis is conducted with a model JEOL-2100F equipped for scanning TEM (STEM) [25]. The TEM specimens are prepared with an in-situ method of dual-beam focused ion beam (FIB) on Tescan GAIA3 SEM/FIB.

5.3 Experimental Results and Discussion

5.3.1 Ag-Al Solid-State Bonding Process

In this experiment, Ag disks, produced in house, were bonded to Al substrates using solid-state bonding technique without any flux or interlayer. Fig. 5.2 shows cross-section back-scattered electron images of Ag-Al joints bonded at 400 °C, 425 °C, and 450 °C, respectively, for 10 minutes. For the Ag-Al joint bonded at 400 °C, Fig. 5.2 (a), no intermetallic compound (IMC) formation was observed. During solid-state bonding, Ag and Al conformed to each other through elastic deformation to achieve intimate contact on the interface. On the bonding interface, no cracks or voids were observed. As the bonding temperature was raised above 425 °C, Ag-Al IMC formed at the bonding interface, as exhibited in Fig. 5.2 (b) and (c). With 425 °C bonding temperature, the microstructure reveals island-like IMC. With 450 °C bonding temperature, a continuous IMC layer was produced. These results indicate that the IMC morphology and growth are strongly dependent on the bonding temperature. In solid-state bonding process, higher bonding temperature accelerates interdiffusion of Ag and Al and thus enhances IMC growth. The SEM images at higher magnification show the IMC grew into both Al and Ag regions away from the bonding interface. A thin black line was

observed. This line was later identified as the aluminum oxide (Al_2O_3) layer on the Al substrate before bonding. Thus, this line can act as a marker of the original Ag-Al contact interface. EDX analysis was performed on the enlarged SEM image, Fig. 2(c), where red dots marked 1 - 5 indicate locations at which the resulting compositions are listed in Table 5.1. Based on the EDX data, the IMC growing into the Al region is identified as Ag_2Al. The IMC phases growing into the Ag region were characterized as Ag_2Al and Ag_3Al, where the Ag_3Al layer is very thin and between the Ag_2Al and Ag regions. As indicated in Table 5.1, the compositions of Ag_2Al on locations 3 and 4 are approximately 34.5 at. % Al while the thin Ag_3Al layer contains 22.1 at. % Al. The Ag-Al phase diagram is presented in Fig. 5.3 to show the composition ranges of the Ag_2Al and Ag_3Al intermetallic phases [26].

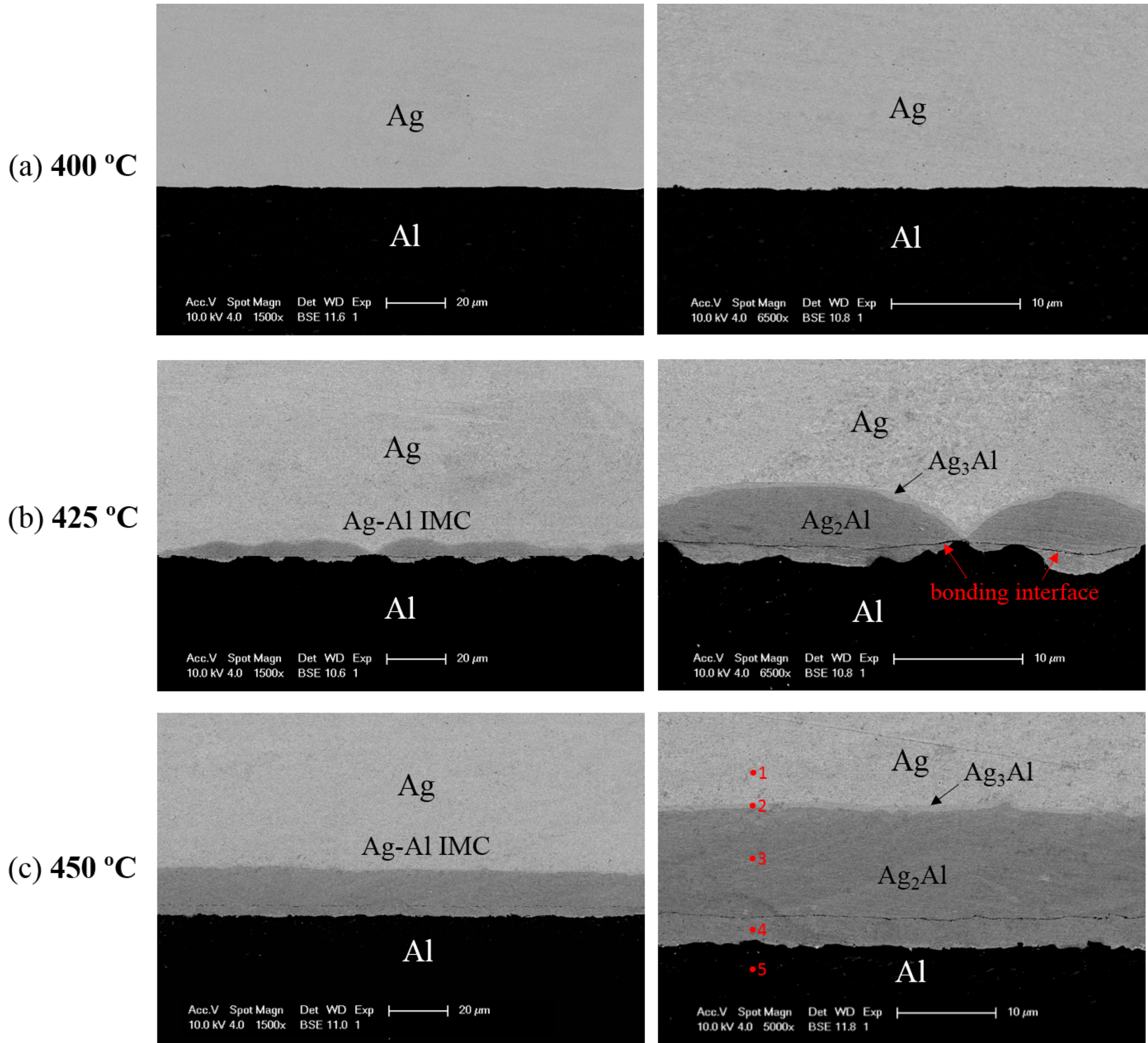

Fig. 5.2 SEM back-scattered electron images of Ag-Al joints bonded at (a) 400 °C, (b) 425 °C, and (c) 450 °C for 10 minutes. In the enlarged image of (c), the red dots marked by 1-5 indicate the EDX analysis locations and the resulting element compositions are listed in the Table 5.1.

Table 5.1 EDX data on locations 1 - 5 near Ag-Al interface in Fig. 2 (c).

Locations	Ag (at. %)	Al (at. %)	Phases
1	98.7	1.3	(Ag)
2	77.9	22.1	Ag_3Al
3	65.7	34.3	Ag_2Al
4	65.5	34.5	Ag_2Al
5	0.8	99.2	(Al)

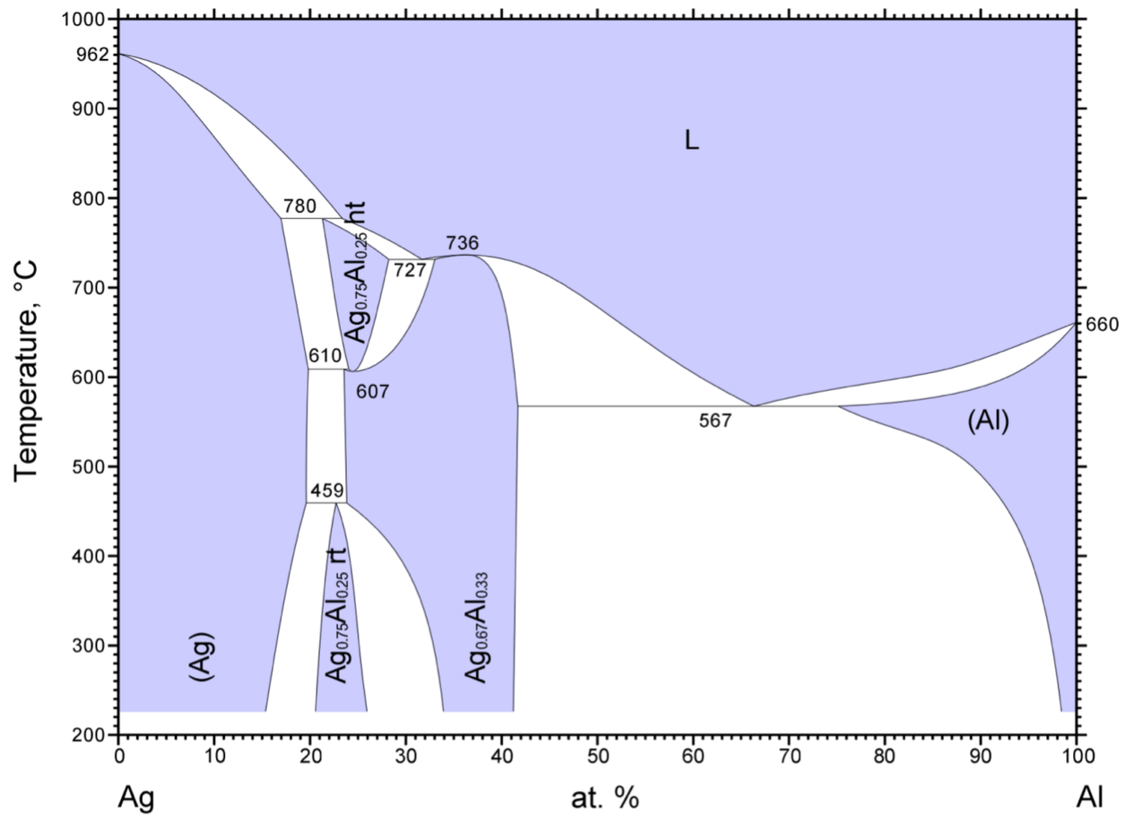

Fig. 5.3 Ag-Al binary phase diagram [26].

5.3.2 Shear Test Results of Ag-Al Solid-State Bonding

The shear strength of the Ag-Al joints was evaluated by standard single-strap-joint shear test [23]. The specimens were tested at room temperature using a tensile testing machine with a crosshead speed of 1 mm/minute. The single-lap-joint and single-strap-joint specimen configurations are illustrated in Fig 5.4 (a). In the typical single-lap-joint shear test, the shear strength and fracture behavior could be influenced by the non-uniform stress distribution along the bonded region [27]. In this study, to minimize the normal stress created by the bending moment on the shear test sample [28], the single-strap-joint was chosen as the shear test configuration. Fig. 5.4 (b) shows the shear strength of the joints bonded at temperatures of 400 °C, 425 °C, and 450 °C, respectively. Test results show that the Ag-Al joints bonded at 450 °C exhibit the highest shear strength of 28.0 MPa. For samples bonded at 425 °C and 400 °C, shear strength values of 19.7 MPa and 5.4 MPa, respectively, were obtained. The standard deviations of the joint shear strength of each bonding condition are also shown in Fig. 5.4 (b). These joint strength values pass the military criterion (MIL-STD-883H method 2019.8) by a large margin [29].

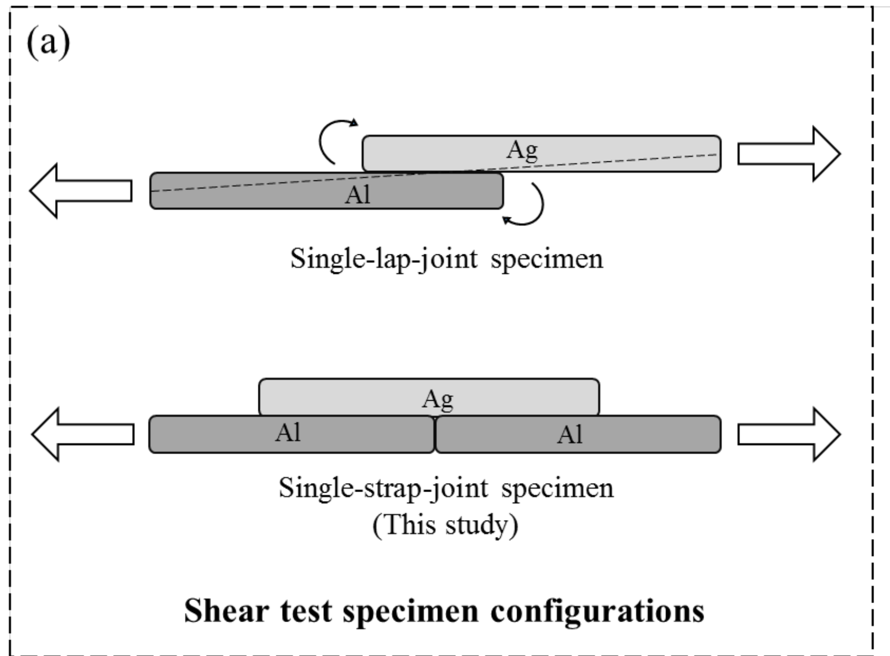

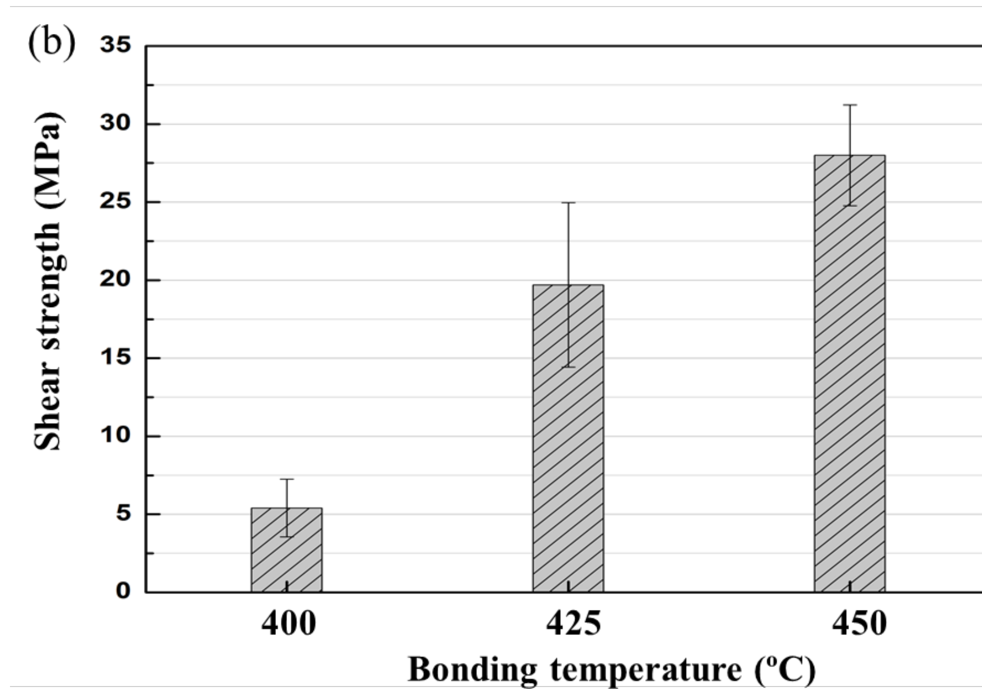

Fig. 5.4 (a) The schematic diagram of the shear test specimen configurations: single-lap-joint and single-strap-joint (used in this study). (b) The shear strength of the Ag-Al joints bonded at 400 °C, 425 °C, and 450 °C, respectively.

To understand the fracture behavior of the Ag-Al joints, the fracture surfaces after the shear test were studied. The phase compositions were probed by SEM/EDX and XRD. The area ratios of fracture phases were analyzed using ImageJ software. Fig. 5.5 shows the SEM micrographs of the fracture surfaces on the Al side of the Ag-Al joints. In the sample bonded at 400 °C, the fracture surface clearly shows 94% Al and only 6% Ag_2Al. No Ag traces are observed on the Al regions, indicating weak bonding interface between the Ag disk and Al substrate. For the sample bonded at 425 °C, the microstructure exhibits a mixture of Ag_2Al and Al. The Ag_2Al regions significantly increased up to 71% of the total fracture area. For the sample bonded at 450 °C, the fracture surface is 100% Ag_2Al, indicating that the breakage incurs within the continuous Ag_2Al layer.

The XRD spectrum on the fracture surface of the Al side of the Ag-Al joints bonded at 450 °C is presented in Fig. 5.5 (d). The XRD pattern reveals the presence of Ag_2Al and Al. Since Ag_2Al layer thickness is much smaller than the X-ray penetration depth, the strong Al peaks were caused by the Al substrate beneath the Ag_2Al layer. The shear strength of the Ag-Al joints and the phase distribution on the fracture surfaces are summarized in Table 5.2. Experimental results show that the shear strength of Ag-Al solid-state bonding are related to the area of intermetallic compound formation. With little IMC formation, the samples bonded at 400 °C exhibits relatively weak bonding and the joint fracture along the Ag/Al

interface. A thin Al_2O_3 layer exists at the Ag/Al interface, as will be shown in next paragraph. This Al_2O_3 layer prevents Ag atoms to get into intimate contact with Al atoms. For the samples bonded at higher temperatures of 425°C and 450°C, Ag and Al atoms are able to inter-diffuse through the thin Al_2O_3 layer to react and form Ag_2Al regions. With a continuous Ag_2Al layer through the joint interface, the sample bonded at 450 °C exhibits the highest shear strength.

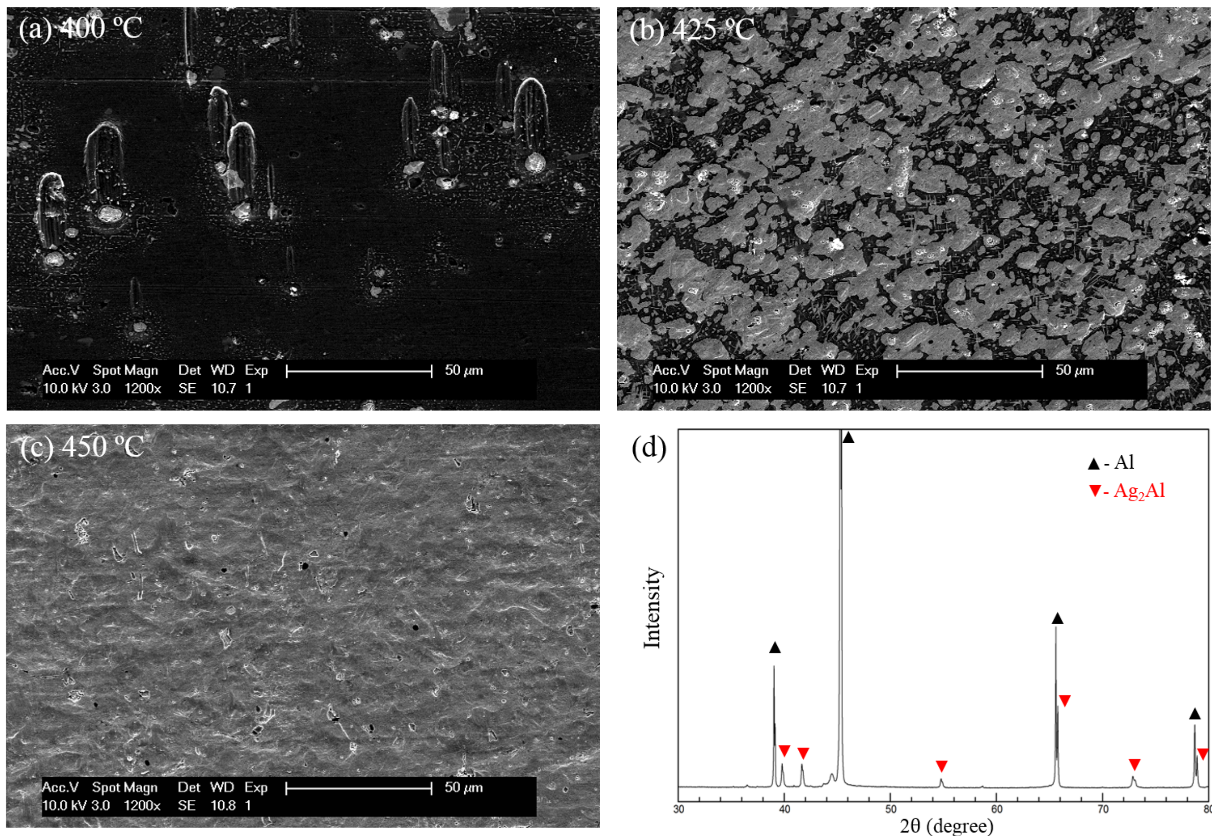

Fig. 5.5 SEM back-scattered images of the fracture surfaces on the Al side of the Ag-Al joints bonded at (a) 400 °C, (b) 425 °C, and (c) 450 °C. The XRD spectrum of the fracture surface on the Al side of the Ag-Al joints bonded at 450 °C is presented in (d).

Table 5.2 The shear strength and the fracture surface composition of Ag-Al joints bonded at 400 °C, 425 °C, and 450 °C, respectively.

Bonding temperature	Shear strength	Composition on fracture surface
400 °C	5.4 MPa	94% Al and 6% Ag_2Al
425 °C	19.7 MPa	29% Al and 71% Ag_2Al
450 °C	28.0 MPa	100% Ag_2Al

To further investigate exactly where the joint bonded at 450 °C fractured within the Ag_2Al region, the Ag side and Al side of the sample after shear test were molded with epoxy, cut in cross sections and polished for characterization. Fig. 5.6 shows the back-scattered electron images of the fractured Ag-Al joints. It is clearly observed that the fracture occurred along the black line shown in Fig. 5.2 (c), and a thin Ag_2Al layer, which was originally beneath the black line, was left on the Al substrate. Also, isolated micro-cracks within the thin Ag_3Al layer were observed, shown in Fig. 5.6 (c) and (d). The micro-cracks were confined within the Ag_3Al layer and did not propagate into Ag_2Al or Ag region. No cracks were seen within the Ag_2Al, indicating that Ag_2Al is relatively ductile compared to Ag_3Al. In this study, no surface pretreatment was applied on the Al substrates to remove the native oxide layer before the solid-state bonding process. It is probable that the thin black line is attributed to the native Al_2O_3 on Al substrates prior to bonding. In the solid-state bonding process at elevated temperatures, Ag and Al atoms inter-diffused through the thin

Al_2O_3 layer to react and form Ag_2Al layer. As seen in Fig. 5.2 (b), the initial Ag_2Al growth was non-uniform along the bonding interface. Initial growth began on the bonding interface regions where Ag atoms and Al_2O_3 molecules had atomic contact. The thin Al_2O_3 layer had nowhere to go and thus was embedded within the resulting the Al_2Al layer. In the following section, nano-structures were studied in details using TEM and STEM with electron diffraction technique to confirm that the black line is indeed composed of Al_2O_3 within Ag_2Al region.

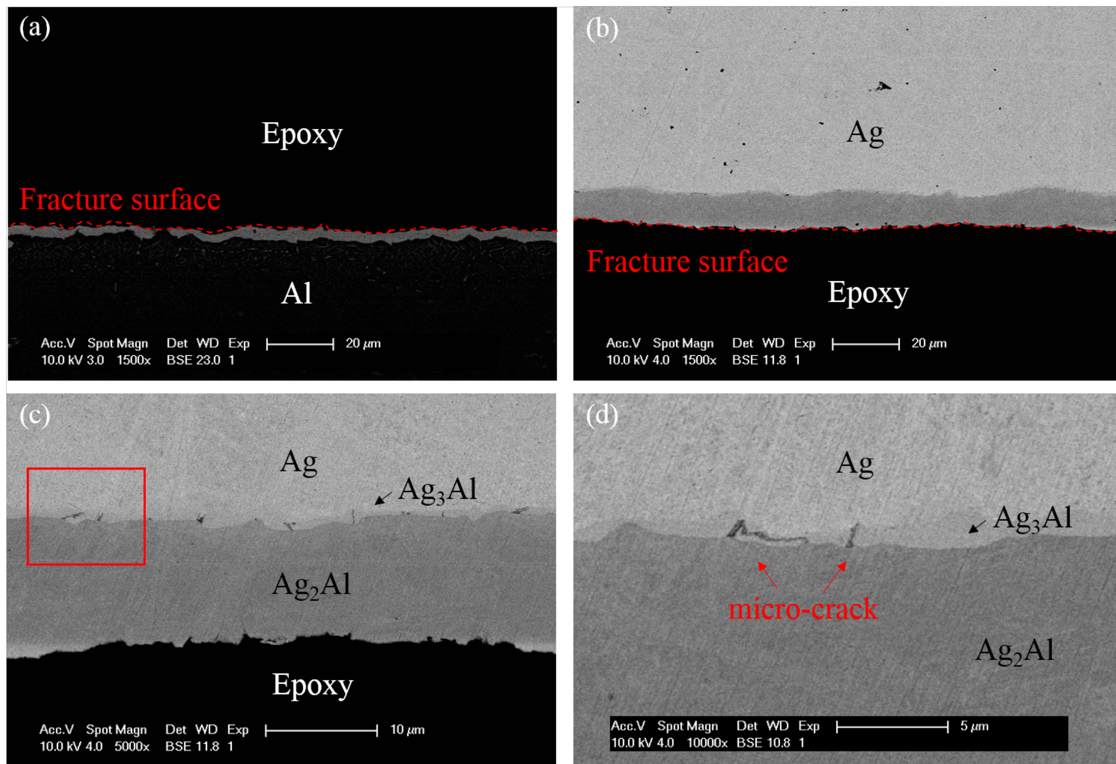

Fig. 5.6 SEM back-scattered images on the cross-sections of Ag-Al joint bonded at 450 °C after shear test (a) Al side and (b) Ag side. Enlarged SEM images on the Ag side are presented in (c) and (d).

5.3.3 TEM analysis on Ag-Al Solid-State Bonding

Figs. 5.7 and 5.8 show the TEM images on the bonding interface cross section of a Ag-Al joint bonded at 450 °C. The TEM specimens were prepared using in-situ dual focused ion beams in an SEM (Tescan GAIA3). The ion-milled region is denoted by the red rectangle on the SEM image, Fig. 5.7 (a). The scanning TEM images reveal Ag_2Al/Al_2O_3 $/Ag_2Al/Al$ structure. The Al_2O_3 layer is clearly observed in Fig. 5.7 (b), pointed out by red arrows. Fig. 8 displays high resolution STEM images of the Ag_2Al/Al interface region and a Ag_2Al region with embedded Al_2O_3 layer. Report shows that the transition temperature of amorphous Al_2O_3 to transform into γ-Al_2O_3 is about 550 °C [30]. In this research, the amorphous Al_2O_3 grew extremely slowly and remained stable during the solid-state bonding process at 450 °C. As shown in Fig. 5.8 (b), the Al_2O_3 layer is 5 nm in thickness, continuous, and well connected to enclosing Ag_2Al at atomic level without any nano-voids or nano-cracks. The selected area diffraction patterns (SADP) of encircled zones in Fig. 5.8 are displayed in the inserts. The SADP patterns confirm the selected area to be Ag_2Al with hexagonal crystal structure, space group: $P6_3/mmc$, and a = b = 2.887 Å, c = 4.624 Å, as characterized along $[11\bar{2}1]$ zone axis. Furthermore, it is worth pointing out that no silver oxide (Ag_2O) was

observed at the Ag-Al bonding interface, since Ag_2O is thermodynamically unstable at high temperature (> 220°C) and tends to decompose in vacuum at 118 - 220 °C [31,32].

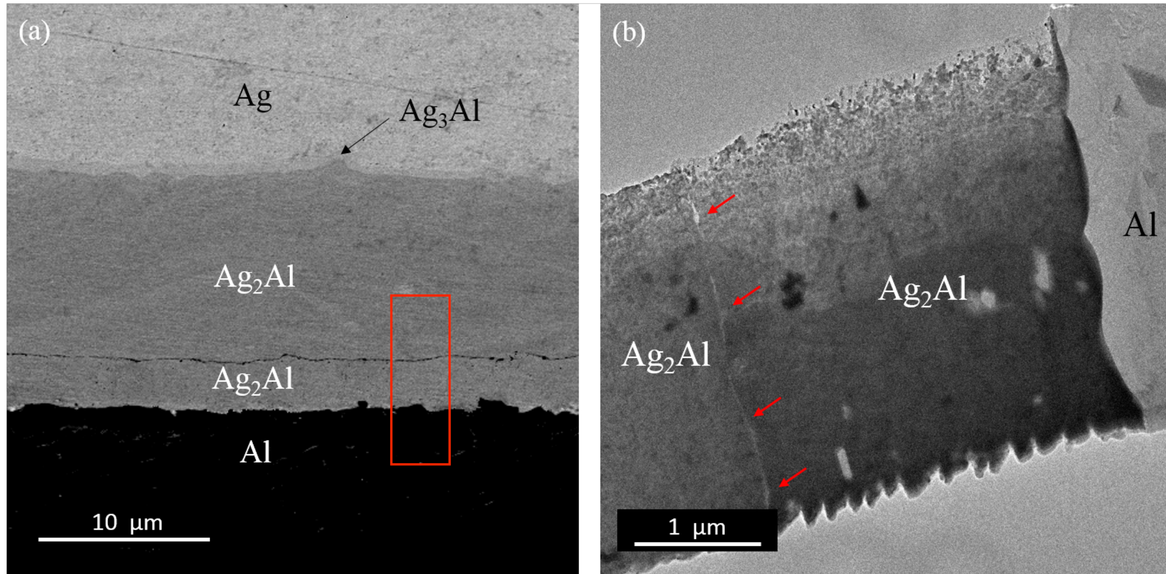

Fig. 5.7 (a) The SEM cross section image showing the interface region of a Ag-Al joint bonded at 450 °C. (b) The TEM image of the rectangle box in (a), where aluminum oxide line is indicated by red arrows. The TEM specimen was prepared by in-situ dual focused ion beams (FIB).

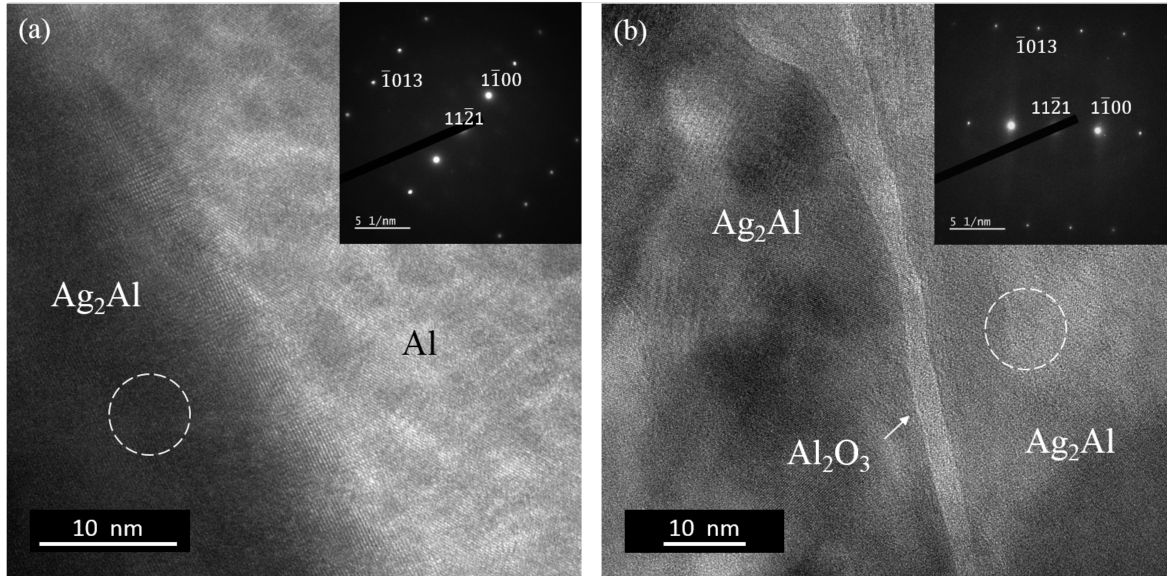

Fig. 5.8 High resolution STEM images of (a) the Ag_2Al/Al interface region and (b) a Ag_2Al region containing a thin Al_2O_3 layer. The inserts display selected area diffraction patterns (SADP) of the encircled Ag_2Al zones characterized along $[11\bar{2}1]$ zone axis

5.4 Summary

In this research, Ag-Al solid-state bonding was achieved at 400, 425, and 450 °C, respectively, to bond Ag directly to Al substrates. This bonding was deemed not possible in the past because of the native oxide on the Al substrate. Our experimental results, however, show that this bonding is achievable so far as the Ag and Al atoms on the interface can interdiffuse through the thin Al_2O_3 layer. No surface treatment was applied on Al substrates to remove the native Al_2O_3 layer before the bonding. Microstructures of the resulting Ag-Al joints were evaluated by SEM and TEM. For the samples bonded at 425 and 450 °C, the

results clearly show that Ag and Al atoms indeed inter-diffused through the thin Al_2O_3 layer to react and form Ag_2Al and Ag_3Al compounds. Using STEM imaging, 5 nm thick Al_2O_3 layer was observed within the Ag_2Al region. It seems that the embedded Al_2O_3 layer was well connected to Ag_2Al region at atomic level. The shear strength of the Ag-Al joints passes the military criterion, MIL-STD-883H method 2019.8, by a large margin. Fracture analyses show that fracture occurred within the Ag_2Al region and extended along the bonding interface. This new Ag-Al bonding process is valuable in opening up more and new Al application as platforms or substrates by bonding a thin Ag layer at selected areas to make them bondable or solder-able.

5.5 References

1. C. Buttay, D. Planson, B. Allard, D. Bergogne, P. Bevilacqua, C. Joubert, M. Lazar, C. Martin, H. Morel and D. Tournier, "State of the art of high temperature power electronics," *Materials Science and Engineering: B*, vol. 176, no. 4, pp. 283-288, 2011.
2. P. Hagler, P. Henson and R. W. Johnson, "Packaging technology for electronic applications in harsh high-temperature environments," *IEEE Trans.Ind.Electron.*, vol. 58, no. 7, pp. 2673-2682, 2011.

3. A. Lostetter, F. Barlow and A. Elshabini, "An overview to integrated power module design for high power electronics packaging," *Microelectronics reliability*, vol. 40, no. 3, pp. 365-379, 2000.

4. P. G. Neudeck, R. S. Okojie and L. Chen, "High-temperature electronics-a role for wide bandgap semiconductors?" *Proc IEEE*, vol. 90, no. 6, pp. 1065-1076, 2002.

5. L. Coppola, D. Huff, F. Wang, R. Burgos and D. Boroyevich, "Survey on high-temperature packaging materials for SiC-based power electronics modules," in *Power Electronics Specialists Conference, 2007. PESC 2007. IEEE*, pp. 2234-2240, 2007.

6. M. R. Werner and W. R. Fahrner, "Review on materials, microsensors, systems and devices for high-temperature and harsh-environment applications," *IEEE Trans.Ind.Electron.*, vol. 48, no. 2, pp. 249-257, 2001.

7. H. He, R. Fu, D. Wang, X. Song and M. Jing, "A new method for preparation of direct bonding copper substrate on Al_2O_3," *Mater Lett*, vol. 61, no. 19, pp. 4131-4133, 2007.

8. B. Mouawad, B. Thollin, C. Buttay, L. Dupont, V. Bley, D. Fabregue, M. Soueidan, B. Schlegel, J. Pezard and J. Crebier, "Direct copper bonding for power interconnects: Design, manufacturing, and test," *IEEE transactions on Components, Packaging and Manufacturing Technology*, vol. 5, no. 1, pp. 143-150, 2015.

9. J. Schulz-Harder, "Advantages and new development of direct bonded copper substrates," *Microelectronics Reliability*, vol. 43, no. 3, pp. 359-365, 2003.
10. Y. Yoshino, H. Ohtsu and T. Shibata, "Thermally induced failure of Copper-Bonded alumina substrates for electronic packaging," *J Am Ceram Soc*, vol. 75, no. 12, pp. 3353-3357, 1992.
11. G. Dong, X. Chen, X. Zhang, K. D. Ngo and G. Lu "Thermal fatigue behaviour of Al_2O_3-DBC substrates under high temperature cyclic loading," *Soldering & Surface Mount Technology*, vol. 22, no. 2, pp. 43-48, 2010.
12. D. Camilleri, "Thermo-mechanical behaviour of DBC substrate assemblies subject to soldering fabrication processes," *Soldering & Surface Mount Technology*, vol. 24, no. 2, pp. 100-111, 2012.
13. S. Kraft, A. Schletz and M. Maerz, "Reliability of silver sintering on DBC and DBA substrates for power electronic applications," in *Integrated Power Electronics Systems (CIPS), 2012 7th International Conference on*, pp. 1-6, 2012.
14. D. C. Katsis and Y. Zheng, "Development of an extreme temperature range silicon carbide power module for aerospace applications," in *Power Electronics Specialists Conference, 2008. PESC 2008. IEEE*, pp. 290-294, 2008.

15. T. G. Lei, J. N. Calata, K. D. Ngo and G. Lu, "Effects of large-temperature cycling range on direct bond aluminum substrate," *IEEE Transactions on Device and Materials Reliability*, vol. 9, no. 4, pp. 563-568, 2009.

16. S. Lee, J. Lee and Y. Kim, "Nucleation and growth of zinc particles on an aluminum substrate in a zincate process," *J Electron Mater*, vol. 36, no. 11, pp. 1442-1447, 2007.

17. M. M. Arshad, I. Ahmad, A. Jalar, G. Omar and U. Hashim, "The effects of multiple zincation process on aluminum bond pad surface for electroless nickel immersion gold deposition," *Journal of electronic packaging*, vol. 128, no. 3, pp. 246-250, 2006.

18. K. Azumi, S. Egoshi, S. Kawashima and Y. Koyama, "Effect of copper pretreatment on the double zincate process of aluminum alloy films," *J.Electrochem.Soc.*, vol. 154, no. 4, pp. D220-D226, 2007.

19. J. Lee, I. Lee, T. Kang, N. Kim and S. Oh, "The effects of bath composition on the morphologies of electroless nickel under-bump metallurgy on Al input/output pad," *J Electron Mater*, vol. 34, no. 1, pp. 12-18, 2005.

20. S. Robertson and I. Ritchie, "The role of iron (III) and tartrate in the zincate immersion process for plating aluminium," *J.Appl.Electrochem.*, vol. 27, no. 7, pp. 799-804, 1997.

21. S. Fu and C.C. Lee, " A study on intermetallic compound formation in Ag-Al system and evaluation of its mechanical properties by micro-indentation," *J. Mater.Sci.: Mater.Electron.*, vol. 29, no. 5, pp. 3985-3991, 2018.
22. S. Fu and C.C. Lee, "A corrosion study of Ag–Al intermetallic compounds in chlorine-containing epoxy molding compounds," *J. Mater.Sci.: Mater.Electron.*, vol. 28, no. 20, pp. 15739-15747, 2017.
23. S. S. Smeltzer, "Testing of structural joints," *Encyclopedia of Aerospace Engineering*, 2010.
24. L. Tong, J. Spelt and G. Fernlund, "Strength determination of adhesive bonded joints," in: L. Tong and C. Soutis (Eds.), Recent Advances in Structural Joints and Repairs for Composite Materials, Springer, pp. 27-66, 2003.
25. https://www.aphys.kth.se/polopoly_fs/1.190438!/Menu/general/column-content/attachment/TEM_manual_JEOL2100.pdf
26. S. Lim, P. Rossiter and J. Tibballs, "Assessment of the al-ag binary phase diagram," *Calphad*, vol. 19, no. 2, pp. 131-141, 1995.
27. D. Oplinger, "Effects of adherend deflections in single lap joints," *Int.J.Solids Structures*, vol. 31, no. 18, pp. 2565-2587, 1994.
28. L. Hart-Smith, "Designing to minimize peel stresses in adhesive-bonded joints," Delamination and debonding of materials, ASTM International, 1985.

29. Department of Defense, U.S.A., Test Method Standard Microcircuits, 2010, MIL-STD-883H method 2019.8.

30. M. A. Trunov, M. Schoenitz, and E. L. Dreizin, " Effect of polymorphic phase transformations in alumina layer on ignition of aluminium particles," *Combustion Theory and Modelling*, vol 10, no. 4, pp. 603-623, 2006.

31. W. Garner and L. Reeves, "The thermal decomposition of silver oxide." *Transactions of the Faraday Society*, vol. 50, pp. 254-260, 1954.

32. B. V. L'vov, "Kinetics and mechanism of thermal decomposition of silver oxide." *Thermochimica acta*, vol. 333, no. 1, pp. 13-19, 1999.

Chapter Six

Direct bonding silver to aluminum using eutectic reaction in air

6.1 Introduction

Microelectronics packaging provides electrical connection, physical protection, mechanical support, and thermal cooling for semiconductor integrated circuit [1]. In recent years, there has been an increasing demand for small size, light weight, and high power electronics on wide varieties of automotive, aerospace, military, and other industrial systems [2,3]. In addition, the introduction of wide-bandgap semiconductor, such as SiC and GaN, has enabled power electronics to operate at high temperatures above 350 °C [4]. High temperature packaging technology and novel interconnection materials are therefore becoming a necessity to achieve high performance and high reliability in power electronics systems [5-7].

Direct bond copper (DBC) substrates are commonly used in power electronics industry [8]. Although DBC substrates outperform other substrate materials in current carrying capacity, thermal conductivity, and overall coefficient of thermal expansion (CTE), DBC substrates suffer from reliability problem in thermal cycling tests [9-11]. The

temperature cycling generate the thermomechanical stress at the copper/ceramic interface, and eventually create crack and delamination of DBC substrates [11]. In recent years, direct bond aluminum (DBA) substrates have been developed as a replacement for DBC substrates [12]. DBA substrates generate less thermomechanical stress between the metal and the ceramic baseplate due to the lower yield stress and plastic strain rate of aluminum as opposed to copper [13,14]. In addition, the high thermal conductivity, light weight, and low cost of aluminum make DBA substrate a promising substrate material for high power electronic packaging.

However, the biggest obstacle of using aluminum (Al) layers or substrates in electronic packaging is the poor compatibility of aluminum oxide layer formed on aluminum surface [15]. The oxide layer prevents aluminum to form strong bonding to metallization layers and die-attach materials such as solders and nano-silver paste [16,17]. Therefore, the zincating process is an essential surface conditioning step to protect the aluminum surface and provide a basis for subsequent metallization [18]. As shown in Fig. 6.1, electrolytic/electroless plating of nickel (Ni) and electrolytic plating of silver (Ag) are the most commonly applied metallization layers post the zincating process. To make aluminum surface bondable, the zincating and following Ni and Ag plating process largely increase the processing cost and add more reliability issues on aluminum substrates.

In this present study, a new process has been developed to directly bond Ag to Al substrates using eutectic reaction in air. The microstructures and bonding strength of the Ag-Al joints were evaluated. The shear strength of the Ag-Al joints passes the military criterion with a large margin. This bonding technique provides an alternative to the zincating and metallization processes on aluminum substrates, making aluminum surface bondable to solders and nano-silver paste. At a more advanced level, device chips can be bonded to Al substrates using Ag foils as the bonding medium at 300 °C.

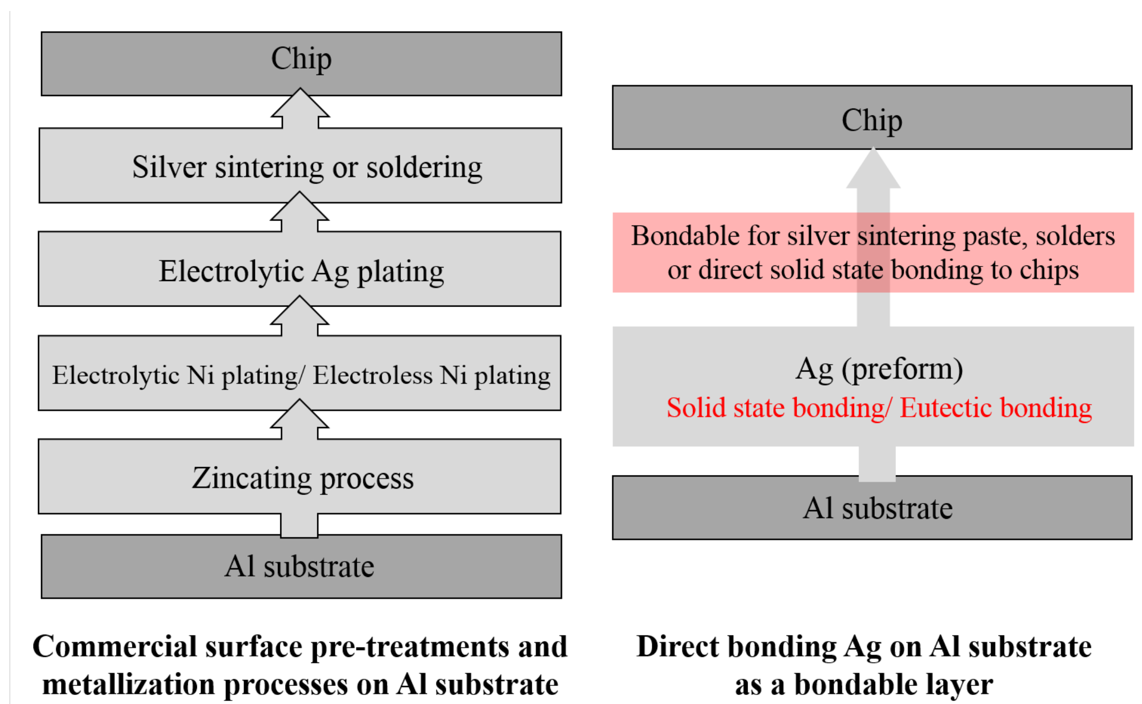

Fig. 6.1 (a) Commercial surface pre-treatments and metallization processes on Al substrate in electronic packaging. (b) Proposed Ag-Al direct bonding technique which is compatible with nano-silver paste and solders.

6.2 Experimental Design and Procedures

To directly bond Ag on Al substrates, Ag disks (10 mm in diameter and 1 mm in thickness) and Al substrates (15 mm × 12 mm × 1 mm) with 99.9% purity are prepared. Ag disks and Al substrates were fine polished with 1 μm diamond powder suspended fluid to achieve clean surfaces with mirror surface finish. In the bonding process, Ag disks and Al substrates are held by a fixture with 1,000 psi (6.89 MPa) static pressure to ensure intimate contact between Ag and Al. The assembly is placed in a pre-heated muffle furnaces and heated with temperature monitored by the thermocouple. The bonding temperatures are selected as 450 °C and 570 °C, with a bonding time of 10 minutes and 5 minutes, respectively.

The microstructures and phase compositions of the resulting Ag-Al joints are examined using scanning electron microscopy/energy dispersive X-ray spectroscopy (SEM/EDX, FEI Philips XL-30). The shear test was conducted at room temperature using a tensile testing machine (Model 8800, Instron Corporation) with a crosshead speed of 1 mm/minute. The standard single-strap-joint configuration was used to evaluate the shear strength of the Ag-Al joints. After the shear test, the fracture surfaces of the joints are evaluated. To further investigate the phase distribution at the Ag/Al interface and the failure

mechanism of the Ag-Al joints, transmission electron microscopy (TEM) analysis is conducted with a model JEOL-2100F equipped for scanning TEM (STEM).

6.3 Experimental Results and Discussion

6.3.1 Ag-Al Eutectic Bonding Process and Comparison with Ag-Al Solid-State Bonding

In this research, Ag disks, produced by conventional casting method, were bonded to Al substrates without using any flux or interlayer. The bonding temperatures 450 °C and 570 °C, respectively, were selected to demonstrate Ag-Al solid state bonding and Ag-Al eutectic bonding in air. Fig. 6.2 shows cross-section back-scattered electron images of Ag-Al joints bonded at 450 °C. During solid state bonding, Ag and Al conformed to each other through elastic deformation to achieve intimate contact on the interface. As the bonding temperature reached 450 °C for 10 minutes, a continuous Ag-Al IMC formed at the bonding interface, as exhibited in Fig. 6.2 (a). No cracks or voids were observed at the bonding interface. In Fig. 6.2 (b) and (c), the SEM images at higher magnification show the IMC grew into both Al and Ag regions away from the bonding interface. A thin black line was observed. This line was later identified as the aluminum oxide (Al_2O_3) layer on the Al substrate before bonding.

Therefore, this line indicates the original Ag-Al contact interface. EDX analysis was conducted on the enlarged SEM images, Fig. 6.2 (b) and (c), where red dots marked 1- 6 indicate the locations of composition analysis. The resulting phase compositions are listed in Table 6.1. The IMC phase growing into the Al region was identified as Ag_2Al. The IMC phases growing into the Ag region were characterized as Ag_2Al and Ag_3Al. As shown in Fig. 6.2 (c), a thin Ag_3Al IMC layer was detected between the Ag_2Al IMC and Ag region.

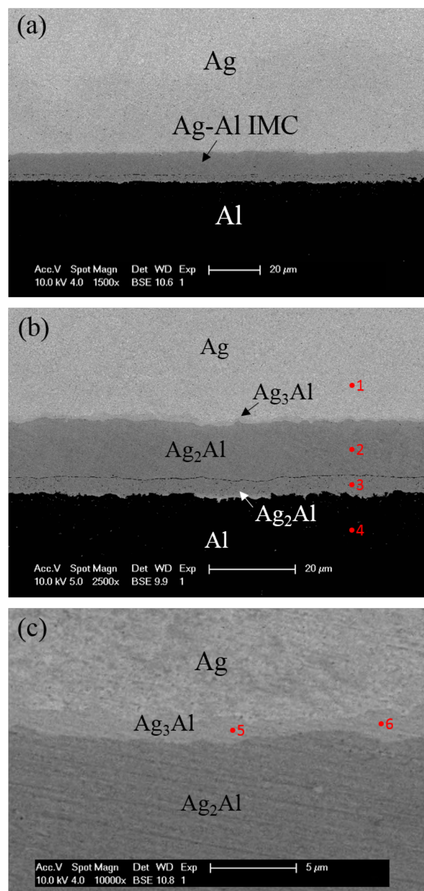

Fig. 6.2 SEM back-scattered electron images of Ag-Al joints bonded at 450 °C for 10 minutes. In the enlarged image of (b) and (c), the red dots marked by 1 - 6 indicate the EDX analysis locations and the resulting element compositions are listed in the Table 6.1.

As indicated in Table 6.1, the compositions of Ag_2Al on locations 2 and 3 are approximately 34.5 at. % Al while the thin Ag_3Al layer contains average 22.0 at. % Al on locations 5 and 6. The Ag-Al phase diagram [19] is presented in Fig. 6.3 to show the composition ranges of the Ag_2Al and Ag_3Al intermetallic phases.

Table 6.1 EDX data on locations 1- 6 near Ag-Al interface in Fig. 6.2.

Locations	Ag (at. %)	Al (at. %)	Phases
1	98.9	1.1	(Ag)
2	65.7	34.3	Ag_2Al
3	65.5	34.5	Ag_2Al
4	0.8	99.2	(Al)
5	78.3	21.7	Ag_3Al
6	77.7	22.3	Ag_3Al

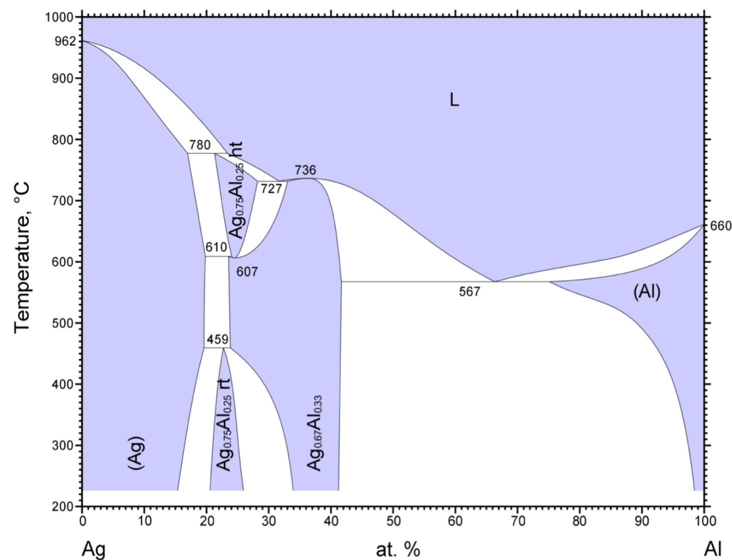

Fig. 6.3 Ag-Al phase diagram [19]

Based on the Ag-Al phase diagram, Ag-Al system has eutectic point between the Ag_2Al and Al-rich solid solution at the temperature of 567 °C. To achieve direct Ag to Al bonding

using eutectic reaction, 570 °C was selected as the bonding temperature. Fig. 7.4 displays the cross-sectional microstructure of the Ag-Al eutectic bonding. As the bonding temperature raised above the Ag-Al eutectic temperature for 5 minutes, a typical eutectic region formed at the bonding interface. The eutectic region was composed of the bright Ag_2Al phase and the dark Al-rich solid solution phase (Al). EDX analysis results show that the oval-shaped Ag_2Al in eutectic region contains approximately 36 - 37.5 at. % Al, and the intergranular Al-rich solid solution contains 9.4 - 14.5 at. % Ag. It is worth mentioning that a continuous Ag_2Al IMC layer formed between the eutectic region and Ag region, but no Ag_3Al IMC formation was detected at the Ag_2Al/Ag interface. No black line (Al_2O_3) was observed within the Ag_2Al layer nor the bonding interface. Also, as shown in Fig. 7.4 (c), a needle-shape Ag_2Al region formed between the eutectic region and the Al base metal. In Fig. 7.4 (b) and (c), the red dots marked 1- 6 indicate the locations of composition analysis. The phase compositions are listed in Table 7.2.

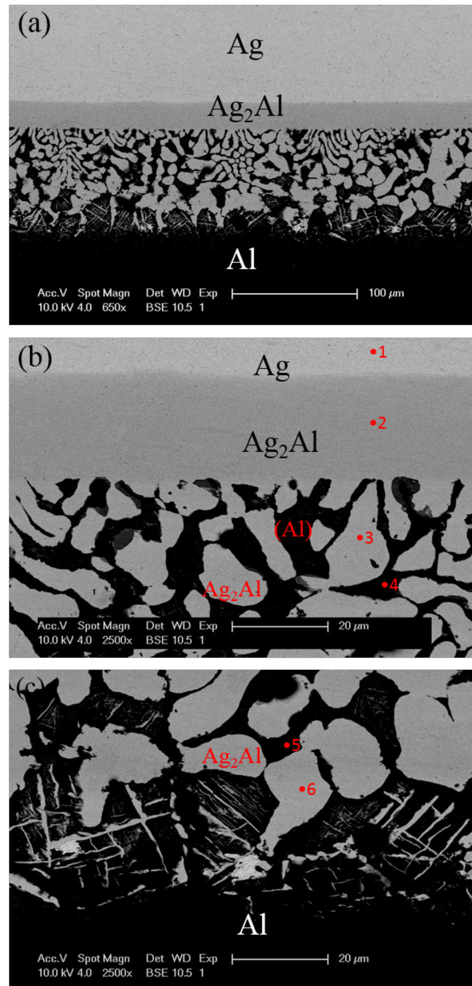

Fig. 6.4 SEM back-scattered electron images of Ag-Al joints bonded at 570 °C for 5 minutes. In the enlarged image of (b) and (c), the red dots marked by 1- 6 indicate the EDX analysis locations and the resulting element compositions are listed in the Table 6.2.

Table 6.2 EDX data on locations 1- 6 near Ag-Al interface in Fig. 6.4.

Locations	**Ag (at. %)**	**Al (at. %)**	**Phases**
1	98.7	1.3	(Ag)
2	65.6	34.4	Ag_2Al
3	63.8	36.2	Ag_2Al
4	14.5	85.5	(Al)
5	9.4	90.6	(Al)
6	62.5	37.5	Ag_2Al

6.3.2 Shear test results of Ag-Al eutectic bonding process

The shear strength of the Ag-Al joints was evaluated by standard single-strap-joint shear test [20]. The specimens were tested at room temperature using a tensile testing machine with a crosshead speed of 1 mm/minute. In this study, instead of using typical single-lap-joint shear test, single-strap-joint was chosen as the shear test configuration to minimize the normal stress created by the bending moment on the shear test sample [21]. The single-strap-joint specimen configuration used in this study is illustrated in Fig. 6.5.

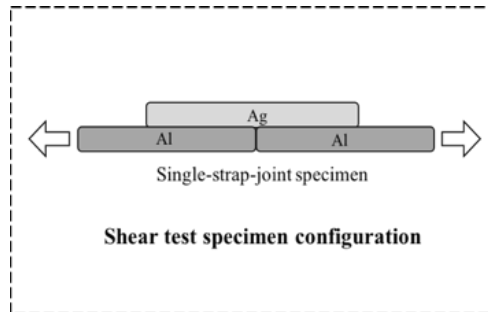

Fig. 6.5 The schematic diagram of the single-strap-joint specimen configuration used in this study for the shear testing.

Table 6.3 Shear strengths of Ag-Al joints using solid-state and eutectic bonding techniques.

Sample #	Solid state bonding (MPa)	Eutectic bonding (MPa)
1	23.7	42.5
2	26.7	> 45 (break at Ag disk)
3	29.1	38.9
4	20.4	> 45 (break at Ag disk)

The shear strength of the Ag-Al joints using solid state bonding and eutectic bonding techniques are summarized in Table III. Test results show that the Ag-Al solid state bondings exhibit shear strength value of 20.4 - 29.1 MPa. For Ag-Al joints bonded at 570 °C using eutectic reaction, sample #1 and #3 broke at the bonding interface with shear strength of 42.5 MPa and 38.9 MPa, respectively. For sample #2 and #4, Ag-Al eutectic bondings broke at Ag disks instead of the bonding interfaces, and the joint shear strength was calculated by the maximum tensile force divided by the Ag-Al bonding area. For both Ag-Al solid state bonding and eutectic bonding, Ag-Al joints strength values pass the military criterion (MIL-STD-883H method 2019.8) by a large margin [22].

To understand the fracture behavior of the Ag-Al joints, the fracture surfaces after the shear test were studied. Fig. 6.6 shows the SEM micrographs of the top-view fracture surfaces on the Al side of the Ag-Al solid state bonding. The microstructure exhibits a flat Ag_2Al surface with no Al substrate exposed, indicating that the breakage incurs within the continuous Ag_2Al layer. To further investigate exactly where the Ag-Al joints fractured within the Ag_2Al region, the Ag side and Al side of the samples after shear test were cut in cross sections for characterization. Fig. 6.6 (b) and (c) show the back-scattered electron images of the fractured Ag-Al solid state bonding. On the fracture surface of the Al side, a thin Ag_2Al layer, which was originally beneath the black line, was left on the Al substrate. It is clearly

observed that the fracture occurred along the black line (Al_2O_3) shown in Fig. 6.2 (b).

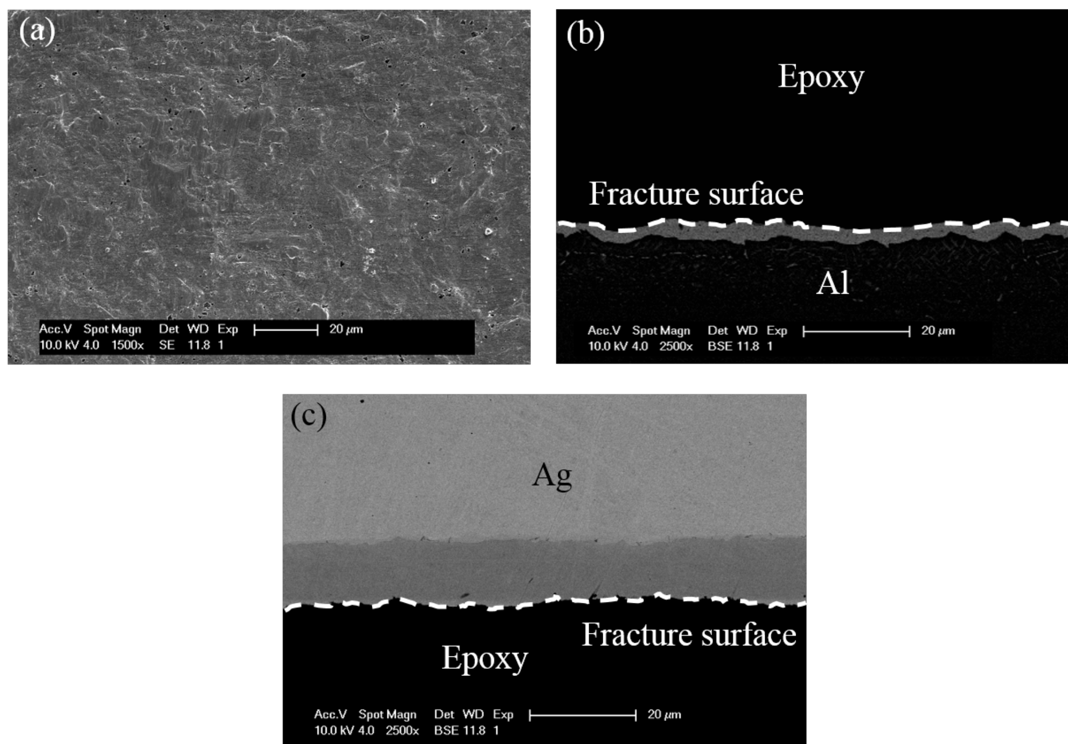

Fig. 6.6 (a) SEM secondary electron image of the fracture surfaces on the Al side of the Ag-Al solid state bonding. SEM back-scattered images of the cross-sections of Ag-Al solid state bonding after shear test on the (b) Al side and (c) Ag side.

Figs. 7 shows the TEM images on the bonding interface cross-section of a Ag-Al solid state bonding. The TEM specimens were prepared using in-situ dual focused ion beams in an SEM. Fig. 7 (a) displays the high resolution STEM image of the $Ag_2Al/Al_2O_3/Ag_2Al$ interface region. The selected area diffraction pattern (SADP) of the Ag_2Al region is shown in Fig. 7 (b). The SADP patterns confirm the selected area to be Ag_2Al characterized along

$[11\bar{2}1]$ zone axis. The embedded Al_2O_3 layer is 5-10 nm in thickness and well connected to enclosing Ag_2Al at atomic level without any nano-cracks. Report shows that the transformation of amorphous Al_2O_3 into γ-Al_2O_3 occurs at 550 °C [23]. In this research, the amorphous Al_2O_3 grew extremely slowly and remained stable during the solid-state bonding process at 450 °C. In shear test, the crack tends to propagate through the continuous Al_2O_3 layer within Ag_2Al region.

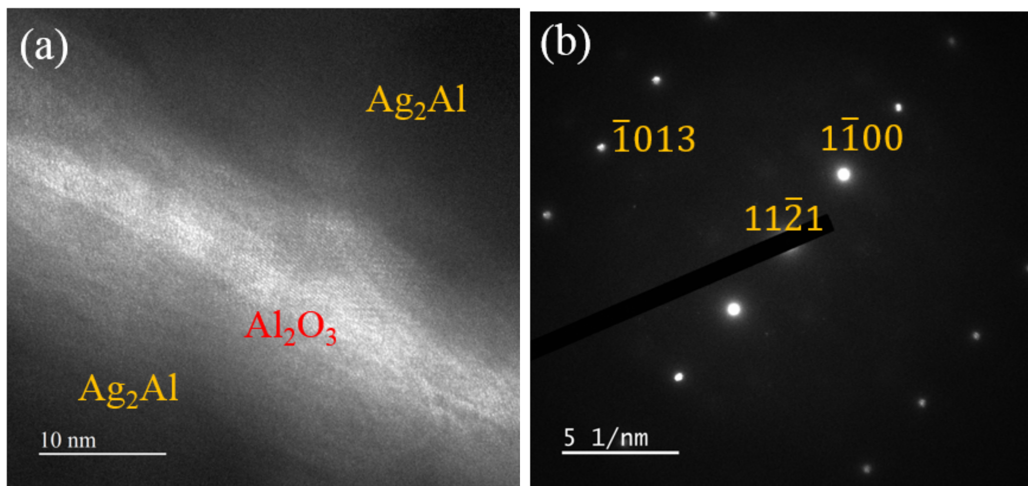

Fig. 6.7 (a) High resolution STEM image of the $Ag_2Al/Al_2O3/Ag_2Al$ interface region. (b)The selected area diffraction pattern (SADP) of the Ag_2Al along $[11\bar{2}1]$ zone axis.

Fig. 6.8 shows the SEM secondary electron images of the top-view fracture surfaces on the Al side of the Ag-Al eutectic bonding. The microstructure shows hybrid-fracture characteristics breaking in the Ag_2Al/(Al) eutectic region, which includes the quasi-cleavage

of Ag_2Al particles and ductile fracture dimples of the Al solid-solution regions. For Ag-Al eutectic bonding, as bonding temperature raised above the eutectic point, the eutectic liquid phase could form at the bonding interface and break the native Al_2O_3 layer on Al substrate. Without the continuous Al_2O_3 layer at the bonding interface as the potentially weak spot, Ag-Al eutectic bonding exhibits higher shear strength and more ductile fracture behavior.

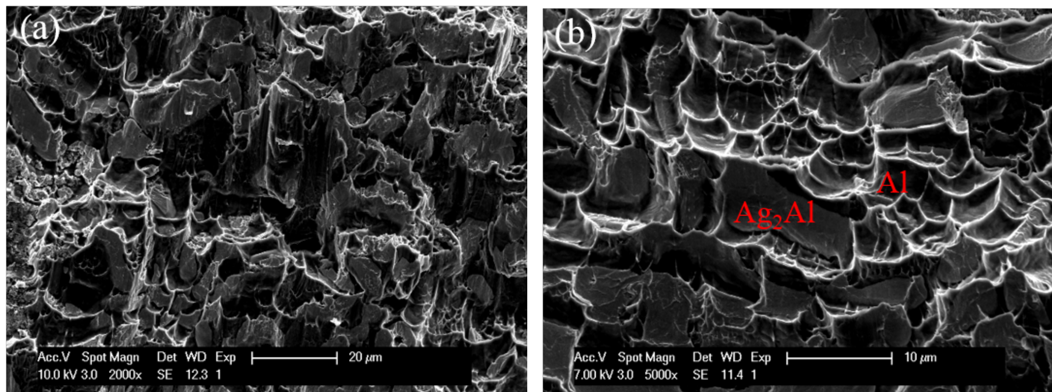

Fig. 6.8 (a) SEM secondary electron image of the fracture surfaces on the Al side of the Ag-Al eutectic bonding.

Furthermore, as compared to Ag-Al solid-state bondings, the joint reliability of Ag-Al eutectic bondings could be enhanced by supressing the formation of Ag_3Al intermetallic phase. In our previous studies on Ag_3Al and Ag_2Al intermetallic compounds, Ag_3Al possesses lower fracture toughness and more brittle nature, and exhibits lower corrosion resistance to moisture and chlorine in the epoxy molding compound [24-26]. Based on Ag-Al diagram,

Ag_3Al phase only stabilizes below 459 °C (μ phase) or within the range of 610 °C to 780 °C (β phase) [19]. In the eutectic bonding process, as the bonding temperature reached 570 °C, the formation of Ag_3Al was supressed or possibly transformed into Ag_2Al phase.

6.4 Summary

In this research, Ag-Al solid state bonding and eutectic bonding process have been developed as novel bonding technique to direct bond Ag to Al substrate. No surface treatment was applied on Al substrates to remove the native Al_2O_3 layer before the bonding. Microstructures of the resulting Ag-Al joints were evaluated by SEM and TEM. The shear strength of the Ag-Al joints passes the military criterion (MIL-STD-883H method 2019.8) by a large margin. Without continuous Al_2O_3 layer at the bonding interface as the potentially weak spot, Ag-Al eutectic bonding exhibits higher shear strength and more ductile fracture behavior. By investigating the fracture surfaces of the Ag-Al joints, the fracture mechanisms of Ag-Al solid state bonding and eutectic bonding were discussed in detail. This new Ag-Al bonding process is valuable in opening up more and new Al application as platforms or substrates by bonding a thin Ag layer at selected areas to make them bondable or solder-able.

6.5 References

1. R. Tummala, E. Rymaszewski, A. Klopfenstein, Microelectronics packaging handbook, Springer Science & Business Media, 2012.
2. A. Lostetter, F. Barlow and A. Elshabini, "An overview to integrated power module design for high power electronics packaging," Microelectronics reliability, vol. 40, no. 3, pp. 365-379, 2000.
3. P. Hagler, P. Henson and R. W. Johnson, "Packaging technology for electronic applications in harsh high-temperature environments," IEEE Trans.Ind.Electron., vol. 58, no. 7, pp. 2673-2682, 2011.
4. P. G. Neudeck, R. S. Okojie and L. Chen, "High-temperature electronics-a role for wide bandgap semiconductors?" Proc IEEE, vol. 90, no. 6, pp. 1065-1076, 2002.
5. M. R. Werner and W. R. Fahrner, "Review on materials, microsensors, systems and devices for high-temperature and harsh-environment applications," IEEE Trans.Ind.Electron., vol. 48, no. 2, pp. 249-257, 2001.
6. L. Coppola, D. Huff, F. Wang, R. Burgos and D. Boroyevich, "Survey on high-temperature packaging materials for SiC-based power electronics modules," in Power Electronics Specialists Conference, 2007. PESC 2007. IEEE, pp. 2234-2240, 2007.

7. J. Cho, R. Sheikhi, S. Mallampati, L. Yin, and D. Shaddock, "Bismuth-Based Transient Liquid Phase (TLP) Bonding as High-Temperature Lead-Free Solder Alternatives," in Electronic Components and Technology Conference (ECTC), 2017 IEEE 67th, pp. 1553-1559, 2017.
8. B. Mouawad, B. Thollin, C. Buttay, L. Dupont, V. Bley, D. Fabregue, M. Soueidan, B. Schlegel, J. Pezard and J. Crebier, "Direct copper bonding for power interconnects: Design, manufacturing, and test," IEEE transactions on Components, Packaging and Manufacturing Technology, vol. 5, no. 1, pp. 143-150, 2015.
9. J. Schulz-Harder, "Advantages and new development of direct bonded copper substrates," Microelectronics Reliability, vol. 43, no. 3, pp. 359-365, 2003.
10. Y. Yoshino, H. Ohtsu and T. Shibata, "Thermally induced failure of Copper-Bonded alumina substrates for electronic packaging," J Am Ceram Soc, vol. 75, no. 12, pp. 3353-3357, 1992.
11. D. Camilleri, "Thermo-mechanical behaviour of DBC substrate assemblies subject to soldering fabrication processes," Soldering & Surface Mount Technology, vol. 24, no. 2, pp. 100-111, 2012.
12. S. Kraft, A. Schletz and M. Maerz, "Reliability of silver sintering on DBC and DBA substrates for power electronic applications," in Integrated Power Electronics Systems (CIPS), 2012 7th International Conference on, pp. 1-6, 2012.

13. D. C. Katsis and Y. Zheng, "Development of an extreme temperature range silicon carbide power module for aerospace applications," in Power Electronics Specialists Conference, 2008. PESC 2008. IEEE, pp. 290-294, 2008.
14. T. G. Lei, J. N. Calata, K. D. Ngo and G. Lu, "Effects of large-temperature cycling range on direct bond aluminum substrate," IEEE Transactions on Device and Materials Reliability, vol. 9, no. 4, pp. 563-568, 2009.
15. S. Lee, J. Lee and Y. Kim, "Nucleation and growth of zinc particles on an aluminum substrate in a zincate process," J Electron Mater, vol. 36, no. 11, pp. 1442-1447, 2007.
16. M. M. Arshad, I. Ahmad, A. Jalar, G. Omar and U. Hashim, "The effects of multiple zincation process on aluminum bond pad surface for electroless nickel immersion gold deposition," Journal of electronic packaging, vol. 128, no. 3, pp. 246-250, 2006.
17. S. Fu, C. Yu, T. Lee, K. Liu and J. Duh, "Impact crack propagation through the dual-phased $(Cu,Ni)_6Sn_5$ layer in Sn–Ag–Cu/Ni solder joints," Mater Lett, vol. 80, pp. 103-105, 2012.
18. J. Lee, I. Lee, T. Kang, N. Kim and S. Oh, "The effects of bath composition on the morphologies of electroless nickel under-bump metallurgy on Al input/output pad," J Electron Mater, vol. 34, no. 1, pp. 12-18, 2005.
19. S. Lim, P. Rossiter and J. Tibballs, "Assessment of the al-ag binary phase diagram," Calphad, vol. 19, no. 2, pp. 131-141, 1995.

20. S. S. Smeltzer, "Testing of structural joints," Encyclopedia of Aerospace Engineering, 2010.

21. L. Hart-Smith, "Designing to minimize peel stresses in adhesive-bonded joints," Delamination and debonding of materials, ASTM International, 1985.

22. Department of Defense, U.S.A., Test Method Standard Microcircuits, 2010, MIL-STD-883H method 2019.8.

23. M. A. Trunov, M. Schoenitz, and E. L. Dreizin, " Effect of polymorphic phase transformations in alumina layer on ignition of aluminium particles," Combustion Theory and Modelling, vol 10, no. 4, pp. 603-623, 2006.

24. S. Fu and C.C. Lee, "Solid-State Reactions of Silver and Aluminum Associated with Silver Wire Bonds," in Electronic Components and Technology Conference (ECTC), 2016 IEEE 66th, pp. 648-653, 2016.

25. S. Fu and C.C. Lee, " A study on intermetallic compound formation in Ag-Al system and evaluation of its mechanical properties by micro-indentation," J. Mater.Sci.: Mater.Electron., vol. 29, no. 5, pp. 3985-3991, 2018.

26. S. Fu and C.C. Lee, "A corrosion study of Ag–Al intermetallic compounds in chlorine-containing epoxy molding compounds," J. Mater.Sci.: Mater.Electron., vol. 28, no. 20, pp. 15739-15747, 2017.

Chapter Seven

New solid-state die-attach method using silver foil bonded on aluminum substrate by eutectic reaction

7.1 Introduction

In power electronics, silicon carbide (SiC) and gallium nitride (GaN), both wide bandgap semiconductors, have emerged as promising alternatives to replace silicon (Si) in the high-power and high-temperature segments [1,2]. Compared to silicon devices, wide bandgap semiconductor devices exhibit lower switching losses, higher breakdown voltages, and higher operating temperatures (above 350 °C) [3-5]. To assure power module reliability in high-temperature applications such as automotive and aerospace vehicles, the electronic packages must withstand severe thermal environments [6,7]. At operating temperatures above 250 °C, reliability becomes a serious challenge in die-attachment and metalized substrates of the modules [8-13]. The operating temperatures of commonly used Sn-Ag-Cu and Sn-Pb solders are limited to 180 °C [8]. For high operation temperature, sintered nano-silver paste has been employed as a die-attach method for power devices [9,10]. Nevertheless, the oxidation issue at the interfaces due to connected pores in the porous silver (Ag) joint structure remains a challenge for this technique [11,12]. In addition,

substrate reliability is another issue in power electronic packages under thermal cycling conditions [13]. Reliability issues of direct bond copper (DBC) substrates have been reported [15,16]. With large temperature excursion higher than 250 °C, severe thermomechanical stresses induce cracks at the copper/ceramic interface, leading to eventual delamination of the DBC structure [14-16].

As a possible alternative, direct bond aluminum (DBA) substrates outperform DBC substrates in thermal cycling tests [17]. DBA substrates generate less thermomechanical stresses at the aluminum/ceramic interface due to the lower yield strength and plastic strain rate of aluminum as opposed to copper. No crack or delamination was observed in DBA substrates after 1500 thermal cycles from -55 °C to 250 °C [18]. The difficulty of using Al electrodes or substrates in electronic packaging is poor bondability. A zincating process and further metallization are required to make DBA substrates compatible with die-attach materials such as solders and nano-silver paste [19]. During the zincating process, the native aluminum oxide (Al_2O_3) is dissolved in the zincating solution and a layer of zinc is deposited to protect the surface, providing a basis for subsequent nickel/silver (Ni/Ag) plating [20]. However, the zincating process exhibits a narrow process window due to its high reaction sensitivity to aluminum surface conditions [21, 22]. The zincating and following

metallization processes on aluminum could largely increase the manufacturing cost and add more reliability issues [23].

In this research, a novel Ag foil bonding technique has been developed to directly bond Ag to Al substrates by Ag-Al eutectic reaction in air. Using the Ag foil as a solid-state bonding medium, Si chips are bonded to the Ag foil on Al substrates at 300 °C without additional die-attach material. In the Ag-Al eutectic bonding process, a eutectic structure consisting of Ag_2Al and Al-rich solid solution form at the bonding interface. Strong bonding is achieved between Ag and Al as the native Al_2O_3 layer originally on Al is broken into pieces and dispersed into the eutectic structure. Shear test results show that the Si/Ag/Al joints pass the military standard with a high shear strength of 39.8 MPa. As illustrated in Fig. 1, this foil bonding technique provides an alternative to the zincating and metallization processes on aluminum-based substrates. Meanwhile, the highly conductive Ag foil can be used as the perfect die-attach medium for high-temperature electronic packaging applications. In this study, bonding design and procedures are first described. Experimental results are reported and discussed. A short summary is then given.

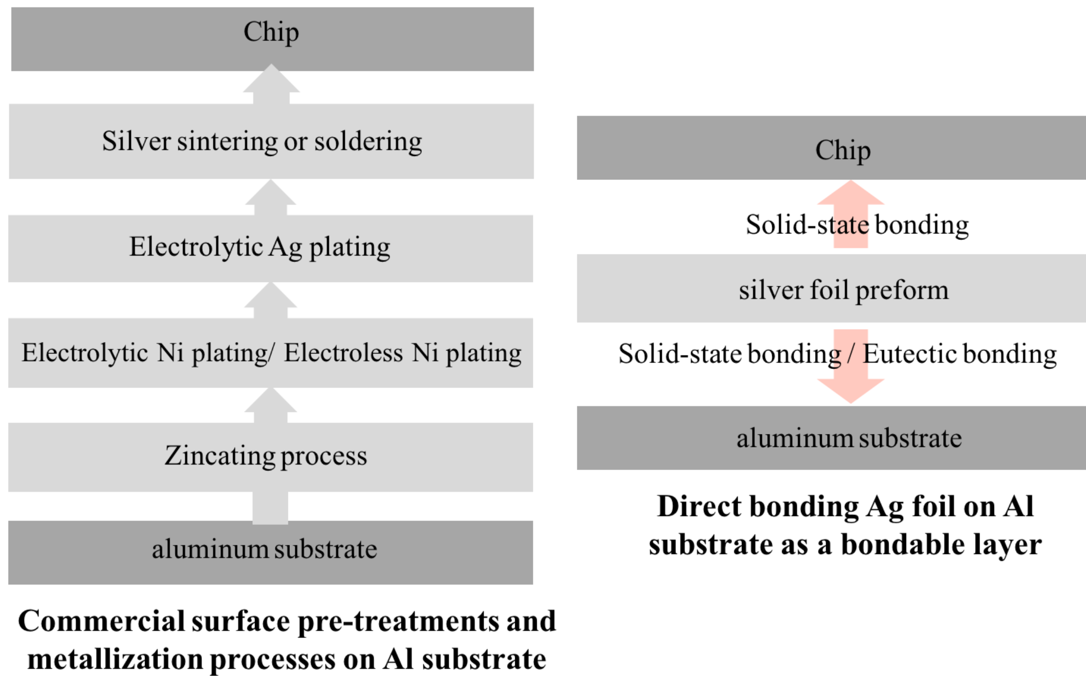

Fig. 7.1 (a) Commercial surface activating and metallization processes on Al substrates and subsequent die-attach process such as silver sintering or soldering. (b) New Ag-Al eutectic and solid-state techniques to bond Al foil directly on Al substrate, onto which Si chip can be directly bonded using solid-state bonding.

7.2 Experimental Design and Procedures

To produce Ag foils, Ag ingots are first grown by melting Ag shots (99.99% purity) in evacuated quartz tubes, followed by furnace cooling down to room temperature. Multiple rounds of cold rolling and subsequent annealing are performed to reduce the thickness of Ag ingots. The post-rolling annealing temperature is designed at 300 °C to release the mechanical stress in the foils and allow Ag grain recrystallization. Accordingly, Ag foils with

a thickness of 150 μm are successfully produced for the subsequent bonding process. To prepare the semiconductor chips, 4-inch Si wafers are sputtered with chromium/gold (Cr/Au, 30 nm/50 nm), followed by Ag electroplating (10 μm). The metalized wafers are then diced into 4 mm × 4 mm chips which are ready for bonding.

Fig. 7.2 illustrates the bonding structure design of the Ag foil bonding technique with detailed bonding parameters listed in Table 1. For the first bond, two bonding techniques, Ag-Al solid-state bonding and Ag-Al eutectic bonding, respectively, are performed to directly bond Ag foils to Al substrates. Prior to bonding, Ag foils and Al substrates are polished with 1 μm diamond powder suspension solution to achieve clean surfaces. During the bonding process, the Ag foil is placed over the Al substrate and held by a fixture with 1,000 psi (6.89 MPa) static pressure to ensure intimate contact. The assembly is loaded into a bonding furnace and heated with temperature monitored by a miniature thermocouple. As shown in Table 1, the Ag-Al solid-state bonding is conducted at 450 °C for 10 minutes under 0.1 Torr (13.33 Pa) vacuum, and the Ag-Al eutectic bonding is conducted at 570 °C for 5 minutes in air atmosphere. After bonding, the samples are kept in the furnace and cool down naturally to room temperature.

For the second bond, metalized Si chips are bonded to the foil-attached Al substrates by solid-state bonding. The same solid-state bonding technique is performed at 300 °C for 10

minutes under 0.1 Torr vacuum. After bonding, the Si/Ag/Al samples are kept in the furnace and cool down naturally to room temperature. The microstructures and phase compositions of resulting Si/Ag/Al joints are examined using scanning electron microscopy/energy dispersive X-ray spectroscopy (SEM/EDX, FEI Philips XL-30, FEG SEM) in back-scattered electron (BSE) mode. To evaluate bonding quality of the joints, die shear test is carried out using XYZ Condor Sigma Shear Tester (XYZTEC). The shear speed is set at 100 μm/s, and the shear height is controlled at 200 μm. After the shear test, the fracture surfaces of the joints are examined by SEM/EDX. The deformation morphology and phase composition of the fracture area are studied in detail.

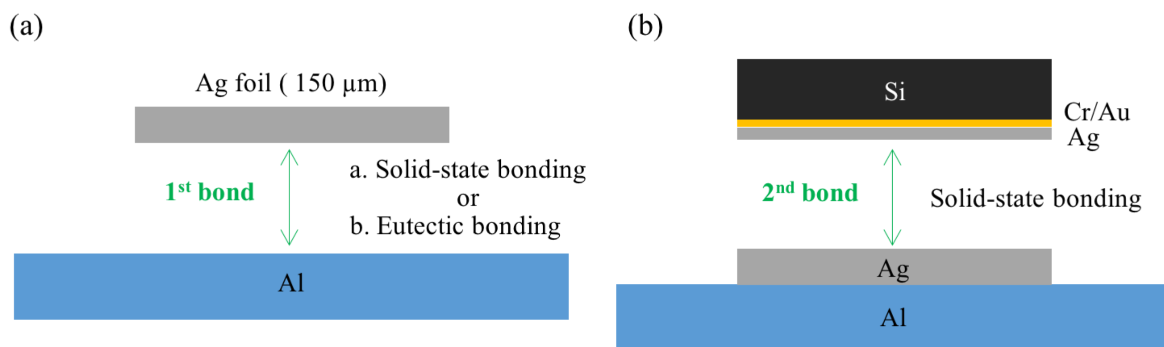

Fig. 7.2 Bonding structure design of the Ag foil bonding technique. (a) First bonding step: Ag-Al solid-state bonding or Ag-Al eutectic bonding to bond Ag foil directly to Al substrate. (b) Second bonding step: solid-state process to bond metalized Si chip to Ag-cladded Al substrate.

Table 1. Conditions of the first bonding step (Ag-Al solid-state and eutectic) and the second bonding step (solid-state) to produce the Si/Ag/Al structure.

	First bonding step		Second bonding step
	a. Solid-state bonding	**b. Eutectic bonding**	**Solid-state bonding**
Bonding temperature	450 ºC for 10 min	570 ºC for 4.5 min	300 ºC for 10 min
Bonding pressure	1000 psi	1000 psi	1000 psi
Vacuum	0.1 Torr (13.33 Pa)	air atmosphere	0.1 Torr (13.33 Pa)

7.3 Experimental Results and Discussion

7.3.1 Ag Foil Bonding Technique to Produce Si/Ag/Al joints

In this research, a two-step bonding process has been developed to bond Si chips to Al substrates using Ag foils. The first bonding step bonds Ag foils directly to Al substrates without using any flux. The second bonding step attaches Si chips to the Ag-cladded Al substrates using solid-state bonding technique. Fig. 7.3 shows the cross-section back-scattered electron images of a Si/Ag/Al joint structure for which solid-state process was used for the first bonding step. Given the large difference in the coefficient of thermal expansion (CTE) between Si (2.7×10^{-6} /°C) and Al (23×10^{-6} /°C), the crack-free Si chip implies that the ductile Ag layer is capable of managing the stress induced by CTE mismatch. In the

first bonding step, Ag foils were bonded to Al substrates at 450 °C for 10 minutes. During the solid-state bonding, Ag and Al surfaces conform to each other through elastic deformation to achieve intimate contact. The atomic interdiffusion of Ag and Al led to IMC growth at the Ag/Al bonding interface. SEM images at higher magnification show that the continuous Ag-Al IMC layer grew into both Al and Ag regions. The original bonding interface appears as a thin black line. In our previous study, nanoscale structures of the Ag-Al solid-state bonding interface were investigated using TEM and STEM with electron diffraction techniques [24]. This black line was identified as native Al_2O_3 layer formed on the Al surface prior to bonding. EDX analysis was performed on the enlarged SEM image, Fig. 7.3 (c), where red dots marked 1 - 5 indicate locations at which the resulting compositions are listed in Table 2. Based on the EDX data, Ag_2Al grew into both Ag and Al regions away from the original bonding interface. A thin layer of Ag_3Al formed between the Ag_2Al and Ag regions. Referring to our TEM study, during solid-state bonding, Ag and Al atoms interdiffused through the 5 nm Al_2O_3 layer and formed Ag_2Al and Ag_3Al compounds. The continuous Al_2O_3 layer was well connected to the surrounding Ag_2Al compound at atomic level without any nano-voids.

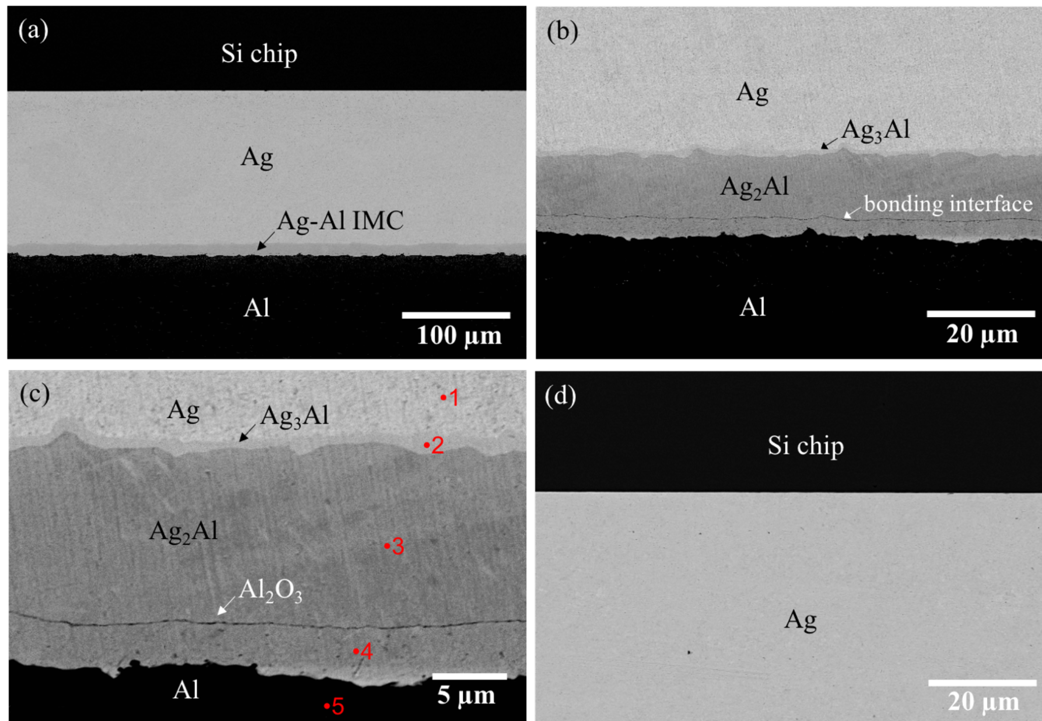

Fig. 7.3 SEM back-scattered electron images of a Si/Ag/Al sample for which the first bonding step is Ag-Al solid-state process and the second step is solid-state bonding of Si chip. In the enlarged image (c), the red dots marked by 1 - 5 indicate EDX analysis locations with element compositions listed in Table 7.2.

Table 7.2 EDX data on locations 1 - 5 near Ag/Al interface in Fig. 7.3 (c).

Locations	Ag (at. %)	Al (at. %)	Phases
1	98.5	1.5	(Ag)
2	77.6	22.4	Ag_3Al
3	65.7	34.3	Ag_2Al
4	65.4	34.6	Ag_2Al
5	0.9	99.1	(Al)

In the second bonding step, metalized Si chips were bonded to the Ag-cladded Al substrates at 300 °C for 10 minutes. It is worth mentioning that the Si chips were sputtered with Cr/Au (30 nm/50 nm), followed by Ag electroplating (10 μm). The Cr/Au films serve as a seed layer for electroplating and provide strong adhesion to the Si surface. The electroplated Ag layer worked as a buffer layer to achieve better interfacial contact during bonding. The enlarged SEM image, Fig. 7.3 (d), shows a sharp Si/Ag interface without IMC formation. No voids or crack were observed near the interface region. The Ag-Al phase diagram is presented in Fig. 7.4 to show the composition ranges of the Ag_2Al and Ag_3Al intermetallic phases [25].

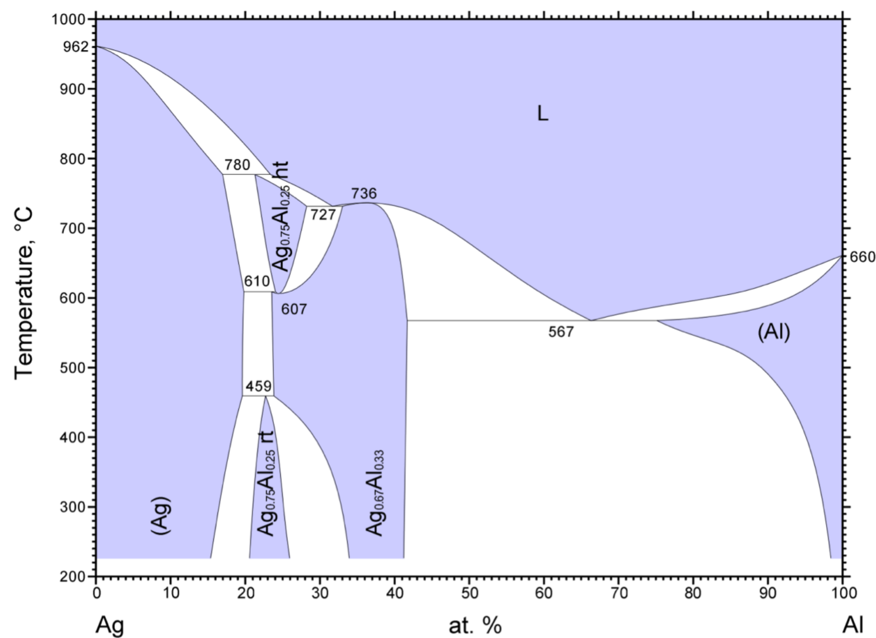

Fig. 7.4 The Ag-Al binary phase diagram showing that Ag_3Al and Ag_2Al compounds have a wide compositional range [25].

As shown above, by using the Ag-Al solid-state bonding technique, Ag foils were directly bonded to Al substrates without metallization, and crack-free Si/Ag/Al joints were successfully produced. The bonding strength of the Si/Ag/Al joints was later evaluated by the die shear test performed at room temperature. Considering the brittle nature of Al_2O_3, the continuous Al_2O_3 layer remaining at the Ag/Al bonding interface could possibly be a weak link of the Si/Ag/Al joints in terms of mechanical reliability. To eliminate the interfacial Al_2O_3 layer and further improve the joint reliability, a novel eutectic bonding technique has been developed to directly bond Ag foils to Al substrates using Ag-Al eutectic reaction in air. Based on the phase diagram, the Ag-Al system has a eutectic point between the Ag_2Al intermetallic phase and Al-rich solid solution (Al) at a temperature of 567 °C. To achieve Ag-Al bonding using the eutectic reaction, 570 °C, a little higher than the eutectic temperature, was selected as the bonding temperature.

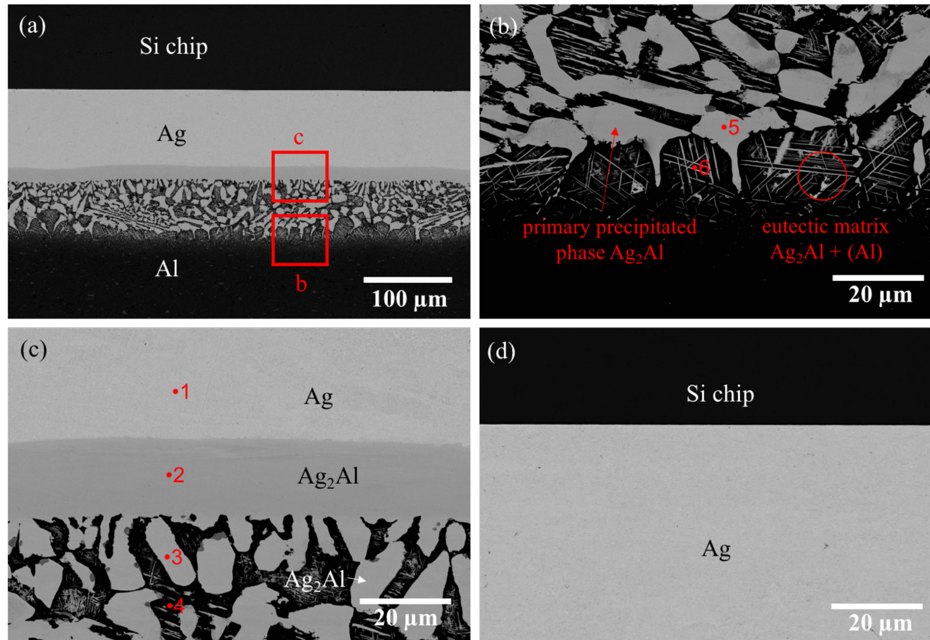

Fig. 7.5 SEM back-scattered electron images of a Si/Ag/Al sample for which the first bonding step is Ag-Al eutectic process and the second step is solid-state bonding of Si chip. In the enlarged image, (b) and (c), the red dots marked by 1-6 indicate the EDX analysis locations with element compositions listed in Table 7.3.

Table 7.3 EDX data on locations 1 - 6 near Ag/Al interface in Fig. 5 (b) and (c).

Locations	Ag (at. %)	Al (at. %)	Phases
1	98.7	1.3	(Ag)
2	65.6	34.4	Ag_2Al
3	63.7	36.3	Ag_2Al
4	14.6	85.4	(Al)
5	62.5	37.5	Ag_2Al
6	5.6	94.4	(Al)

Fig. 7.5 shows cross-section back-scattered electron images of a Si/Ag/Al joint for which the first bonding step was conducted using Ag-Al eutectic reaction. In the first bonding step, Ag foils were bonded to Al substrates at 570 °C for 5 minutes. While the samples were

heated up to 570 °C, Ag and Al largely interdiffused across the Ag/Al interface. As the local composition near the Ag/Al interface reached the eutectic composition, the interface region melted into Ag-Al eutectic liquid at the temperature right above 567 °C. The molten Ag-Al eutectic liquid broke up the thin Al_2O_3 layer at the bonding interface and promoted metallic bonding to the Al substrate. During the sample cooling process, the eutectic liquid solidified and a resultant eutectic structure appeared at the bonding interface region. In Fig. 7.5 (b), the bright primary precipitated phase (Ag_2Al) and the dark surrounding eutectic matrix (Ag_2Al + Al solid solution) are clearly observed. The eutectic matrix is a mixture the plate-like Ag_2Al phase and the Al-rich solid solution (Al). As shown in Fig. 7.5 (c), a continuous Ag_2Al layer formed between the eutectic region and the Ag region, which could be attributed to Ag-Al solid-state reaction. It is worth pointing out that the formation of Ag_3Al was significantly suppressed, and no Ag_3Al layer was observed at the Ag_2Al/Ag interface. In addition, no black line of Al_2O_3 was observed within the Ag_2Al layer or the bonding interface because the native Al_2O_3 layer was broken into pieces during eutectic reaction and possibly dispersed into the eutectic structure. EDX analysis was performed on images in Fig. 7.5 (b) and (c), where red dots marked 1 - 6 indicate locations at which the resulting compositions are listed in Table 3. EDX results show that the primary Ag_2Al phase contains 62.5 - 65.6 at. % Ag, and the Al-rich solid solution contains 5.6 - 14.6 at. % Ag. For the second bonding step,

the solid-state bonding technique mentioned previously was used to attach metalized Si chips to Ag-cladded Al substrates. The solid-state process was performed at 300 °C for 10 minutes. The enlarged SEM image, Fig. 5 (d), shows clear Si/Ag interface without IMC formation. No voids or cracks were observed near the bonding interface.

7.3.2 Shear Test Results of the Si/Ag/Al joints

The shear strength of Si/Ag/Al joints was evaluated by a standard die shear test. The specimens were tested at room temperature using a XYZ Condor Sigma Shear Tester (XYZTEC). The die shear test configuration is schematically illustrated in Fig 6 (a). The shear height was controlled at 200 μm to apply shear force on the Si chip, and the shear speed was set at 100 μm/s. A total of twelve samples were tested, including six Si/Ag/Al joint samples produced by Ag-Al solid-state bonding and six joint samples produced by Ag-Al eutectic bonding. Two different fracture modes were observed in both types of samples during the die shear test. Fig. 7.6 (b) shows the optical image of the sample fractured at the Ag/Al interface, and Fig. 7.6 (c) shows the sample fractured at the Si chip.

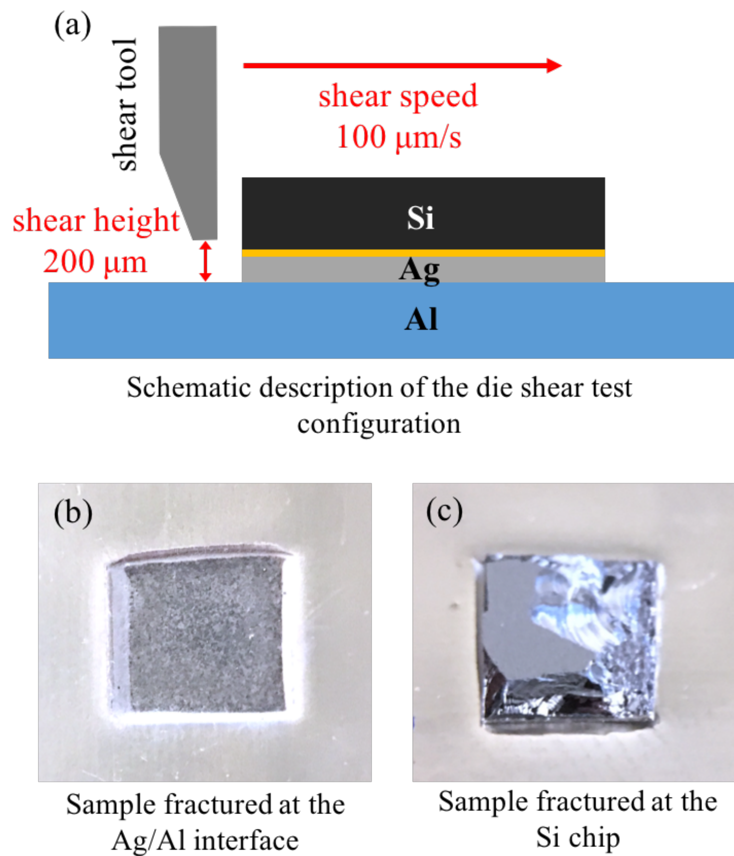

Fig. 7.6 (a) The schematic illustration of die shear test configuration. (b) Optical image of a sample fracturing at the Ag/Al interface. (c) Optical image of a sample fracturing within the Si chip.

Shear test results of the Si/Ag/Al joints produced by Ag-Al solid-state bonding and Ag-Al eutectic bonding are presented in Table 4 and Table 5, respectively. The fracture force, shear strength, and the fracture interface of each tested sample are listed. Test results show that, of the six samples produced by Ag-Al solid-state bonding, the fracture force ranges from 12.3 to 56.1 kgf. For samples 2 - 5, the Si chip was completely removed by the shear tool, and

the joint fractured along the Ag/Al interface. For samples 1 and 6, the sample fractured within the Si chip rather through the joint. The average shear strength of the solid-state bonded samples is 22.3 MPa. For the six samples produced by Ag-Al eutectic bonding, the fracture force ranges from 28.3 to 122.6 kgf. Samples 7, 8, 10, and 12 fractured within the Si chip. For samples 9 and 11, the Si chip was removed during shear test and the joint fractured along the Ag/Al interface. Compared to samples prepared by Ag-Al solid-state bonding, Si/Ag/Al samples prepared by Ag-Al eutectic reaction exhibit a higher average shear strength of 39.8 MPa. For both solid-state bonded samples and eutectic bonded samples, the joint strength values exceed the military criterion (MIL-STD-883H method 2019.8) by a large margin [26].

Table 7.4 Shear test results on breakage force, shear strength, and fracture interface of six Si/Ag/Al joint samples produced by Ag-Al solid-state bonding.

Si/Ag/Al joint samples produced by Ag-Al solid-state bonding			
Sample #	**Fracture force (kgf)**	**shear strength (MPa)**	**fracture mode and interface**
1	52.6	32.9	Within Si chip
2	12.3	7.7	Ag/Al interface
3	29.5	18.4	Ag/Al interface
4	28.2	17.6	Ag/Al interface
5	56.1	35.1	Ag/Al interface
6	35.9	22.4	Within Si chip
Average shear strength: 22.3 MPa			

Table 7.5 Shear test results on breakage force, shear strength, and fracture interface of six Si/Ag/Al joint samples produced by Ag-Al eutectic bonding.

Si/Ag/Al joints produced by Ag-Al eutectic bonding			
Sample #	**Fracture force (kgf)**	**shear strength (MPa)**	**fracture mode and interface**
7	50.2	31.4	Within Si chip
8	28.3	17.9	Within Si chip
9	85.5	53.4	Ag/Al interface
10	32.2	20.1	Within Si chip
11	62.6	39.1	Ag/Al interface
12	122.6	76.6	Within Si chip
Average shear strength: 39.8 MPa			

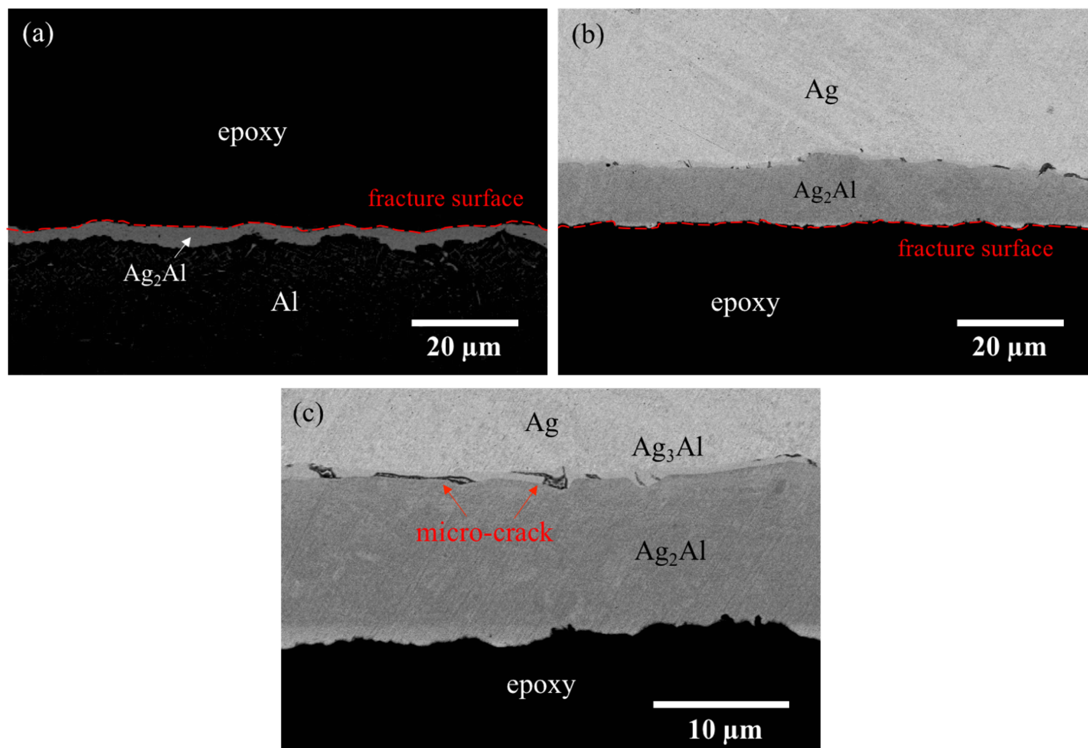

Fig. 7.7 Back-scattered SEM images of a fractured Si/Ag/Al sample for which the first bonding step is solid-state process: (a) the Al side, (b) the Ag side, (c) enlarged image of (b).

To understand the fracture behavior of the Si/Ag/Al joints, the deformation morphology and phase composition of the fracture area were evaluated by SEM/EDX. For solid-state bonded Si/Ag/Al joints, samples 3 and 5 were examined to study the fractured interface. For eutectic bonded Si/Ag/Al joints, samples 9 and 11 were examined. Since the Si/Ag/Al joints fractured along the Ag/Al bonding interface, the Ag side and Al side of the test sample were, respectively, molded with epoxy, cut in cross sections and polished for characterization. Fig. 7.7 displays the back-scattered electron images of fractured Ag/Al interface in a solid-state bonded sample. The cross-section images reveal that fracture occurred along the Al_2O_3 layer within the Ag_2Al region visible in Fig. 3(c). As shown in Fig. 7 (a), a thin Ag_2Al layer, which was originally beneath the black Al_2O_3 line, was left on the Al substrate after the shear test. In Fig. 7 (b), a smooth fracture surface was observed on the Ag foil that ended with a thin Ag_3Al layer and a Ag_2Al region that broke along the black Al_2O_3 line. As mentioned in previous sections, no surface treatment was applied to Al substrates to remove native oxide layer before the Ag-Al solid-state bonding process. The continuous Al_2O_3 layer existing at the Ag/Al interface seems to be the weak link of Si/Ag/Al joints because the joints tend to fracture along the brittle Al_2O_3 layer. It is worth pointing out that several isolated micro-cracks were observed within the thin Ag_3Al layer. The enlarged SEM image, Figs. 7 (c), shows that the micro-cracks were confined within the Ag_3Al layer and did not propagate into the

Ag_2Al or the Ag region. No cracks were observed within the Ag_2Al, indicating that Ag_2Al is relatively ductile compared to Ag_3Al. These results are consistent with our previous discovery on the mechanical properties of bulk Ag_2Al and Ag_3Al intermetallic phases [27]. The micro-indentation results show that Ag_3Al exhibits remarkably higher hardness and lower fracture toughness as compared to Ag_2Al. Unlike most intermetallic compounds, Ag_2Al exhibits considerable ductility as no indentation crack was observed under 1,000 gf loading force. Fig. 7.8 displays the SEM secondary electron images of the fracture surfaces on the Al side of the solid-state bonded sample. The microstructure exhibits a flat Ag_2Al surface with no Al substrate exposed. The enlarged SEM image, Figs. 7.8 (b), shows some cleavage features on the smooth fracture surface with very little plastic deformation.

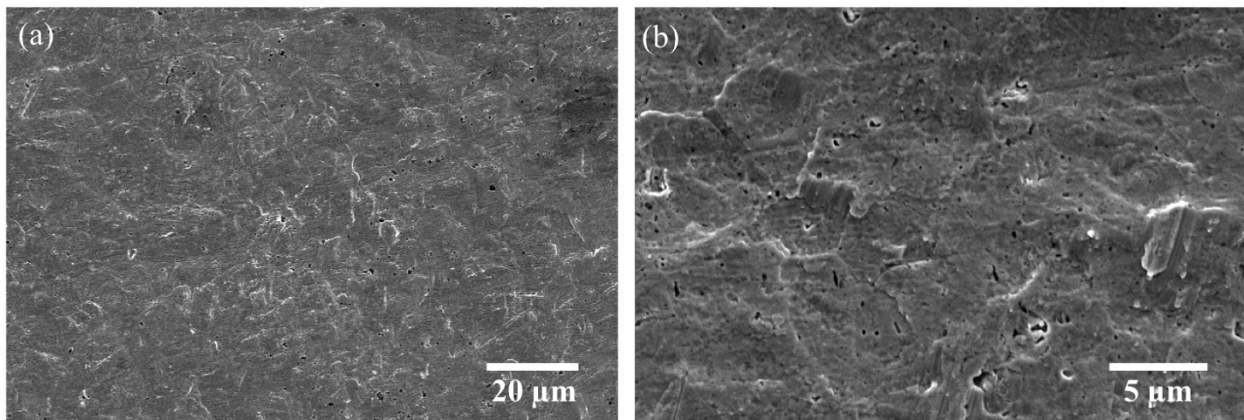

Fig. 7.8 (a) SEM secondary electron image of the fracture surface on the Al side of a Si/Ag/Al joint sample for which Ag-Al solid-state process was used for the first bonding step. (b) Enlarged SEM image of the fracture surface.

Fig. 7.9 displays the back-scattered electron images of the fractured Ag/Al interface in a eutectic bonded sample. The cross-section images reveal that fracture occurred within the eutectic region at the bonding interface. On the broken surfaces of Al and Ag sides of the sample, an irregular fracture surface was observed within the Ag_2Al+(Al) eutectic structure. It appears that, due to plastic deformation, some isolated voids formed within the eutectic structure near the fracture surface, as shown in Fig. 7.9 (b). No cracks or voids were observed within the Ag_2Al layer and the Ag regions. Fig. 7.10 shows the SEM secondary electron images of the fracture surface on the Al side of the eutectic bonded sample. The microstructure exhibits a mixed fracture characteristic within the eutectic region, including the trans-granular fracture of Ag_2Al compound and the ductile deformation of the Al solid solution. The enlarged SEM image, Fig. 7.10 (b), shows the quasi-cleavage features with fine steps and tear ridges on the Ag_2Al fracture surface. The fractured Ag_2Al compounds are surrounded and connected by the plastic-deformed Al solid solution with dimples and ridges.

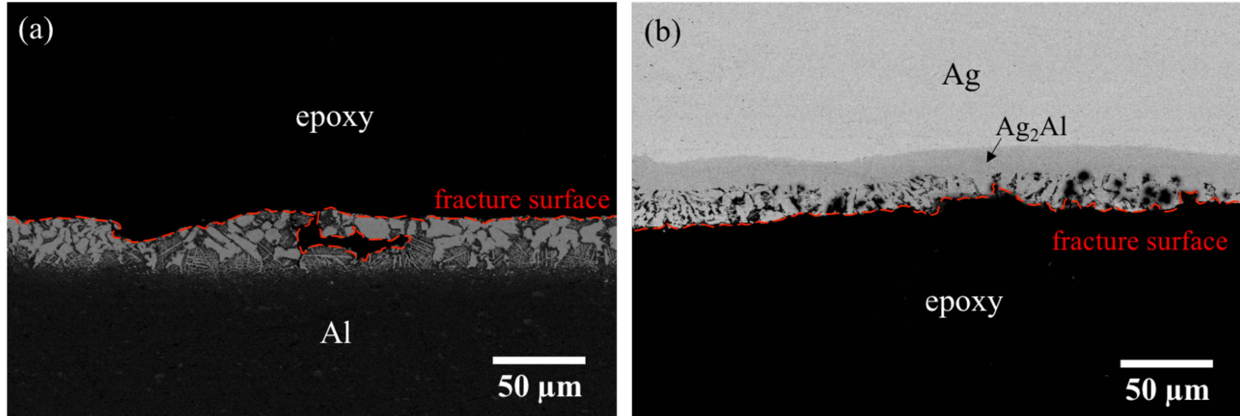

Fig. 7.9 The SEM back-scattered electron images of the fractured Ag/Al interface of a Si/Ag/Al joint for which the first bonding step was conducted using Ag-Al eutectic reaction. (a) Al side and (b) Ag side.

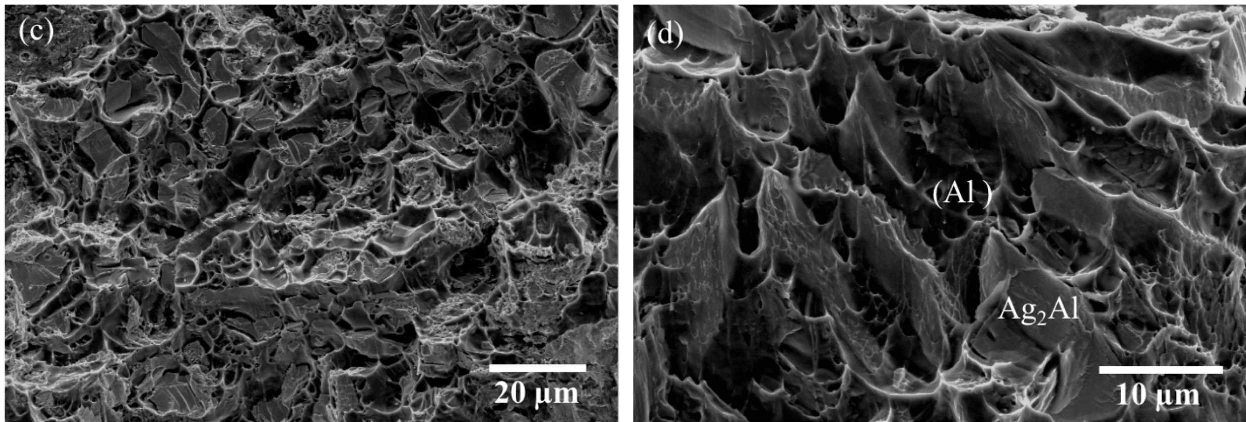

Fig. 7.10 (a) SEM secondary electron image of the fracture surface on the Al side of a Si/Ag/Al joint sample for which the first bonding step was conducted using Ag-Al eutectic reaction. (b) Enlarged SEM image showing the quasi-cleavage feature of the Ag_2Al compound and the ductile dimples on the Al solid solution.

As compared to the Ag-Al solid-state bonding with the cleavage fracture of Al_2O_3, the Ag-Al eutectic bonding exhibits superior bonding reliability and a more ductile fracture behavior. The interfacial Al_2O_3 layer and brittle Ag_3Al IMC layer were successfully eliminated in the Ag-Al eutectic bonding. As a potential fracture path, the continuous Al_2O_3 layer was broken during the eutectic reaction and possibly dispersed into the Ag_2Al+(Al) eutectic structure. The eutectic structure provides an excellent mechanical combination of the high-hardness Ag_2Al compounds and the surrounding high-ductility Al solid solution, and therefore allows the Ag-Al eutectic bonding to achieve a much higher shear strength. Furthermore, it is important to prevent the Ag_3Al IMC formation in the Ag-Al bonding. In our previous research on Ag_3Al and Ag_2Al intermetallic compounds, Ag_3Al possesses a lower fracture toughness with brittle nature, and exhibits a lower corrosion resistance to moisture and chlorine in the epoxy molding compound [27,28]. In this study, micro-cracks were observed within the thin Ag_3Al IMC layer in the Ag-Al solid-state bonding after shear test. The Ag-Al bonding reliability could be further deteriorated with thicker Ag_3Al IMC growth under long-term thermal aging. Based on the Ag-Al diagram, the Ag_3Al phase only stabilizes below 459 °C (μ phase) or within the range of 610 °C to 780 °C (β phase). In the Ag-Al eutectic bonding process, as the bonding temperature reached 570 °C, the formation of Ag_3Al was suppressed or possibly transformed into Ag_2Al phase.

7.4 Summary

In this research, a novel Ag foil bonding technique has been developed to bond Ag foil directly to Al substrates by Ag-Al eutectic reaction in air or solid-state process, respectively. Prior to bonding Ag foils to Al substrates, no surface treatment was applied to Al substrates to remove the native Al_2O_3 layer. The resulting structure is a Ag-cladded Al substrate for further applications. For samples bonded with Ag-Al eutectic reaction, Ag and Al atoms inter-diffused through the thin Al_2O_3 to react and form Ag_2Al and Ag_3Al compounds. The continuous Al_2O_3 layer was well connected to the surrounding Ag_2Al compound. For samples bonded with Ag-Al eutectic reaction, cross-sectional SEM images exhibit a zone of eutectic structure of Ag_2Al and (Al) phases along the Ag/Al interface. The native Al_2O_3 layer, a potential fracture plane, was broken into pieces during the eutectic reaction and possibly dispersed into the eutectic structure. It is interesting to notice that the other compound, Ag_3Al, was not found in the eutectic structure.

To demonstrate the application of the Ag-cladded Al substrate, Si chips were bonded to the substrates using solid-state process at 300 °C without any additional die-attach material. Twelve Si/Ag/Al joint samples were prepared for shear test. The resulting breaking force far exceeds the military criterion (MIL-STD-883H method 2019.8). These samples fractured

either along the Ag-Al interface or within the Si chip. In the samples fractured at the Ag-Al interface, the solid-state bonded samples exhibit a cleavage fracture mode along the Al_2O_3, and the eutectic bonded samples exhibit a mixed fracture mode with more ductile features. We expect the Ag-cladded Al substrates to have valuable applications for electronic and photonic packages and housings where high heat-conducting and lightweight are necessary requirements, such as in aerospace and in space

7.5 References

1. C. Buttay, D. Planson, B. Allard, D. Bergogne, P. Bevilacqua, C. Joubert, M. Lazar, C. Martin, H. Morel and D. Tournier, "State of the art of high temperature power electronics," Materials Science and Engineering: B, vol. 176, no. 4, pp. 283-288, 2011.
2. R. F. Davis, Z. Sitar, B. Williams, H. Kong, H. Kim, J. Palmour, J. Edmond, J. Ryu, J. Glass, and C. Carter Jr. "Critical evaluation of the status of the areas for future research regarding the wide band gap semiconductors diamond, gallium nitride and silicon carbide." Materials Science and Engineering: B, vol. 1, no. 1, pp. 77-104, 1988.
3. H. Matsunami. "Current SiC technology for power electronic devices beyond Si." Microelectronic engineering, vol. 83, no. 1, pp. 2-4, 2006.

4. J. Millan, P. Godignon, X. Perpina, A. Pérez-Tomás, and J. Rebollo. "A survey of wide bandgap power semiconductor devices." IEEE transactions on Power Electronics, vol. 29, no. 5 , pp. 2155-2163. 2014.

5. R. S. Pengelly, S. M. Wood, J. W. Milligan, S. T. Sheppard, and W. L. Pribble. "A review of GaN on SiC high electron-mobility power transistors and MMICs." IEEE Trans. Microwave Theory Tech., vol. 60, no. 6 , pp. 1764-1783. 2012.

6. P. Hagler, P. Henson and R. W. Johnson, "Packaging technology for electronic applications in harsh high-temperature environments," IEEE Trans. Ind. Electron., vol. 58, no. 7, pp. 2673-2682, 2011.

7. H. Chin, K. Cheong, and A. Ismail, "A review on die attach materials for SiC-based high-temperature power devices," Metallurgical Mater. Trans. B, vol. 41, pp. 824–832, 2010.

8. Y. Yamada, Y. Takaku, Y. Yagi, K. Ishida et al., "Reliability of wire-bonding and solder joint for high temperature operation of power semiconductor device", Microelectronics Reliability, vol. 47, no. 12, pp. 2147-2151, 2007.

9. K. S. Siow. "Mechanical properties of nano-silver joints as die attach materials." J. Alloys Compounds, vol. 514, pp. 6-19, 2012.

10. T. Wang, X. Chen, G. Lu, and G. Lei. "Low-temperature sintering with nano-silver paste in die-attached interconnection." J Electron Mater, vol. 36, no. 10, pp. 1333-1340, 2007.

11. S. Y. Zhao, X. Li, Y. H. Mei, G.Q. Lu, "Study on high temperature bonding reliability of sintered nanosilver joint on bare copper plate", Microelectronics Reliability, vol. 55, pp. 2524-2531, 2015.

12. S. T. Chua, K. S. Siow, "Microstructural studies and bonding strength of pressureless sintered nano-silver joints on silver direct bond copper (DBC) and copper substrates aged at 300°C", Journal of Alloys and Compounds, vol. 687, pp. 486-498, 2016.

13. R. Khazaka, L. Mendizabal, D. Henry, and R. Hanna. "Survey of high-temperature reliability of power electronics packaging components." IEEE Transactions on power Electronics, vol. 30, no. 5, pp. 2456-2464, 2015.

14. Y. Yoshino, H. Ohtsu and T. Shibata, "Thermally induced failure of Copper-Bonded alumina substrates for electronic packaging," *J Am Ceram Soc*, vol. 75, no. 12, pp. 3353-3357, 1992.

15. D. Camilleri, "Thermo-mechanical behaviour of DBC substrate assemblies subject to soldering fabrication processes," *Soldering & Surface Mount Technology*, vol. 24, no. 2, pp. 100-111, 2012.

16. G. Dong, X. Chen, X. Zhang, K. D. Ngo and G. Lu "Thermal fatigue behaviour of Al_2O_3-DBC substrates under high temperature cyclic loading," *Soldering & Surface Mount Technology*, vol. 22, no. 2, pp. 43-48, 2010.

17. S. Kraft, A. Schletz and M. Maerz, "Reliability of silver sintering on DBC and DBA substrates for power electronic applications," in *Integrated Power Electronics Systems (CIPS), 2012 7th International Conference on*, pp. 1-6, 2012.

18. T. G. Lei, J. N. Calata, K. D. Ngo and G. Lu, "Effects of large-temperature cycling range on direct bond aluminum substrate," *IEEE Transactions on Device and Materials Reliability*, vol. 9, no. 4, pp. 563-568, 2009.

19. S. Lee, J. Lee and Y. Kim, "Nucleation and growth of zinc particles on an aluminum substrate in a zincate process," *J Electron Mater*, vol. 36, no. 11, pp. 1442-1447, 2007.

20. M. M. Arshad, I. Ahmad, A. Jalar, G. Omar and U. Hashim, "The effects of multiple zincation process on aluminum bond pad surface for electroless nickel immersion gold deposition," *Journal of electronic packaging*, vol. 128, no. 3, pp. 246-250, 2006.

21. K. Azumi, S. Egoshi, S. Kawashima and Y. Koyama, "Effect of copper pretreatment on the double zincate process of aluminum alloy films," *J.Electrochem.Soc.*, vol. 154, no. 4, pp. D220-D226, 2007.

22. J. Lee, I. Lee, T. Kang, N. Kim and S. Oh, "The effects of bath composition on the morphologies of electroless nickel under-bump metallurgy on Al input/output pad," *J Electron Mater*, vol. 34, no. 1, pp. 12-18, 2005.

23. S. Robertson and I. Ritchie, "The role of iron (III) and tartrate in the zincate immersion process for plating aluminium," *J.Appl.Electrochem.*, vol. 27, no. 7, pp. 799-804, 1997.

24. S. Fu and C. C. Lee. "Direct silver to aluminum solid-state bonding processes." Materials Science and Engineering: A, vol. 722, pp. 160-166, 2018.

25. S. Lim, P. Rossiter and J. Tibballs, "Assessment of the al-ag binary phase diagram," *Calphad*, vol. 19, no. 2, pp. 131-141, 1995.

26. Department of Defense, U.S.A., Test Method Standard Microcircuits, 2010, MIL-STD-883H method 2019.8.

27. S. Fu and C.C. Lee, " A study on intermetallic compound formation in Ag-Al system and evaluation of its mechanical properties by micro-indentation," *J. Mater.Sci.: Mater.Electron.*, vol. 29, no. 5, pp. 3985-3991, 2018.

28. S. Fu and C.C. Lee, "A corrosion study of Ag–Al intermetallic compounds in chlorine-containing epoxy molding compounds," *J. Mater.Sci.: Mater.Electron.*, vol. 28, no. 20, pp. 15739-15747, 2017.

Chapter Eight

Summary

This dissertation aims to evaluate the material properties of the Ag-Al intermetallic compounds (IMC), and develop new Ag-Al bonding processes for high-temperature applications. In Chapter 3, Ag-Al alloys and Ag-Al joints are produced to study the intermetallic phases formation in Ag-Al alloys and at Ag/Al interface. The deformation and fracture behaviors of bulk Ag_2Al and Ag_3Al are evaluated using micro-indentation technique. The results show that Ag_3Al exhibits high hardness and low fracture toughness with brittle fracture mode, while Ag_2Al shows ductile deformation with no crack formation. In Chapter 4, a corrosion experiment according to industry condition is designed to measure the corrosion rates of Ag, Al, and Ag_3Al and Ag_2Al compounds in epoxy molding compounds under humidity test. The results show that the corrosion rate of Ag_3Al is twice of that of Ag_2Al, and no corrosion occurs on Ag or Al. The corrosion mechanism of Ag-Al IMC is established. New information obtained above can help the search of new processes and techniques to counter or reduce the brittle fracture and chlorine-induced corrosion of the Ag-Al wire bonds. The results clearly suggest that Ag_3Al is likely the weak link of the Ag-Al joints and should be eliminated or suppressed.

After studying the Ag-Al IMC properties, this dissertation further designs novel bonding processes to directly bond Ag to Al substrates. Two Ag-Al bonding processes are developed: solid-state and eutectic reaction, as presented in Chapter 5 and 6. No surface treatment was applied on Al substrates to remove the native Al_2O_3 layer before the bonding. SEM and TEM with electron diffraction technique was utilized to study the nanostructure of the bonding interface. The shear strength of Ag-Al joints passes the military standard by a large margin. At last, in Chapter 7, a two-step bonding process has been developed to bond Si chips to Al substrates using Ag foil bonding technique. Using the Ag foil as a bonding medium, Si chips are bonded to the Ag-cladded Al substrates using solid-state process at 300 °C without additional die-attach material. In the Ag-Al soli-state bonding process, Ag and Al atoms inter-diffused through the thin Al_2O_3 to form Ag_2Al and Ag_3Al compounds. In the Ag-Al eutectic bonding process, Ag_2Al+(Al) eutectic structure forms at the Ag/Al interface without Ag_3Al compound formation. The native Al_2O_3 layer, a potential fracture path, is broken into pieces during eutectic reaction and possibly dispersed into the eutectic structure. Shear test results of the resulting Si/Ag/Al joints far exceed the military criterion. The fracture mechanisms are studied in detail.

The two Ag-Al bonding processes provide alternatives to the zincating and metallization processes on aluminum substrates. The Ag foil bonding technique provides a novel solid-

state die-attach method on Al substrates to produce a reliable Si/Ag/Al joint structure. With the advantages of high thermal conductivity, high reliability, lightweight, and process simplicity, the Ag-cladded Al structures should be highly valuable for applications in electronic and photonic packages, such as aircraft and aerospace vehicles.